

FEDERAL UNIVERSITY OF ESPIRITO SANTO  
SCHOOL OF ENGINEERING  
ELECTRICAL ENGINEERING POSTGRADUATE PROGRAM

ALESSANDRO BOTTI BENEVIDES

**A BRAIN-COMPUTER INTERFACE ARCHITECTURE  
BASED ON MOTOR MENTAL TASKS AND MUSIC IMAGERY**

VITORIA  
2013

ALESSANDRO BOTTI BENEVIDES

**A BRAIN-COMPUTER INTERFACE ARCHITECTURE  
BASED ON MOTOR MENTAL TASKS AND MUSIC IMAGERY**

Document presented to the Electrical Engineering  
Postgraduate Program of the Federal University  
of Espirito Santo, as a partial requirement for the  
degree of Doctor in Electrical Engineering.

Advisors: Prof. Dr. Teodiano Freire Bastos Filho.  
Prof. Dr. Mário Sarcinelli Filho.

VITORIA, BRAZIL  
2013

Dados Internacionais de Catalogação-na-publicação (CIP)  
(Biblioteca Setorial Tecnológica,  
Universidade Federal do Espírito Santo, ES, Brasil)

---

B461b Benevides, Alessandro Botti, 1982-  
A brain-computer interface architecture based on motor  
mental tasks and music imagery / Alessandro Botti Benevides. –  
2013.  
161 f. : i.

Orientador: Teodiano Freire Bastos Filho; Mário Sarcinelli  
Filho.

Tese (Doutorado em Engenharia Elétrica) – Universidade  
Federal do Espírito Santo, Centro Tecnológico.

1. Interface cérebro-computador. 2. Neurociências. 3.  
Eletroencefalografia. 4. Processamento de sinais. 5. Sistemas de  
reconhecimento de padrões. 6. Análise multivariada. I. Bastos  
Filho, Teodiano Freire. II. Sarcinelli Filho, Mário. III. Universidade  
Federal do Espírito Santo. Centro Tecnológico. IV. Título.

CDU: 621.3

---

**ALESSANDRO BOTTI BENEVIDES**

**A BRAIN-COMPUTER INTERFACE ARCHITECTURE  
BASED ON MOTOR MENTAL TASKS AND MUSIC IMAGERY**

Thesis presented to the Electrical Engineering Postgraduate Program of the Federal University of Espirito Santo, as a partial requirement for the degree of Doctor in Electrical Engineering.

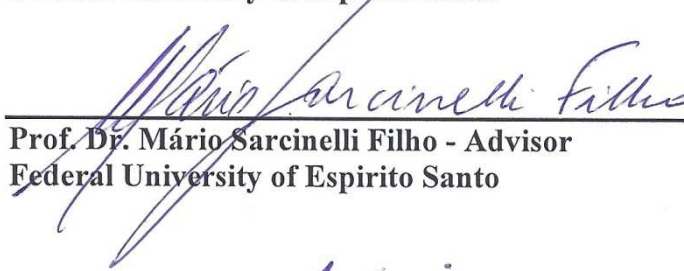
Approved on August 30, 2013.

EXAMINING COMMITTEE



---

**Prof. Dr. Teodiano Freire Bastos Filho - Advisor**  
Federal University of Espirito Santo




---

**Prof. Dr. Mário Sarcinelli Filho - Advisor**  
Federal University of Espirito Santo



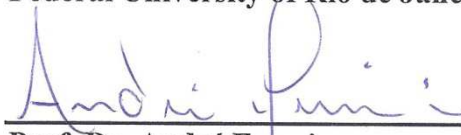
---

**Prof. Dr. Aura Conci**  
Fluminense Federal University



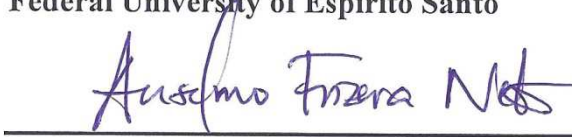
---

**Prof. Dr. Carlos Julio Tierra Criollo**  
Federal University of Rio de Janeiro



---

**Prof. Dr. André Ferreira**  
Federal University of Espirito Santo



---

**Prof. Dr. Anselmo Frizzera Neto**  
Federal University of Espirito Santo



To my parents, who taught me the value of work;  
to my brother, for his unconditional support;  
and to the teachers I met during the course,  
both those I was fortunate enough to know personally,  
but also those who enlightened my mind through the legacy of their words.

## Acknowledgments

I am thankful to Prof. Dr. Teodiano who advised me since 2005 when I was undergraduate research fellow studying Brain-Computer Interfaces to control a robotic wheelchair. He also advised me during my undergraduate Thesis and during the Master's degree program, in which we studied the Wavelet Transform, several classifiers and a general model to obtain the signal of cortical sources from the electroencephalogram signal. I am also very grateful for the opportunity provided by Prof. Teodiano, so I could perform a year of split Ph.D at the University of Alcalá de Henares, in Spain.

I am grateful to Prof. Dr. Anselmo for the hours of conversations, advice and suggestions spent at the Institute of Industrial Automatic (CSIC - Madrid). I'm sure that his suggestions - informally pronounced over coffee – are beyond comparison with the best ideas I might had, even after hours of mental labor. I am also very grateful to Prof. Dr. Mário Sarcinelli for advice and support since graduation. And I especially thank to my brother, Alessander, who I consider an excellent computer engineer and philosopher. He inspired me throughout my life, shaping much of my personality and helping me all through graduation.

Finally, I want to thank everyone I met at the LAI laboratory who helped me directly or indirectly. So, to be fair, I'll cite them in the chronological order in which I met them: Sandra, André Ferreira, Jhon Freddy, Dennis, Marcelo Hübner, Carlos Valadao, Igor Pizetta, Richard, Anibal and Javier. And I apologize to those that I probably forgot to mention.

There are no words to express how grateful I am to my mother, who helped me to close new scars (literally), and to overcome all the pain. Without her support I never would have finished this research. Mom, I thank you with all my heart.

## Abstract

This present research proposes a Brain-Computer Interface (BCI) architecture adapted to motor mental tasks and music imagery. For that purpose the statistical properties of the electroencephalographic signal (EEG) were studied, such as its probability distribution function, stationarity, correlation and signal-to-noise ratio (SNR), in order to obtain a minimal empirical and well-founded parameter system for online classification. Stationarity tests were used to estimate the length of the time windows and a minimum length of 1.28 s was obtained. Four algorithms for artifact reduction were tested: threshold analysis, EEG filtering and two Independent Component Analysis (ICA) algorithms. This analysis concluded that the algorithm “fastICA” is suitable for online artifact removal. The feature extraction used the Power Spectral Density (PSD) and three methods were tested for automatic selection of features in order to have a training step independent of the mental task paradigm, with the best performance obtained with the Kullback-Leibler symmetric divergence method. For the classification, the Linear Discriminant Analysis (LDA) was used and a step of reclassification is suggested. A study of four motor mental tasks and a non-motor related mental task is performed by comparing their periodograms, Event-Related desynchronization/synchronization (ERD/ERS) and SNR. The mental tasks are the imagination of either movement of right and left hands, both feet, rotation of a cube and sound imagery. The EEG SNR was estimated by a comparison with the correlation between the ongoing average and the final ERD/ERS curve, in which we concluded that the mental task of sound imagery would need approximately five times more epochs than the motor-related mental tasks. The ERD/ERS could be measured even for frequencies near 100 Hz, but in absolute amplitudes, the energy variation at 100 Hz was one thousand times smaller than for 10 Hz, which implies that there is a small probability of online detection for BCI applications in high frequency. Thus, most of the usable information for online processing and BCIs corresponds to the  $\alpha/\mu$  band (low frequency). Finally, the ERD/ERS scalp maps show that the main difference between the sound imagery task and the motor-related mental tasks is the absence of ERD at the  $\mu$  band, in the central electrodes, and the presence of ERD at the  $\alpha$  band in the temporal and lateral-frontal electrodes, which correspond to the auditory cortex, the Wernicke’s area and the Broca’s area.

## Summary

Chapter 1 : Introduction.....	1
<b>1.1 Motivation</b> .....	1
<b>1.2 Objectives</b> .....	7
<b>1.3 Thesis structure</b> .....	10
Chapter 2 : The human brain .....	11
<b>2.1 Section planes and reference points of the human brain</b> .....	11
<b>2.2 Description of the S1, M1, A1, V1 areas, Wernicke’s area and Broca’s area</b> .....	14
<b>2.3 Pyramidal tract and the contralaterality of motor movements</b> .....	17
<b>2.4 Neuronal circuits and oscillatory activity of the thalamocortical system</b> .....	18
<b>2.5 Direct pathway of movement</b> .....	24
Chapter 3 : The EEG signal.....	28
<b>3.1 Electroencephalographic signal</b> .....	28
<b>3.2 EEG acquisition</b> .....	34
<b>3.3 Main EEG rhythms</b> .....	39
<b>3.4 Artifacts</b> .....	43
<b>3.5 Spatial filtering</b> .....	48
<b>3.6 Methods for avoiding, discarding and minimizing artifacts</b> .....	50
<b>3.7 EEG records and SNR</b> .....	55
<b>3.8 Movement-related potentials</b> .....	60
<b>3.9 ERD/ERS</b> .....	62
Chapter 4 : The proposed BCI.....	68
<b>4.1 EEG Database</b> .....	68
<b>4.2 Pseudo-online method</b> .....	69
<b>4.3 Feature extraction</b> .....	71
<b>4.4 EEG stationarity</b> .....	73
<b>4.5 Feature Selection</b> .....	81
<b>4.6 Classifier</b> .....	87
<b>4.6.1 Bayesian Classifier</b> .....	87
<b>4.6.2 The normal distribution</b> .....	89
<b>4.6.3 Normal classifier</b> .....	93
<b>4.7 Simulated results and the reclassification method</b> .....	96
Chapter 5 : Results.....	103
<b>5.1 Experimental environment</b> .....	103
<b>5.2 EEG pre-processing and histograms</b> .....	105
<b>5.3 ERD/ERS scalp maps</b> .....	106
<b>5.4 Periodograms</b> .....	109

<b>5.5 Artifact removal techniques</b> .....	112
<b>5.6 Sampling rate analysis</b> .....	113
<b>5.7 Stationarity analysis</b> .....	115
<b>5.8 SNR analysis</b> .....	117
Chapter 6 : Conclusion .....	122
References .....	132
Appendix A .....	140

## List of Tables

Table 3.1 – Frequencies occurring in the human brain (Cheeín, 2005). .....	40
Table 4.1 – Confirmatory analysis of KPSS and ADF tests. TSP: Trend Stationary Process; NSURP: Non Stationary Unit-Root Process .....	76
Table 4.2 – Results from each subject.....	100
Table 4.3 – Statistical measures from each subject .....	100
Table 4.4 – Comparison with best results of dataset V submitted to BCI Competition III. The row labeled “Authors*” shows the classifications results obtained using 0.5 s reclassification windows, which is the same length used by the other studies shown here .....	101

## List of Figures

Figure 1.1 – BCI timeline. ....	8
Figure 2.1 – Section planes and reference points of the human brain (Russell, 2013). .	12
Figure 2.2 – Left: Skull bones; Right: Location of the four brain lobes (adapted from Bear, et al., 2008).....	12
Figure 2.3– Left: Brodmann’s cytoarchitectonic map (Bear, et al., 2008); Right: Main areas related to the processing of the senses.....	13
Figure 2.4 – Left: Somatotopic map of human pre-central gyrus (M1); Right: Somatotopic map of human postcentral gyrus (S1). ....	14
Figure 2.5 – Left: Location of Broca's area and Wernicke's area (adapted from Bear, et al., 2008); Right: primary, secondary, and tertiary auditory cortex. ....	15
Figure 2.6 – Visual information path from retina to visual cortex (adapted from Claffey, 2013).....	16
Figure 2.7 – Left: Spinal nerves and spinal nerve roots (adapted from Bear, et al., 2008); Right: Pyramidal system.....	17
Figure 2.8 – (A) Excitatory-inhibitory neuronal circuit (Guyton & Hall, 2006); (B) Two neurons oscillator; (C) Firing pattern of the two neurons oscillator (adapted from Bear, et al., 2008). ....	19
Figure 2.9 – Oscillatory neuronal circuits (Guyton & Hall, 2006).....	20
Figure 2.10 – Cortical layers. (A) Golgi method; (B) Nissl method; (C) Weigert method (adapted from Machado, 2007). ....	21
Figure 2.11 – (A) Location of the thalamus in the brain; (B) Schematic representation of the main nuclei of the thalamus; (C) connectivity of each nucleus with the cortex (adapted from what-when-how, 2013). ....	22
Figure 2.12 - Motor circuit. Green synapses are marked with sign (+) and are excitatory, while black synapses are marked with sign (-) and are inhibitory (adapted from Bear, et al., 2008). ....	25
Figure 3.1 - Typical EEG record (adaptated from Bear, et al., 2008). ....	28
Figure 3.2 – Electric field generated by extracellular currents in pyramidal cells (Bear, et al., 2008). ....	29
Figure 3.3 – (A) Bipolar configuration of the electric field of a pyramidal neuron during a PSP; (B) Bipolar configuration of the electric field of a pyramidal neurons of an active cortical region; (C) Equivalent current dipole of the active cortical region (Luck, 2005). ....	31
Figure 3.4 – (A) Pyramidal neurons beneath EEG electrode; (B) Unsynchronized neuronal activity; (C) Synchronized neuronal activity (adapted from Bear, et al., 2008). ....	32
Figure 3.5 – Concentric spherical head model proposed by Rush & Driscoll (Malmivuo & Plonsey, 1995). ....	33
Figure 3.6 – A) and B) International 10-20 System; C) International 10-10 System (Malmivuo & Plonsey, 1995). ....	35
Figure 3.7 –Grounding electrode (G), the reference electrode (R) and the active electrode (A) in order to compose the occipital channel O1. ....	36
Figure 3.8 – (A) Bipolar method; (B) Unipolar method (uniauricular reference); (C) Unipolar method (biauricular reference); (D) CAR method using the uniauricular reference. ....	37
Figure 3.9 – Decrease of the average reference amplitude as the number of channels increases.....	39

Figure 3.10 – Coverage of the EEG frequency spectrum (Thalamocortical oscillations, 2013).....	40
Figure 3.11 – Brain rhythms $\alpha$ , $\beta$ , $\theta$ and $\delta$ . The EEG signal at the bottom shows the occipital desynchronization measured when the eyes are open (adapted from Guyton & Hall, 2006).....	42
Figure 3.12 – EEG signal with grid line artifact and eye blinks artifacts (the mental tasks experiments are mentioned in chapter 3, section 3.8). ....	44
Figure 3.13 – a) EOG schematic; b) EOG electrode placement (Duane, 2006); c) Ocular dipole rotation affecting the EEG baseline.....	45
Figure 3.14 – Eye blink artifact on EEG. Left: EEG and periodogram of channel Fp1 heavily contaminated with low frequencies from eye blink artifacts; Middle: EEG and periodogram of channel C3 contaminated with low frequencies from eye blink artifacts and the artifact from the power grid line; Right: EEG and periodogram of channel C3 after applying the CAR method and a high pass filter with cutoff frequency of 5Hz....	46
Figure 3.15 – a) EEG signal corrupted with ECG and EOG artifacts; b) ECG signal; c) EOG signal (Garcés & Leber, 2011). ....	47
Figure 3.16 – (A) EEG (F3-C3) and EMG; (B) EEG and EMG Amplitude spectrums; (C) Coherence between EEG and EMG. The horizontal gray line is the 95% confidence interval (Grosse, 2004); (D) Deltoid muscle. ....	49
Figure 3.17 – Electrode location for the spatial filters analyzed (McFarland et al., 1997). ....	49
Figure 3.18 – EEG of channels Fp1 and C3 and their periodograms during the application of the following cases: raw EEG; CAR method; threshold analysis and filtering. ....	51
Figure 3.19 – ICA components obtained by “fastICA” algorithm and their fixed scalp topographies. ....	53
Figure 3.20 – EEG of channels Fp1 and C3 and their periodograms during the application of the following cases: raw EEG; “fastICA” algorithm and “runica” algorithm.....	54
Figure 3.21 – Left: ERP observation by averaging EEG recordings (Rugg & Coles, 1996); Right: Normal somatosensory evoked potential (adapted from Delamonica, 1984).....	56
Figure 3.22 – Bereitschaftspotential and the Libet’s experiment. At -550 ms: the rise of BP; at -200 ms: the awareness of intention; at -100 ms: the possibility of veto of the action; at 0 s: the action of pressing a button. ....	61
Figure 3.23 – DC potential of electrodes C3 and C4 (adapted from Beisteiner, et al., 1995).....	63
Figure 3.24 – ERD/ERS calculation method. The reference period was taken between 1 and 3 s and the motor mental task occurred between 5 and 15 s. (a) raw EEG from channel C3 during the first, fifteenth, and thirtieth epoch, respectively in black, dark and light gray; (b) EEG from channel C3 filtered at $\mu$ band; (c) channel C3 $\mu$ band energy (d) channel C3 $\mu$ band average energy of 60 epochs; (e) channel C3 $\mu$ band ERD/ERS. ....	65
Figure 3.25 – Activation and deactivation flow: (A) programming phase; (B) execution phase; (C) recovery phase (Bianchi, et al., 1995).....	67
Figure 4.1 – Left: raw EEG of channel C3 from the first section of each subject; Right: EEG band pass filtered from 1 to 32 Hz and preprocessed by the CAR method.....	69
Figure 4.2 – Left: averaged ACF obtained by using CAR method; Right: averaged ACF obtained by using the large Laplace. ....	71



Figure 4.3 – Low-dimensional visualization of the feature space; left: Sammon map of EEG signals in the time domain; center: Sammon map of PSD using all frequency components; right: Sammon map of PSD using selected frequency components ( $\xi = 50\%$ ).	72
Figure 4.4 – Left: The ongoing average $\mu$ and standard deviation $\sigma$ calculated with time-windows up to 10 s; Right: The ongoing average $\mu$ and standard deviation $\sigma$ calculated with time-windows lasting up to 240 s.	74
Figure 4.5 – A) left tailed test; B) right tailed test; C) two-tailed test.	76
Figure 4.6 – Application of KPSS and ADF tests for each subject.	80
Figure 4.7 – Channel $\times$ frequency matrix. $H_{C_1}$ , $H_{C_2}$ and $H_{C_3}$ are the histograms of the respective classes $C_1$ , $C_2$ and $C_3$ .	81
Figure 4.8 – Discriminative Power. Left: Histograms without overlap ( $DP = 1$ ); Right: Histograms with complete overlap ( $DP = 0$ ).	82
Figure 4.9 – Left: Discriminant Matrix $\mathbf{D}$ of subject 1 obtained with DP method; Right: Total contribution of each channel in relation to the discrimination between the classes.	83
Figure 4.10 – Left: Discriminant Matrix $\mathbf{D}$ of subject 1 obtained with DP method; Right: Total contribution of each channel in relation to the discrimination between the classes.	84
Figure 4.11 – Left: Discriminant Matrix $\mathbf{D}$ of subject 1 obtained with K-L method; Right: Total contribution of each channel in relation to the discrimination between the classes.	86
Figure 4.12 – Selection of features with discriminant values higher than Oz maximum discriminant.	86
Figure 4.13 – Left: Univariate normal distribution; Right: Mahalanobis distances from a bivariate normal distribution (Duda, et al., 2000).	93
Figure 4.14 – Nonlinear decision regions. (A) Decision boundary between two univariate normal distributions; (B) Decision boundary between two bivariate normal distributions; (C) Decision boundary between two four bivariate normal distributions (Duda, et al., 2001).	95
Figure 4.15 – Linear decision region of normal distributions. (A) Univariate normal distributions; (B) Bivariate normal distributions; (C) Multivariate normal distributions (Duda, et al., 2000).	96
Figure 4.16 – EEG histograms and estimated normal probability functions of subject 1 during the mental task of imagination of movement of the left hand.	97
Figure 4.17 – Classifier output.	98
Figure 4.18 – Time windows and reclassification windows.	99
Figure 4.19 – Success rate for different values of $\xi$ .	99
Figure 4.20 –Reclassification.	100
Figure 5.1 – a) BNT device; b) BNT panel (adapted from BrainNet - BNT36 User's manual, 2004); c) MedCap <sup>®</sup> cap of integrated electrodes, conductive electrolytic gel and paste.	104
Figure 5.2 – EEG histograms and estimated normal probability functions of subject 1 during the mental task of imagination of movement of the right hand.	106
Figure 5.3 – Relative energy of the $\alpha/\mu$ , $\beta$ and $\gamma$ bands. The reference period was taken between 1 and 3 s and the mental task occurred between 5 and 15 s. (a) arrangement of electrodes; (b) ERD/ERS scalp map during the mental task of imagination of movement of the right hand; (c) ERD/ERS scalp map during the mental task of imagination of movement of the left hand; (d) ERD/ERS scalp map during the mental task of imagination of movement of both feet; (e) ERD/ERS scalp map during the mental task	

of rotation of a cube; (f) ERD/ERS scalp map during the mental task of music imagery. ....	108
Figure 5.4 – (a) average periodogram during the mental task of rotation of a cube; (b) average periodogram during the mental task of rotation of a cube focused on the activity from 0 to 30 Hz; (c) average periodogram with relative amplitudes for the mental task of rotation of a cube; (d) average periodogram with relative amplitudes for the mental task of rotation of a cube focused on the activity from 0 to 30 Hz; (e) average periodogram with relative amplitudes for the mental task of music imagery; (f) average periodogram with relative amplitudes for the mental task of music imagery focused on the activity from 0 to 30 Hz.....	111
Figure 5.5 – ERD/ERS of channel C3 at $\mu$ band. In black: ERD/ERS obtained without artifact removal; in dark gray: ERD/ERS obtained with “fastICA”; in light gray: ERD/ERS obtained with “runica”. ....	112
Figure 5.6 – Left: Relative energy of the $\mu$ and $\beta$ bands of channel C3. The reference period was taken between 0 and 2 s and the index finger extension occurred between 4 and 6 s; Right: Periodogram of channel C3.....	114
Figure 5.7 – Left: Relative energy of the $\mu$ and $\beta$ bands of channel C3. The reference period was taken between 0 and 2 s and the mental task occurred between 4 and 6 s; Right: Periodogram of channel C3. ....	115
Figure 5.8 – Average ACF obtained during the motor mental task. ....	115
Figure 5.9 – Left: Ongoing average $\mu$ and standard deviation $\sigma$ calculated with time-windows up to 25 s during the right hand imagery task; Right: Ongoing average $\mu$ and standard deviation $\sigma$ calculated with time-windows up to 25 s during the sound imagery task.....	116
Figure 5.10 – Left: KPSS and ADF tests results for motor mental tasks; Right: KPSS and ADF tests results for non-motor mental tasks. ....	117
Figure 5.11 –Left: Mental task of right hand. The correlation curve, C-1, of channel C3 is shown by the black continuous line. The correlation curve, C-2, of channel C3 is shown by the gray continuous line. The square root of the SNR curve is shown by the gray dashed line, whose vertical axis is on the right side; Right: The $a$ value of the first part of C-1 is shown by the black line. The $a$ value of the second part of C-1 is shown by the gray line. ....	120
Figure 5.12 – Mental task of music imagery. The correlation curve, C-1, of channel T5 is shown by the black continuous line. The correlation curve, C-2, of channel T5 is shown by the gray continuous line. The square root of the SNR curve is shown by the gray dashed line, whose vertical axis is on the right side.....	121
Figure 6.1 – BCI schematic flow chart proposed in this Ph.D. Thesis.....	123
Figure A.1 – UDP packet sent by BNT36. ....	141

## Nomenclature

### Metric symbols

Symbol	Description	Name
$t$	Time	s
$f$	Frequency	Hertz
$v$	Electrical voltage	V
$\tau_m$	Time instant of the first ACF minimum	s
$T_S$	Sampling period	s
$F_S$	Sampling frequency	Hertz

### Greek letters

Symbol	Description	Unit
$\alpha$	Significance level	%
$\alpha, \beta, \delta, \theta, \mu$	Frequency bands of the EEG signal	Hz
$\gamma(j)$	j-th lagged autocovariance	-
$\gamma_1(P)$	skewness of a probability distribution P	U*
$\gamma_2(P)$	kurtosis of a probability distribution P	U*
$\nabla$	First difference operator	-
$\varepsilon$	White noise	-
$\mu_k$	Mean of a random variable of class $C_k$	U*
$\boldsymbol{\mu}_k$	Mean vector of random variables of class $C_k$	U*
$\xi$	Random walk	-
$\rho$	Resistivity	$\Omega m$
$\rho_{x_1 x_2}$	Correlation between variables $x_1$ e $x_2$	-
$\boldsymbol{\Sigma}_k$	Covariance matrix of $C_k$	-
$\sigma_k$	Standard deviation of a random variable of class $C_k$	U*
$\tau$	Temporal increment or also the time constant	-
$\varphi$	Parameter of the autoregressive model	-
$\Psi_X$	Characteristic function of the random variable $x$	-
$\Omega$	Long-run variance	-

\*Unit of the observed variable

**Other symbols**

<b>Symbol</b>	<b>Description</b>	<b>Example</b>
$\mathbf{C}_k$	Class $k$	$(k \in \mathbb{N})$
$d$	Number of dimensions of the class	$(d \in \mathbb{N})$
$D_{\text{KL}}(\mathbf{P}  \mathbf{Q})$	Kullback-Leibler Divergence between two probability distributions P and Q.	$(D_{\text{KL}} \in \mathbb{R})$
$f(\cdot)$	Algebraic function	$f(t)$
$g_k$	Discriminant function of class $\mathbf{C}_k$	$(g_k \in \mathbb{R})$
$k_i(\mathbf{P})$	$i^{\text{th}}$ cumulant of a probability distribution P	$(k_i \in \mathbb{R})$
$\mathbf{K}_x$	cumulant-generating function of the random variable $x$	-
$L$	Number of classes in the sample space	$(L \in \mathbb{N})$
$n$	Number of epochs	$(n \in \mathbb{N})$
$N_k$	Number of samples of class $\mathbf{C}_k$	$(N_k \in \mathbb{N})$
$p$	Autoregressive model order	$(p \in \mathbb{N})$
$P(\mathbf{C}_k)$	Priori probability of class $\mathbf{C}_k$	$(P(\mathbf{C}_k) \in \mathbb{R})$
$p(x)$	univariate distribution of the random variable $x$	$(p(x) \in \mathbb{R})$
$p(x,y)$	bivariate distribution of the random variables $x$ and $y$	$(p(x,y) \in \mathbb{R})$
$p(x,y,\dots)$	multivariate distribution of multiple random variables $x,y,\dots$	$(p(x,y,\dots) \in \mathbb{R})$
$P(x \mathbf{C}_k)$	Probability density function of class $\mathbf{C}_k$	$(P(x \mathbf{C}_k) \in \mathbb{R})$
$P(\mathbf{C}_k/x)$	Posteriori probability of class $\mathbf{C}_k$	$(P(\mathbf{C}_k x) \in \mathbb{R})$
$\mathbf{S}$	Sample Space	$(\mathbf{S} \in \mathbb{C})$
$w(\cdot)$	Bartlett Kernel	-
$x$	Event in the sample space (random variable)	$(x \in \mathbb{C})$
$\mathbf{x}$	Vector of random variables (with dimension $d$ )	$(\mathbf{x} \in \mathbb{C})$

**Superimposed symbols**

<b>Symbol</b>	<b>Description</b>	<b>Example</b>
$\text{T}$	Transpose	$\mathbf{A}^{\text{T}}$
-	Averaging operation	$\bar{\mu}$
$\wedge$	Clear signal in the absence of noise or an estimate variable	$\hat{\nu}$

**Subscribed symbols**

<b>Symbol</b>	<b>Description</b>	<b>Example</b>
$i, j$	Identification number or index	$a_{ij}$
$max$	Maximum value of a function	$max(g_{ck})$

**Acronyms**

<b>Symbol</b>	<b>Description</b>
ABCI	Affective Brain-Computer Interface
AC	Alternating Current
ACo	Acetylcholine
ALIS	Association of Locked-In Syndrome
AP	Action Potential
AR	Autoregressive Model
BCI	Brain-Computer Interface
BP	Bereitschaftspotential
BSS	Blind Source Separation
BCG	Ballistocardiogram
CAR	Common Average Reference
CCD	Cortical Current Density
cdf	Cumulative Distribution Function
CNS	Central Nervous System
CPM	Central Pontine Myelinolysis
CRP	Cornea-Retinal Potential
DA	Dopamine
DC	Direct Current
DOC	Disorders of Consciousness
DP	Discriminative Power
ECG	Electrocardiogram
ECoG	Electrocorticogram
EEG	Electroencephalogram
EMG	Electromyogram
EOG	Electrooculogram
EP	Evoked Potential

**Acronyms** (continuation)

<b>Symbol</b>	<b>Description</b>
EPSP	Excitatory Post-Synaptic Potential
ERD	Event Related Desynchronization
ERP	Event-Related Potential
ERS	Event Related Synchronization
ESD	Energy Spectral Density
fMRI	functional Magnetic Resonance Imaging
GABA	Gamma-Aminobutyric Acid
Glu	Glutamate
Gly	Glycine
GPL	General Public License
HAC	Heteroscedastic and Autocorrelation Consistent
hBCIs	hybrid Brain-Computer Interfaces
HDD	Hard Disk Drive
HFO	High-Frequency Oscillations
HOS	High Order Statistical Separation
ICA	Independent Component Analysis
IPSP	Inhibitory Post-Synaptic Potential
IT	Inferior Temporal Cortex
IV	Intertrial Variance
LDA	Linear Discriminant Analysis
LED	Light-Emitting Diode
LFP	Local Field Potential
LG	Lateral Geniculate Nucleus of the thalamus
MEG	Magnetoencephalography
MMI	Minimization of Mutual Information
MCS	Minimally Conscious State
MG	Medial geniculate nucleus of the thalamus
MRI	Magnetic Resonance Imaging
MRP	Movement-Related Potential
MSE	Mean Square Error
NA	Noradrenaline

**Acronyms** (continuation)

<b>Symbol</b>	<b>Description</b>
NIRS	Near-Infrared Spectroscopy
OLS	Ordinary Least Squares Regression
PET	Positron Emission Tomography
PDF	Probability Density Function
PMA	Premotor Area
PNS	Peripheral Nervous System
PSD	Power Spectral Density
PSP	Post-Synaptic Potential
PVS	Persistent Vegetative State
QDA	Quadratic Discriminant Analysis
RAM	Random-Access Memory
REM	Rapid Eye Movement
RP	Readiness Potential
RPE	Retinal Pigment Epithelium
SDK	Software Development Kit
SFA	Signal Fraction Analysis
SMA	Supplementar Motor Area
SNR	Signal to Noise Ratio
ssBCI	single-switch BCI
SSVEP	Steady-State Visual Evoked Potential
STFT	Short Time Fourier Transform
TCR	Thalamic Relay Cells
TRN	Thalamic Reticular Nucleus
VHFO	Very High-Frequency Oscillations
VL	Ventral Lateral nucleus of the thalamus
VNS	Vegetative Nervous System
VP	Ventral Posterior nucleus of the thalamus
VPL	Ventral posterolateral nucleus of the thalamus
VPM	Ventral posteromedial nucleus of the thalamus
VS	Vegetative State
WSS	Wide Sense Stationarity

## Chapter 1 : Introduction

The research presented in this thesis studies the development of a Brain-Computer Interface (BCI) architecture based on the electroencephalographic signal (EEG) by using motor related mental tasks as well as other paradigms like sound imagery. BCIs may use the voluntary modulation of the neural activity to transmit information that can be used for communication or control. The measurement of the self-controlled neural activity can be performed invasively, e.g., by performing single-unit recordings, which are the measure of single-neuron activity and local field potentials using a microelectrode system, by using the measure of multiple neuron activity using microelectrode arrays, or by using electrodes placed directly on the exposed surface of the brain to record electrical activity from the cerebral cortex, that is the Electrocorticography (ECoG) (Lebedev & Nicolelis, 2006).

The measurement of the self-controlled neural activity can be performed non-invasively, e.g., by using functional Magnetic Resonance Imaging (fMRI), Magnetoencephalography (MEG), Positron Emission Tomography (PET) and EEG signal. Recent studies have succeeded in demonstrating that EEG-based BCIs may be used to control robotic devices (del R. Millán et al., 2004; Ferreira et al., 2008; Müller et al., 2013). For a detailed review about BCIs see (Wolpaw et al., 2002; Wolpaw, 2007; Cincotti et al., 2008; He et al., 2013).

### 1.1 Motivation

BCIs have been primarily conceived as a potential new therapy to restore motor control in severely disabled patients, particularly those suffering from devastating conditions such as amyotrophic lateral sclerosis (ALS), spinal cord injury, stroke and cerebral palsy. As this technology advances, BCIs might also hold promise for amputees, by controlling limb prostheses. BCIs dedicated to the restoration of locomotion and speech are emerging applications (Lebedev & Nicolelis, 2006).

BCI applications are currently being used, e.g., for: (i) assistance for patients with severe motor disabilities; (ii) diagnosis of Disorders of Consciousness (DOC); (iii) entertainment applications; (iv) recognition of affective or cognitive states and rehabilitation therapy (v). Not only BCIs are used for the applications mentioned above,



but also hybrid Brain-Computer Interfaces (hBCIs) are being used to increase the reliability of standard BCIs. The development BCIs for disabled people should allow them to use all their remaining functionalities as control possibilities and to use the currently best available ones. For example, for subjects that can control the movement of the eyes the Steady-State Visual Evoked Potential (SSVEP)-based BCIs can be used.

Indeed, Pfurtscheller et al. propose an hBCI to control a hand orthosis, which is composed of a single-switch BCI (ssBCI) based on the motor imagery paradigm and a SSVEP-based BCI. The ssBCI is used to activate and deactivate the light-emitting diodes (LEDs) of the SSVEP-based BCI, which controls the orthosis via gazing at a 8 Hz LED to open it and gazing at a 13 Hz LED to close it (Pfurtscheller, et al., 2010). Sometimes muscular activity would be available and hBCIs may include different kinds of biological signals like the electrocardiogram (ECG) or the electromyogram (EMG) (Leeb et al., 2010; Shahid et al., 2011).

(i) BCI applications for assistance are mostly directed to people in a situation called total Locked-in Syndrome<sup>1</sup> (LIS), or pseudocoma. The next paragraphs will, then, briefly describe the types of LIS, which were the original motivation behind the development of BCIs. Bauer et al. (1979) subdivided the syndrome on the basis of the extent of motor impairment as “classical LIS”, characterized by total immobility except for vertical eye movements or blinking; “incomplete LIS”, in which there are remnants of voluntary motion, and “total LIS” that consists of complete immobility including all eye movements combined with preserved consciousness.

Patients with incomplete and classical LIS may use Human Machine Interfaces (HMIs) adjusted to their specific needs and these devices can be as simple as a head pointer going up to electronic interfaces controlled by biological electrical signals such as surface myoelectric (EMG) and electrooculographic (EOG) signals. The user, for example, can control the interface through myoelectric signals of muscle movements of the face such as eye blinking, or through electrooculographic signals from eyeball movement. But people with total LIS may only use BCIs to communicate their thoughts to those around them by modulating their own neural activity. The Association of Locked-In Syndrome (ALIS) database shows that some sort of HMI is used by 81% of the LIS patients (Laureys, et al., 2005).

---

<sup>1</sup> LIS was defined in 1966 by Fred Plum and Jerome Posner to describe the quadriplegia and anarthria resulting from the disruption of corticospinal and corticobulbar pathways, respectively, in brainstem damage.

The most common causes of LIS are stroke or brain hemorrhage, traumatic brain injury, motor-neuron diseases or Medication overdose. Among them, the most common etiology of LIS is vascular pathology. Another important cause of total LIS can be observed in end-stage Amyotrophic Lateral Sclerosis (ALS) and Duchenne Muscular Dystrophy (DMD), i.e., motor-neuron diseases. But, LIS may be caused either by brainstem tumor, encephalitis, Central Pontine Myelinolysis (CPM), vaccine reaction and prolonged hypo-glycemia (Laureys, et al., 2005). Most LIS patients, with appropriate medical care, can return home and their life expectancy is about several decades. Once a person has medically stabilized in LIS for more than one year, 10 year-survival is 83% and 20 year-survival is 40% (Laureys, et al., 2005). Even if the chances of motor recovery are very limited, computer-based communication methods, HMIs or BCIs, have substantially improved the quality of life in chronic locked-in syndrome (Laureys, Owen & Schiff, 2004).

Julia Tavalaro, Jean-Dominique Bauby and Philippe Vigand are good examples of LIS patients who maintained an active and productive life. In 1966, Julia Tavalaro suffered two strokes and fell into a coma for 7 months. She was misdiagnosed as being in a vegetative state for 6 years, until being considered to have LIS in 1973. She wrote the book "Look Up for Yes" in 1997. In 1990, Philippe Vigand had a vertebral artery dissection and remained in a coma for 2 months. In 2000, he wrote "Only the Eyes Say Yes" and he has written his second book, "Dealing with the Menaced French Ecosystem" in 2002. Jean-Dominique Bauby had a brain stem stroke in December of 1995 and remained in a coma for several weeks. He created the Association of Locked-In Syndrome (ALIS) and wrote the book "The Diving Bell and the Butterfly", which became a best-seller. ALIS has registered 367 locked-in patients just in France (Laureys, et al., 2005).

Regarding BCIs applied to severe LIS patients worth quoting the cases of Elias Musiris and Erik Ramsey. In 2002, Elias Musiris, a patient with chronic ALS was the first total LIS person to regain some measure of communication through EEG-based BCI, developed by neurological researcher Niels Birbaumer. In 1999, 16-year-old Erik Ramsey suffered a brainstem stroke after a car crash. He remained in coma for three weeks and was diagnosis with classical LIS. In 2004, he had a microelectrode inserted into the part of the motor cortex responsible for the movements involved in speech and the ground wire connected to the Dura mater, the outermost of the three layers of the meninges that surround the brain and spinal cord. The electrode captured the

extracellular electricity of about forty neurons and the signal was transmitted wirelessly under the scalp to a computer to be decoded, translated and synthesized into single vowels.

(ii) A common pattern that can be observed in the people described above is to have undergone an early stage of coma. In fact, the misdiagnosis between Vegetative State (VS) and Minimally Conscious State (MCS) is around 40%, which brings us to the second kind of application using BCIs, that is to improve DOC diagnosis (Laureys, 2007; 2005; Gantner, et al., 2013; Decoder, 2013). The next paragraphs describe the common progress of a victim of brain damage to exemplify how the VS and MCS arise and are common misdiagnosed. Some emphasis is given to the role of the EEG in the current diagnosis of brain death and the progress of using this type of signal to build BCIs systems able to identify people that are just minimally aware.

After a stroke or traumatic brain injury the patient usually remains in a coma. To clearly distinguish a coma from syncope (fainting), concussion, or other states of transient unconsciousness, a coma must persist for at least 1 h. Then, a coma is a time-limited condition leading either to brain death, vegetative state, recovery of consciousness or LIS, in rare cases. Brain death can be diagnosed with an extremely high rate of probability within hours to days of the original injury. The diagnosis performed with the EEG is the most validated test and, because of its wide availability, preferred confirmatory test for brain death implemented in many countries' guidelines. The EEG in patients with brain death shows an absence of electrocortical activity, and the EEG signal becomes isoelectric, that is flat line, which is similar to a "functional decapitation". The EEG confirmatory test for brain death has sensitivity and specificity of 90% (Laureys, Owen & Schiff, 2004).

The term Vegetative State was defined in 1972 by Bryan Jennett and Fred Plum for patients with "wakefulness without awareness" of themselves or their environment. One month after the occurrence of brain damage, the vegetative state is declared persistent, but does not mean that it is irreversible. The term Permanent Vegetative State was defined in 1994 by the US Multi-Society Task Force on Persistent Vegetative State (PVS) and does imply that the patient will not recover. The VS may arbitrary be regarded as a Permanent VS three months after a nontraumatic brain injury and twelve months after a traumatic injury and does imply that the patient will not recover. However, after being in the VS the patient can also progress to the Minimally Conscious State (MCS), which is an intermediate state between full awareness, as found

in LIS patients and no awareness at all, as found in the VS patients (Laureys, Owen & Schiff, 2004; Laureys, 2005).

An important difference is that patients who have remained in the MCS for years still have a chance of recovery. In a much publicized case, Terry Wallis, who was considered to be in a VS since a road accident in 1984, was actually in MCS for 19 years and started talking in 2003. Wallis also regained some ability to move his limbs, although he can not walk and still needs persistent care (Laureys, 2007; Gantner, et al., 2013).

For example, in July 2005, a 23-year-old woman sustained a severe traumatic brain injury as a result of a road traffic accident. She remained comatose for more than a week and then evolved to the VS during the five following months. Even though she fulfilled all of the criteria for a diagnosis of VS according to international guidelines, the investigators conducted a second study in which they asked her to perform mental imagery tasks. When she was asked to imagine playing a game of tennis, the fMRI scans showed activity in the Supplementary Motor Area (SMA) of her brain. When she was asked to imagine walking through the rooms of her house, the scans showed activation of the network involved in spatial navigation. Despite the clinical diagnosis that the patient was in a vegetative state, she understood the tasks and repeatedly performed them and hence must have been conscious (Laureys, 2007; Owen, et al., 2006; Gantner, et al., 2013).

Similar studies are being conducted with EEG-based BCIs, which have the advantage of being cheaper, portable and possible to use at the patient's bedside. Monti et al. (2010) demonstrated that a DOC patient was able to use the modulation of his brain activity to reliably answer 'yes' or 'no' to simple questions, even though no signs of communication had ever been found through bedside examination. EEG studies measuring effective connectivity in the  $\alpha$  (8-12 Hz) and  $\beta$  (14-30 Hz) frequency bands seem able to differentiate between VS and MCS patients. Effective connectivity is a measure of the causal relationship between brain areas. Additionally, the EEG entropy was shown to be able to differentiate acute unconsciousness from MCS patients with 89% sensitivity and 90% specificity. However, the prognostic value of this measure was not high and hence can not be recommended as a prognostic tool (Gantner, et al., 2013).

The EEG is already very important to the confirmatory test of brain death and is also becoming important as a paradigm for single-switch BCIs that would improve the reliability of VS and MCS diagnosis. Single-switch BCIs are simpler BCIs that operate

with only two mental tasks, in which one of them is the absence of making any particular mental task, as used by Monti et al. (2010). These simpler BCIs are proving useful to confirm the patient awareness. In fact, there is a recent European collaborative project named DECODER (2010-2013) which aims to deploy ssBCIs for the detection of consciousness in non-responsive patients and greatly improve DOC diagnosis. DECODER project will use ssBCIs based on EEG and Near-Infrared Spectroscopy (NIRS), which also can be applied at the patients' bedside (Decoder, 2013).

The American Academy of Neurology (AAN) has published a position statement, in 1993, concerning that LIS patients have the right to make health care decisions about themselves, including whether to accept or refuse life-sustaining therapy, either by not starting it or not stopping once started (Gantner, et al., 2013). In addition, through BCIs these patients can finally express their preferences in terms of treatment planning, like pain management or end-of-life decision-making (Laureys, et al., 2005).

(iii) Entertainment applications are a relatively new branch in the field of BCIs that are intended for healthy people who want to control games and devices through BCIs. Some companies that are engaged in BCI products like interfaces, Software Development Kits (SDK) and games are Interactive Productline<sup>®</sup>, OCZ Technology<sup>®</sup>, Emotiv<sup>®</sup>, NeuroSky, Inc and PLX Devices<sup>®</sup>.

For a short review, in 2003 the Swedish Company Interactive Productline<sup>®</sup> developed the game Mindball<sup>®</sup>, in which players compete to control a ball's movement across a table by modulating their brain waves, becoming more relaxed or focused. The manufacturer of computer hardware, OCZ Technology<sup>®</sup>, developed in 2008 the computer game controller, nia<sup>™</sup> (Neural Impulse Actuator), based on facial EMG and EEG. The neuroengineering company Emotiv<sup>®</sup> has brought to market in 2009 a low cost EEG interface called EPOC<sup>®</sup> that is able to play games specifically developed for it, or use it to connect to a computer to play games or control devices. NeuroSky, Inc. is a BCI company that in 2009 developed the EEG-based headset called Mindset<sup>®</sup>, and the compatible toys Mindflex<sup>®</sup> and Star Wars Force Trainer<sup>®</sup>, in which players lift a ball by concentrating. In 2011, NeuroSky, Inc. launched a new headset called Mindwave<sup>®</sup>. In 2011, PLX Devices<sup>®</sup> launched the EEG-based headset XWave Sonic<sup>™</sup> and the EEG-based headband XWave Sport<sup>™</sup> for EEG use and analysis in computer systems.

(iv) Affective Brain-Computer Interfaces (ABCIs) are an approach of affective computing directed to BCIs. Affective computing is a branch of computer science

which originated about 1995 related to the study and development of systems that can recognize, interpret, process, and simulate human affects. Affective computing may use several kinds of features to perform the recognition of human affects, such as facial image, body gesture image, blood volume pulse, galvanic skin response, facial EMG and EEG. The common basic emotions that are used for recognition are: anger, disgust, fear, happiness, sadness and surprise.

ABCIs usually use a more limited range of features than affective computing, just taking the features that were previously used in the BCI system. Often, these features are only the EEG and the facial EMG. Actually, ABCIs intend to perform the automatic recognition of attention or fatigue that would be used to adapt the BCI to the user state and improve the success rate of the BCI during the identification of the mental tasks.

As exemplified in the preceding paragraphs, most BCI applications are intended for people with disabilities. As each individual has their own skills and preferences, some mental tasks can be easily performed by some and evoke a good pattern for classification, while others may have difficulty or do not evoke a pattern at all. Within this context, the motivation for this Ph.D. Thesis is to find new ways to control BCIs and also to propose a BCI with minimal empirical parameters. The chance of finding a better match between the user and the BCI increases by using a wider variety of mental tasks.

## **1.2 Objectives**

The BCIs are platforms that can be understood as the integration of two main processes which are the signal acquisition and the signal processing (Figure 1.1). Regarding the signal acquisition it is important to define a standard that is used for the placement of the electrodes on the scalp and the sampling rate of the system. The signal processing stage comprises the signal pre-processing, the feature extraction, the pattern classification and the translation of the mental task to commands for a BCI application. The signal pre-processing stage is intended to reduce the amount of noise that contaminates the EEG signal and it usually uses spatial filters or High Order Statistical Separation methods. The feature extraction stage focuses on finding the main features that differentiate the mental tasks, and this stage can be followed by a feature selection

step to refine the search for the best features. Then, the EEG features are sent to a classifier whose output is translated into commands for a BCI application.

This present research has four main objectives. The first goal is to study the statistical properties of the EEG, like the EEG Probability Distribution Function (PDF), the EEG stationarity, the correlation and the Signal-to-Noise Ratio (SNR), in order to propose a system with minimal empirical and well-founded parameters for online classification. This statistical analysis estimates the EEG sampling rate and the length of the time windows used thenceforth, and then, covers the first stage of the BCI timeline shown in Figure 1.1.

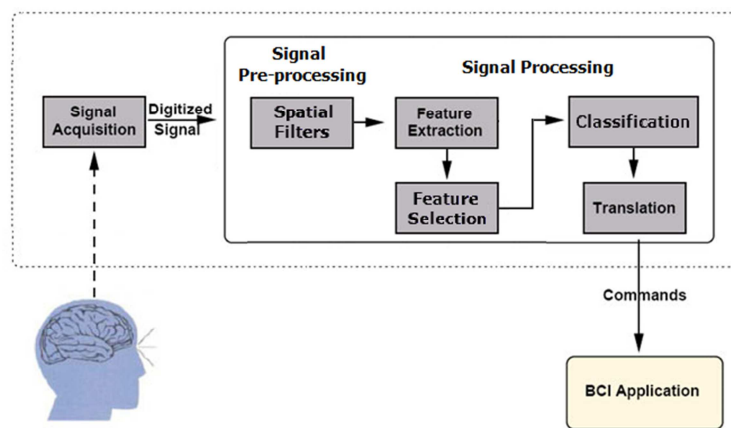


Figure 1.1 – BCI timeline.

The second objective is to make the BCI training step non-supervised and independent of the chosen mental task paradigm. Most BCIs use the motor imagery paradigm, i.e., the user has to imagine the movement of the hands, sometimes also including the movement of the legs due to the prior knowledge of the physiological aspects of motor related mental tasks (Blankertz et al., 2007). It is known that the energy of specific bands of frequencies measured on the motor cortex undergo changes during the imagination of movement, which is called Event Related Synchronization/Desynchronization (ERD/ERS) (Pfurtscheller et al., 1999). These known patterns are, then, used for the identification of motor related mental tasks. Other studies have used non-motor tasks, such as thinking of words beginning with the same random letter (Anderson et al. 2007) or repetitive subtraction (Obermaier et al. 2001).

There are classifiers, with or without the training step, in which the training can be non-supervised or supervised. However, most common BCIs use some prior knowledge of the physiological mental tasks to train its classifier either directly or indirectly with supervised training. This second goal of making the BCI training step non-supervised and independent of the chosen paradigm would, then, allow the system to be independent of some prior knowledge of the physiology of the mental tasks. Most physiological research report the average behavior from subjects, then even if these physiological characteristics related to mental tasks are known, the BCI would not be suited to take into account individual bias. As the proposed method is based only on the discriminative capacity of the EEG features, the BCI would, then, be adapted for each user. For this purpose methods for automatic selection of features were studied so that the BCI here developed could have automatic adjustment for mental tasks of any paradigm chosen by the user.

The third goal of this research is to study the use of non-motor mental tasks like sound imagery, also called audiation (Zeki and Marini, 1998; Gegenfurtner and Kiper, 2004) for BCI applications. Some recent efforts in this area were presented by Dr. Schaefer's group, comparing Evoked-Potentials (EPs) during perception and imagery of rhythms, and also the  $\alpha$  band (8-13 Hz) activity of the EEG during perception and imagery of music (Schaefer, Vlek & Desain, 2011a; 2011b). Dr. Schaefer's group was able to identify perceived and imagined music through offline single-trial EEG classification (Schaefer et al., 2011c). On the other hand, Klonowski et al. (2009) proposed a method to identify different inner tones, or imagined tones, by using high-resolution EEG and analyzing the high-frequency spectrum, and a comparison between music and motor imagery can be seen in Soriano et al. (2013).

Then, in order to investigate the possibility of extending the BCI to operate with both, motor and sound imagery paradigms, five mental tasks were used, which were the imagination of the movement of right and left hands, of both feet, of rotation of a cube and of music imagery. The traditional method to obtain the ERD/ERS, suggested by Pfurtscheller et al. (1999), was implemented and an analysis of the EEG SNR was performed. This analysis was performed in order to estimate the number of epochs necessary to observe the ERD/ERS pattern during the mental tasks with these two kinds of paradigms, the motor and non-motor related mental tasks. As distinct mental tasks activate different brain areas, the ERD/ERS pattern obtained over the scalp should vary according to the mental task. The SNR and the differences between ERD/ERS scalp



maps of the five mental tasks are used here as a factor in making a decision about choosing new tasks to be used in the BCI.

The fourth goal of this thesis is to test algorithms for minimization of the artifacts caused by eye blinks and eye movements. These algorithms will be implemented to work online in the BCI pre-processing step; therefore, some simple methods like threshold analysis for artifact discard and EEG filtering were compared to a more complex method which is to perform Blind Source Separation (BSS) by using High Order Statistical Separation (HOS) methods. For this purpose the Independent Component Analysis (ICA) is tested for artifact reduction (Croft & Barry, 2000, Jung et al., 2000, Jung et al., 2001, Ford et al., 2004). There are two broadest definitions of independence for the ICA, next, the most employed algorithms of each approach were tested. Finally, the processing time of the techniques of artifact removal studied were calculated in order to evaluate whether it is possible to adapt the algorithms to an online approach.

### **1.3 Thesis structure**

Chapters 2 and 3 comprise the electrophysiological theoretical background. Chapter 2 describes the human brain and Chapter 3 describes the genesis of the EEG signal. The origin of the oscillatory activity and the main EEG rhythms are described in order to explain the ERD/ERS and the physiological aspects of motor related mental tasks. Chapter 3 explains the EEG acquisition process, the formation of the EEG channels, the methods for avoiding and minimizing artifacts, the types of EEG records and the EEG SNR. The examples in this chapter used our own data and simulations to verify the results from the literature.

Chapter 4 shows the results obtained with statistical tests and simulations to achieve the four main aforementioned objectives. All techniques were initially tested on an EEG database available on the internet that is shown in Chapter 4. Then, Chapter 5 shows the test protocol and the results of applying the techniques shown in Chapter 4 with our own data. Finally, Chapter 6 presents the conclusion and suggestions for further research.

## Chapter 2 : The human brain

The purpose of this chapter is to describe the human brain anatomically and physiologically, so as to better understand some of the patterns observed in the EEG signal that are used to distinguish the distinct mental tasks that control the BCI.

The nervous system coordinates and monitors all conscious and unconscious activity of body. It comprises the Central Nervous System (CNS) and the Peripheral Nervous System (PNS). The CNS consists of the brain and spinal cord. The PNS consists of nerves<sup>2</sup> and ganglia<sup>3</sup>, which are outside of the brain and spinal cord, and terminal organs (Bear et al. 2008). Upcoming sections deal with CNS and its main constituent, the brain.

### 2.1 Section planes and reference points of the human brain

The relative position of the brain structures is located through section planes and reference points. Then, this section will cover some terms used throughout the thesis to locate and describe brain structures. The front portion of the brain with respect to the body is called the anterior portion, and the rear portion is called the posterior portion. The top portion is called the dorsal portion and the bottom portion is called the ventral portion. Figure 2.1 shows the directions and the three section planes that are the sagittal, coronal and horizontal planes. The structures nearest to the medial line are called medial structures and structures furthest from the medial line are called lateral structures. Moreover, the structures that are on the same side of the medial line are called ipsilateral to each other, and the structures that are on opposite sides of the medial line are called contralateral to each other. Finally, the similar structures that are on both sides of the medial line are called bilateral.

The brain surface is composed of numerous circumvolutions. The circumvolutions are the evolutionary result of the brain's attempt to increase its cortical area, being confined to the skull. The protrusions are called gyri and the grooves are called sulci; very deep sulci are called fissures. The exact pattern of gyri and sulci may

---

<sup>2</sup> Groupings of axons in the PNS. Only one group of CNS axons is referred to as a nerve, which is the optic nerve (Bear, et al., 2008).

<sup>3</sup> From the Greek word "node". Agglomerate cell bodies of neurons found outside the CNS (Bear et al. 2008).

vary considerably from individual to individual, but many features are common to all human brains.

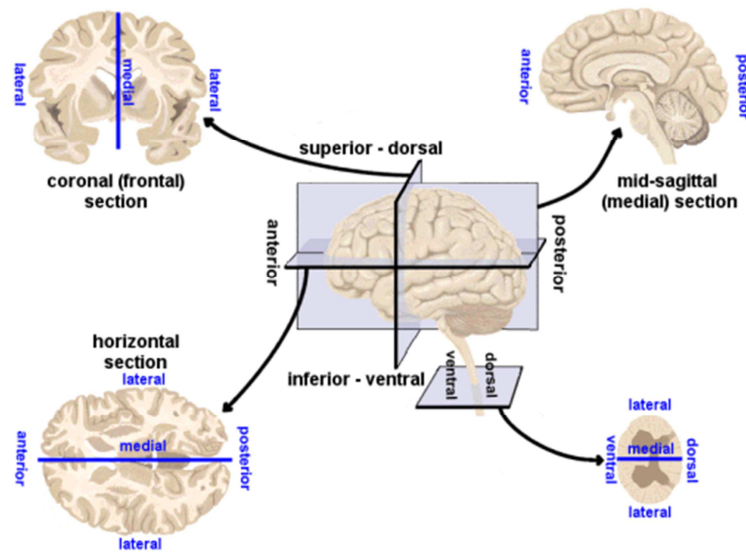


Figure 2.1 – Section planes and reference points of the human brain (Russell, 2013).

By convention, the brain is divided into lobes, named in relation to the underlying skull bones (Figure 2.2 - Left). The central sulcus separates the frontal lobe from the parietal<sup>4</sup> lobe. The lateral sulcus, or Sylvian fissure<sup>5</sup>, separates the frontal lobe and the temporal<sup>6</sup> lobe. The occipital<sup>7</sup> lobe is located on the caudal region of the brain, and is surrounded by the parietal and temporal lobes (Figure 2.2 - Right) (Bear, et al., 2008).

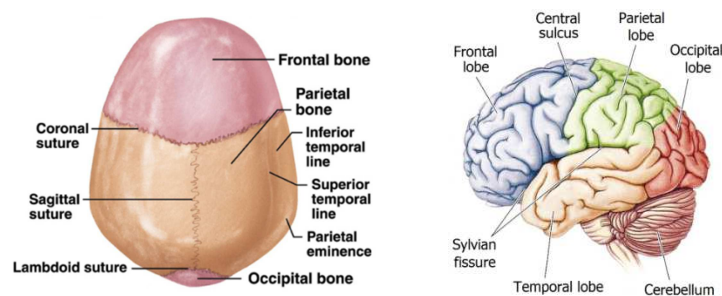


Figure 2.2 – Left: Skull bones; Right: Location of the four brain lobes (adapted from Bear, et al., 2008).

<sup>4</sup> The term “parietal” is derived from Latin, “*parietālis*”, meaning wall.

<sup>5</sup> Assigned in tribute to Franciscus Sylvius (1614-1672), who was a Dutch physician and scientist.

<sup>6</sup> The term temporal arises from Latin “*tempus*” meaning time. The word time was used for this region because it is typically on the sides of the skull where hair first becomes gray, showing the ravages of time.

<sup>7</sup> The term occipital means something situated near the “*occiput*”, which is derived from Latin prefix “*ob*” at the back of combined with “*caput*”, head.

The temporal lobe receives and processes auditory information and it is related to object identification and naming. The frontal lobe, including the motor, the premotor and the prefrontal cortices, is involved in planning actions and movement, as well as abstract thought. The parietal lobe is the primary somatosensory cortex and receives information about touch and pressure from the thalamus. The occipital lobe receives and processes visual information (Guyton & Hall, 2006).

The cerebral surface or cortex<sup>8</sup> is organized like a patchwork quilt. These areas were first identified and numbered by Brodmann<sup>9</sup> (Figure 2.3 - Left). The main areas related to the processing of the senses are: the primary motor cortex, or M1 (area 4), the Supplementary Motor Area (SMA) and Premotor Area (PMA) (area 6) in the frontal lobe; the primary somatosensory cortex, or S1 (areas 1, 2 and 3), and the primary gustatory cortex (area 43) in the parietal lobe; the primary auditory cortex, or A1 (areas 41 and 42) and the olfactory cortex in the temporal lobe and the primary visual cortex, or V1 (area 17) in the occipital lobe.

In the context of the mental tasks analyzed in this research, the areas 4 (M1) and 6 (SMA and PMA) are related to motor mental tasks and are especially important. The areas 39 and 40 (Wernicke's area) and 44 and 45 (Broca's area) are related to the tasks of imagining/remembering words. The areas 41 and 42 (A1) are related to music imagery tasks and the area 17 (V1) is related to visual tasks (Figure 2.3 - Right).

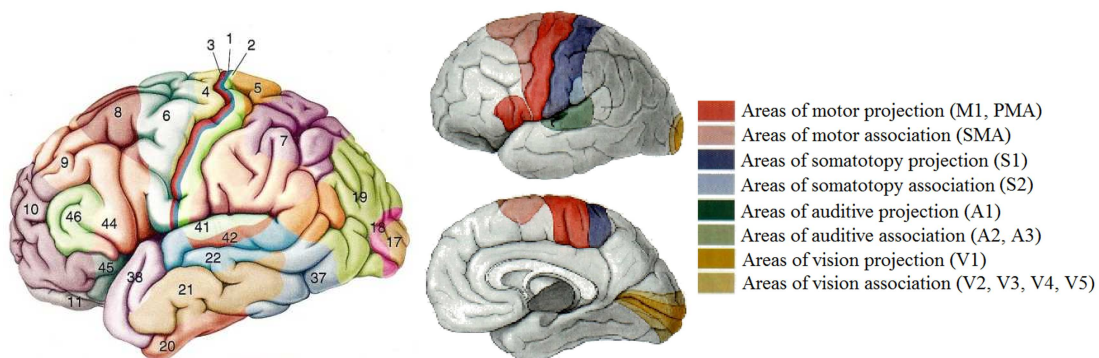


Figure 2.3– Left: Brodmann's cytoarchitectonic map (Bear, et al., 2008); Right: Main areas related to the processing of the senses.

<sup>8</sup> The term "cortex" is derived from Latin meaning "bark" (Bear, et al., 2008).

<sup>9</sup> Korbinian Brodmann (1868-1918) was a German neurologist and psychiatrist responsible for the subdivision of the cerebral cortex in 47 functional areas, called Brodmann areas, which were numbered according to the sequence in which he studied them (Bear, et al., 2008).

## 2.2 Description of the S1, M1, A1, V1 areas, Wernicke's area and Broca's area

The primary motor cortex is directly responsible for the coordination of voluntary movements. The left side of Figure 2.4 (in red) shows the somatotopic<sup>10</sup> map of M1, which correlates some M1 areas with the control of body parts. It is worth noting that more than half of M1 comprises the area controlling the muscles of the hands and the muscles of speech (Guyton & Hall, 2006).

The right side of Figure 2.4 (in blue) shows the somatotopic map of S1, correlating areas of the somatosensory cortex with the sensitivity of various areas of the body. Note that the somatotopical organization of the human pre-central gyrus (M1) is very similar to that observed in somatosensory areas of the postcentral gyrus (S1). This research will be measuring, through EEG electrodes, the electrophysiological changes in areas corresponding to the movement of the hands and feet in the pre-central gyrus, since this same area in the postcentral gyrus corresponds to the sensitivity of touch, pressure and temperature of such members.

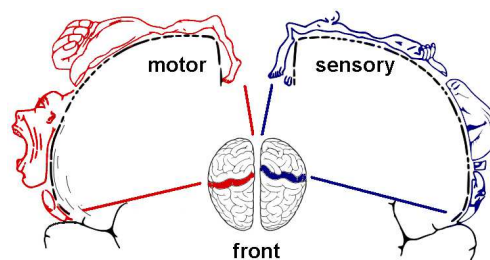


Figure 2.4 – Left: Somatotopic map of human pre-central gyrus (M1); Right: Somatotopic map of human postcentral gyrus (S1).

The premotor area (PMA) has the function of supporting the movements generated by the M1 cortices of both hemispheres. The premotor area, or premotor cortex, performs the motor planning which is a “simulation” of the muscular movement to be performed. The signs associated with the motor planning are directly sent from PMA to M1 to excite multiple muscle groups related to accomplishment of the task (Bear, et al., 2008).

Human studies performed by Danish Neurologist Per Roland using Positron Emission Tomography (PET) to track changes in cortical activation patterns that follow

<sup>10</sup> The mapping of the body surface sensations or the control of body movement in a CNS area is called somatotopy (Bear, et al., 2008).

voluntary movements showed that performing finger movements increases blood flow in the following regions: somatosensory areas, posterior parietal cortex, portions of prefrontal cortex and the areas M1, SMA and PMA (Roland, et al., 1980). When participants were asked to just mentally imagine the movement without actually moving the fingers, area 6 (SMA and PMA) remained active, while area 4 (M1) did not remain active (Bear, et al., 2008).

Language processing, comprehension and speech production occur in the Broca's area, while the association and interpretation of information occur in the Wernicke's area (Figure 2.5 - Left), which plays a very important role during the chaining of the discourse. This area allows us to understand what others say and it also provides the ability to organize the words in a syntactically correct way. The Broca's area is located in the left hemisphere in 95% of persons (Guyton & Hall, 2006).

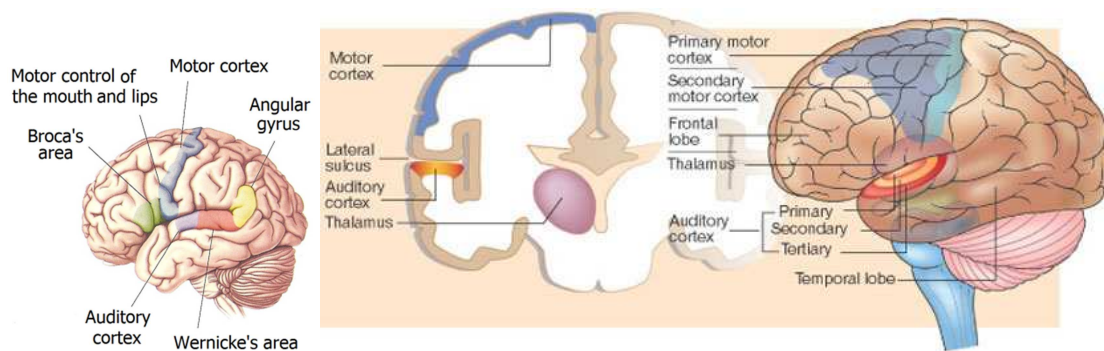


Figure 2.5 – Left: Location of Broca's area and Wernicke's area (adapted from Bear, et al., 2008); Right: primary, secondary, and tertiary auditory cortex.

The primary auditory cortex (A1) is the first cortical region of the auditory pathway, and it is directly connected with the medial geniculate nucleus of the thalamus (MGN). It roughly corresponds with the Brodmann areas 41 and 42, and it is located in the temporal lobe. This cortex area is the neural crux of hearing and, in humans, of language and music. The right auditory cortex has long been shown to be more sensitive to tonality, while the left auditory cortex has been shown to be more sensitive to minute sequential differences in sound, such as in speech. The auditory cortex is divided into three separate parts: the primary, secondary, and tertiary auditory cortices. These structures are formed concentrically around one another, with the primary cortex in the middle and the tertiary cortex on the outside (Figure 2.5 - Right).



The primary auditory cortex is tonotopically<sup>11</sup> organized, which means that neighboring cells in the cortex respond to neighboring frequencies forming a “frequency map”. This area of the brain is thought to identify the fundamental elements of music, such as pitch and loudness. The secondary auditory cortex (A2) has been indicated in the processing of harmonic, melodic and rhythmic patterns. The tertiary auditory cortex (A3) supposedly integrates everything into the overall experience of music and remembering a sound stimulus only faintly activates the tertiary auditory cortex.

The visual information processing begins with the sensitizing of photosensitive cells in retina, which sends information through the optic nerve to the thalamus area called the lateral geniculate nucleus<sup>12</sup> or body (LG). The LG then modulates and transmits visual information to the striate cortex or the primary visual cortex (V1). Visual areas are subdivided into the V1, V2, V3, V4 and V5 areas (Figure 2.6). The V5 area is also known as the visual area MT (middle temporal). The V1 projections extend to V2, V3 and V5 areas. The V4 area is related to the perception of shape and color, and the inferior temporal (IT) cortex is related to visual memory and recognition of human faces.

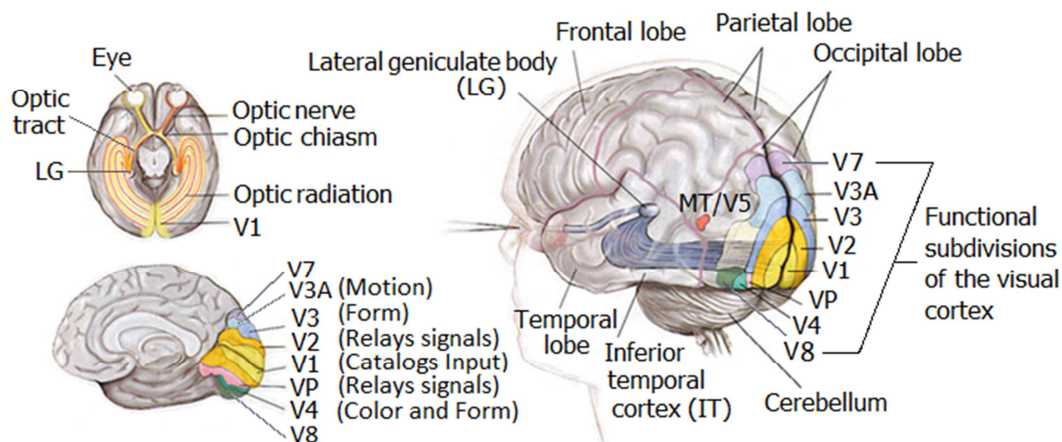


Figure 2.6 – Visual information path from retina to visual cortex (adapted from Claffey, 2013).

<sup>11</sup> Tonotopy is the spatial arrangement of where sounds of different frequency are processed in the brain. Tones close to each other in terms of frequency are represented in topologically neighbouring regions in the brain. Tonotopic maps are a particular case of topographic organization, similar to somatotopy in somatosensory areas and retinotopy in the visual system.

<sup>12</sup> The lateral geniculate nuclei are formed by six layers of overlapping cells which curve around the optic tract, as the articulation of a knee. From this fact derives the name geniculate, “*geniculatus*” from Latin, meaning “like a little knee” (Bear, et al., 2008).

### 2.3 Pyramidal tract and the contralaterality of motor movements

This section will discuss the contralaterality of motor movements. This means that the motor area in the right cerebral hemisphere controls the voluntary movements of the left side of the body, conversely, the motor area in the left cerebral hemisphere controls the voluntary movements of the right side of the body. The imagination of movement of the right hand is thereby being processed in the primary motor cortex of the left hemisphere.

The Somatic Motor System and Vegetative Nervous System (VNS) are all neural eferences of CNS. The brain sends signals for muscle control and receives sensory information through 12 pairs of cranial nerves and 31 pairs of nerves in the spinal cord (Figure 2.7 - Left). Axons that carry stimulatory signals from the brain to effector organs such as muscles and glands, through the spinal cord, are primary efferent<sup>13</sup> nerves of the somatic motor system. Primary efferent nerves enter the spinal cord through ventral roots. Axons that carry information from the sensory receptors of the skin, muscles and joints to the brain, through the spinal cord, are the primary afferent<sup>14</sup> nerves of the somatic sensory system. Primary afferent nerves enter the spinal cord through dorsal roots. Thus, the two roots of the spinal cord transmit information in opposite directions (Bear, et al., 2008).

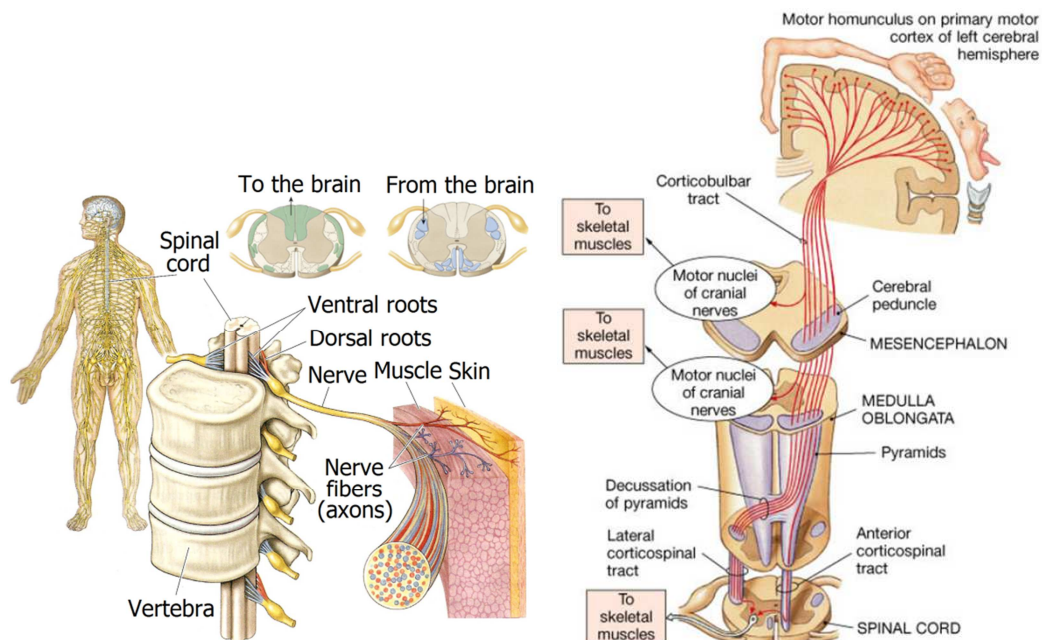


Figure 2.7 – Left: Spinal nerves and spinal nerve roots (adapted from Bear, et al., 2008); Right: Pyramidal system.

<sup>13</sup> The term “efferent” is derived from Latin meaning "which brings" (Bear, et al., 2008).

<sup>14</sup> The term “afferent” is derived from Latin meaning "which leads" (Bear, et al., 2008).



The path involving the transmission from the motor cortex to the muscles is called the corticospinal or pyramidal tract<sup>15</sup>. Transmission occurs directly in the pyramidal tract and indirectly through multiple accessory pathways involving basal ganglia, cerebellum, and several brainstem nuclei. The pyramidal tract originates from pyramidal neurons in layer V of the cerebral cortex of M1 (30%), PMA and SMA (30%) and S1 (40%). The pyramidal tract is mainly composed of motor axons, constituting the volunteer component of the motricity. The pyramidal pathways consist of a single tract, originating in the brain, which is divided into two separate tracts in the spinal cord: the lateral corticospinal tract and the anterior corticospinal tract (Figure 2.7 - Right).

From all the fibers of the pyramidal tract, 80% cross to the other side in the decussation<sup>16</sup> of pyramids in the Bulb<sup>17</sup> (contralaterally), forming the lateral corticospinal tract and 20% follow caudally to lateral funiculus of the spinal cord (ipsilaterally), forming the anterior corticospinal tract. The anterior corticospinal tract also crosses to the other side, but only at the medullar level, where it makes a synapse (Guyton & Hall, 2006). Therefore, the behavior of the pyramidal pathways leads to the conclusion that the voluntary motricity is 100% crossed, either at the bulbar level, or at the spinal cord level (Bear, et al., 2008).

## 2.4 Neuronal circuits and oscillatory activity of the thalamocortical system

As mentioned in the Introduction chapter, mental tasks related to motor imagery are the most common choice to control BCIs. In part, this is due to the easiness of performing motor imagery tasks compared to mental tasks of mathematical calculation or vocabulary association, and also due to the well documented physiological features of motor imagery like the Event Related Desynchronization/Synchronization (ERD/ERS) (Pfurtscheller & Lopes, 1999). Finally, motor imagery tasks provide an intuitive way for controlling BCIs associated to electronic prosthetic limbs.

This section will discuss the physiological aspects that cause the ERD/ERS pattern, observed during the imagination of motor tasks. Subsequently, after the

---

<sup>15</sup> Grouping of CNS axons that have common origin and destination (Bear, et al., 2008).

<sup>16</sup> Axons crossing from one side to the other (Bear, et al., 2008).

<sup>17</sup> The cross section of the medulla at the decussation level shows that the corticospinal tract forms a triangular protuberance, reason why this area is called bulbar pyramid. For the same reason the corticospinal tract is also called the pyramidal tract (Bear, et al., 2008).

presentation of the characteristics of the EEG signal, the ERD/ERS will be defined and mathematically quantified.

Neurons that connect the nervous system with different layers of the brain form neuronal circuits. The neuronal circuits transmit information through excitatory and inhibitory synapses. Excitatory synapses may be mediated by the neurotransmitter acetylcholine (ACh), dopamine (DA), noradrenaline (NA), adrenaline, serotonin, glutamate (Glu) and glycine (Gly), while the inhibitory synapses are mainly mediated by the neurotransmitter gamma-aminobutyric acid (GABA).

In some neuronal circuits, the input signal causes an excitatory synapse in one direction and one inhibitory synapse in another direction (Figure 2.8 - A). In this Figure the input fiber (sensory neuron) directly excites the neuron #1 and simultaneously excites the intermediate inhibitory neuron (neuron #2), which secretes GABA to inhibit neuron #3. This kind of circuit is important to prevent excessive activity in many parts of the brain (Guyton & Hall, 2006).

Oscillatory neuronal circuits are the most important neuronal circuits of the nervous system. Figure 2.8 - B shows a very simple circuit, consisting only of an excitatory neuron, one inhibitory neuron and an external constant afference, where an excitatory cell (cell E) and an inhibitory cell (cell I) establish a synapse with each other. As long as there is a constant excitatory conduction over the cell, which does not have to be rhythmic, the resulting activity of the set tends to be oscillating. A cycle of activity across this network generates the firing pattern shown in Figure 2.8 - C.

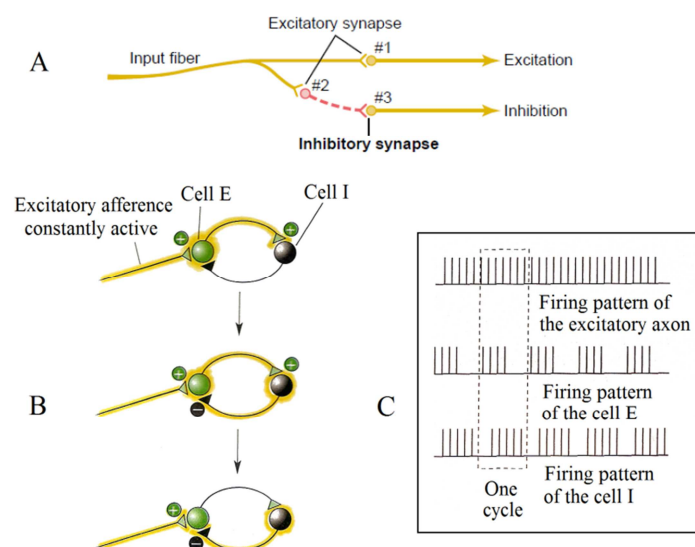


Figure 2.8 – (A) Excitatory-inhibitory neuronal circuit (Guyton & Hall, 2006); (B) Two neurons oscillator; (C) Firing pattern of the two neurons oscillator (adapted from Bear, et al., 2008).

Oscillatory neuronal circuits can also be formed by positive feedback. Consequently, once stimulated, the circuit can produce periodic stimuli for long periods. The simplest oscillatory circuit is shown in Figure 2.9 - A. This circuit only has one neuron whose part of its output extends to its own dendrites to be re-stimulated. Figure 2.9 - B shows a circuit with additional feedback neurons. Figure 2.9 - C shows a little more complex circuit with facilitator and inhibitor neurons, and Figure 2.9 - D shows an oscillatory circuit with multiple parallel neurons (Guyton & Hall, 2006).

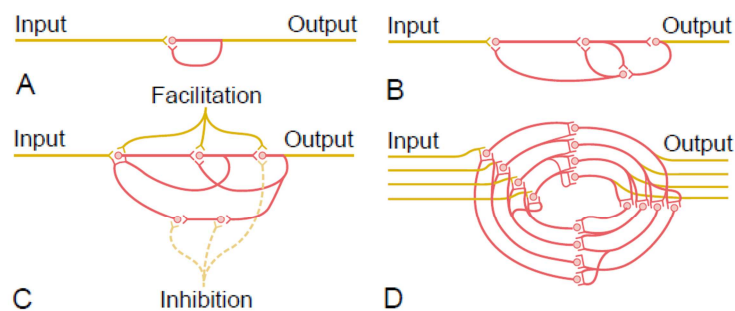


Figure 2.9 – Oscillatory neuronal circuits (Guyton & Hall, 2006).

Kevan Hashemi calculated that coherent neurons could not activate themselves at a frequency much higher than 100 Hz. The activation of a single neuron takes roughly 2 ms for its rising and falling edges, and its refractory period, in which it can not be reactivated, is about 10 ms. Thus, it will prevent any neuron from firing at a much higher frequency than 100 Hz (Hashemi, 2012). Simple neuronal circuits working with negative (Figure 2.8 - B) or positive (Figure 2.9 - A) feedback will also be subject to this same upper bound of the frequency.

The oscillatory activity can be measured in the EEG signal, being an emergent property of the thalamocortical system and the corticocortical system. In the thalamocortical system the oscillatory neuronal circuits are formed between the thalamus and the cortex and in the corticocortical system the oscillatory neuronal circuits are formed between the different layers of the cerebral cortex.

The human cortex is a laminar structure composed of six distinct layers<sup>18</sup> of alternate white and grey laminae with different kinds of neurons. Figure 2.10 shows a schematic representation of the cortical layers such as it appears in histological

<sup>18</sup> The cortex layers were discovered in 1840 by the French physician Jules Baillarger. His name is associated with the inner and outer bands of Baillarger, which are two layers of white fibers of the cerebral cortex. They are prominent in the sensory cortical areas because of high densities of thalamocortical fiber terminations.

preparations stained by different methods (Machado, 2007). Perpendicular to the layers there are large neurons called pyramidal neurons, which connect the various layers together and represent about 85% of the neurons in the cortex (Guyton & Hall, 2006). Corticocortical oscillatory circuits typically do not involve a large number of cells working in synchrony. Thus, the set does not induce high electrical amplitude activity and is hardly measurable by electrodes on the scalp, which contribute little to the EEG.

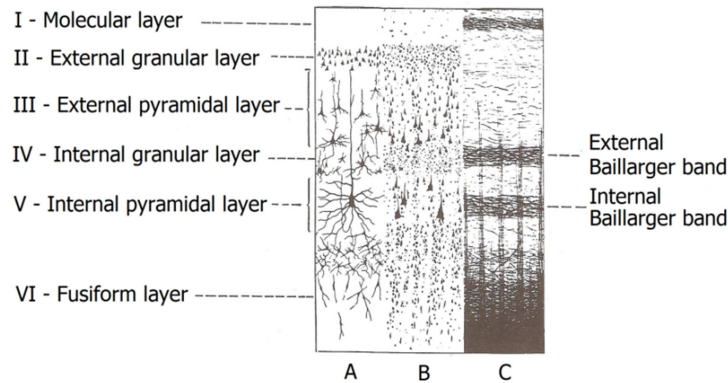


Figure 2.10 – Cortical layers. (A) Golgi method; (B) Nissl method; (C) Weigert method (adapted from Machado, 2007).

Under certain conditions, thalamic neurons can generate precise rhythmic discharges of action potentials that reach the cortex. The thalamus is located in the center of the brain, connecting its different parts, and all information reaching the cortex passes through it. Information from the sensory systems are sent to the thalamus, which redirects it to specific areas of the cerebral cortex, while information about the control of voluntary movement traverse the thalamus in the opposite direction. The thalamus is mainly composed of gray matter<sup>19</sup>, in which multiple cores are distinguished. Figure 2.11 - A shows the location of the thalamus in the brain. Figure 2.11 - B shows the main nuclei of the thalamus and Figure 2.11 - C shows the connectivity of each nucleus with the cortex. The information from M1 passes through the Ventral lateral nucleus (VL) of the thalamus where it is directed to some cranial nerves (III, IV, V, VII, IX, X, XI and XII) and to the spinal cord (Bear, et al., 2008).

To illustrate the process of information flow through the thalamus, the senses of tasting, hearing, vestibular and somatosensory will be quickly covered. The gustatory information from different regions of the tongue and oral cavity is led into the bulb by

<sup>19</sup> The gray matter consists of cell bodies of neurons while the white matter is formed by myelinated axons.

three cranial nerves (VII, IX and X) after rising to the Ventral Posteromedial nucleus (VPM) of the thalamus, and finally reaching the primary gustatory cortex (area 43) (Figure 2.11 - C). Auditory information captured by auditory receptors of the cochlea<sup>20</sup> is driven by the auditory nerve (cranial nerve VIII) to the medial geniculate nucleus of the thalamus (MG) from where it goes to the primary auditory cortex (A1) (Figures 2.3 and 2.11 - C).

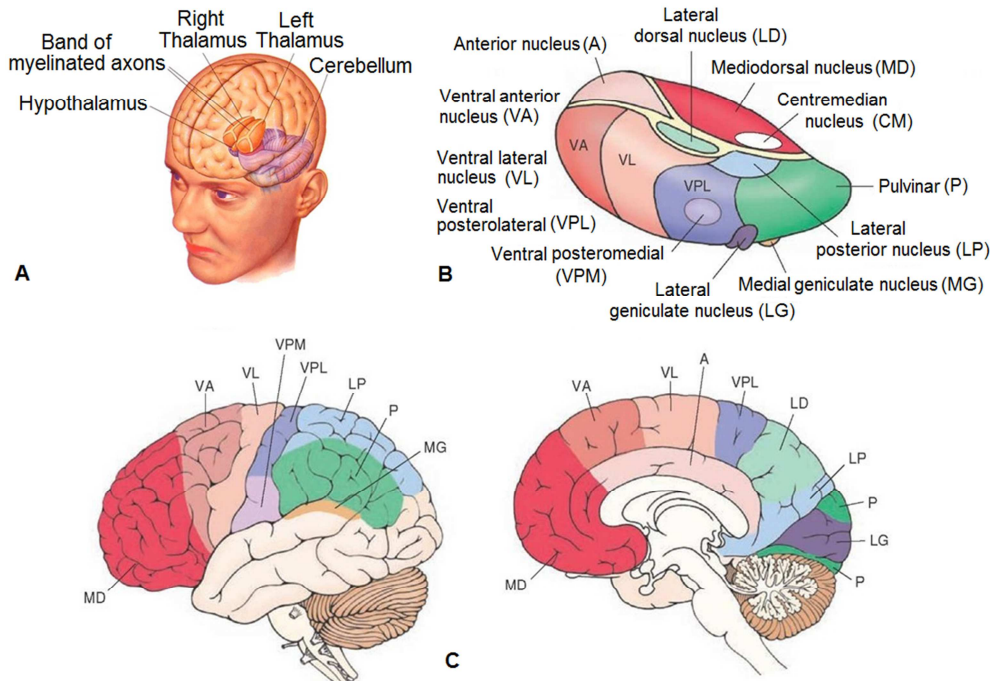


Figure 2.11 – (A) Location of the thalamus in the brain; (B) Schematic representation of the main nuclei of the thalamus; (C) connectivity of each nucleus with the cortex (adapted from what-when-how, 2013).

The vestibular system, which gives information about the position and movement of the head providing a sense of balance is driven by the auditory nerve to the Ventral Posterolateral and Posteromedial nucleus (VPL and VPM) of the thalamus, projecting axons to regions close to the representation of the face between S1 and M1. The somatic sensory system, which involves the senses of touch, temperature, pain and body position sends the information from the sensory receptors through the spinal cord, which continues to the medulla, pons and midbrain until it reaches the VPL and VPM nucleus, which projects axons to S1 (Bear, et al., 2008).

The thalamus has a particular set of neuronal cells that operate as the circuits of Figures 2.8 and 2.9, providing self-sustaining rhythmic discharge, even in the absence

<sup>20</sup> The term “cochlea” is derived from Latin meaning “snail” (Bear, et al., 2008).

of an external afference. The rhythmic activity of these circuits becomes synchronized with many other thalamic cells that are projected to the cortex by thalamocortical axons. Thus, a relatively small group of centered thalamic cells can compel a much larger group of spread out cortical cells to follow the thalamic rhythm (Bear, et al., 2008). When a neuron or a neuron mass starts to spike at a fixed delay in response to periodic input it is called phase-locking.

The large number of cortical cells working in synchrony induces a high electrical amplitude activity that can be measured by electrodes on the scalp. It, then, provides a large contribution to the EEG and is closely related to the ERD/ERS patterns observed in the EEG during the performance of mental tasks (Pfurtscheller & Lopes da Silva, 1999). Hereinafter, for a better understanding of what occurs during the mental tasks, an example of a pattern observed in the EEG due to thalamocortical rhythms during the opening and closing of the eyes will be shown.

The visual information captured in the retina is conducted through the optic nerve (cranial nerve II) and proceeds by optical tracts to the lateral geniculate nucleus of the thalamus (LG), which projects axons to layers IV and VI of V1. Thus, when the eyes are open, the nerve impulses are continually transmitted to the visual cortex. While activated, the neuronal circuits block the sending of rhythmic activity from the thalamus to V1, which undoes the synchrony. Local brain activity increases greatly because the neural masses of V1 are processing a lot of information, but the synchronization between each neuron becomes so small that the resulting induced electrical activity measured in the scalp is almost null. The results are EEG waves of small amplitude, high frequency and irregular rhythm known as  $\beta$  (14 - 30 Hz) rhythm (Guyton & Hall, 2006).

When the eyes are closed no impulses are being transmitted to the visual cortex. Then, the neural circuits allow the sending of rhythmic activity from the thalamus to V1, which become synchronized, or phase-locked, in the same frequency band as the thalamic pace. Local brain activity decreases, but the neuronal circuits of V1 are synchronized at nearby frequencies, resulting in a high-energy pace, the  $\alpha$  (8 - 13 Hz) rhythm (Guyton & Hall, 2006).

The resulting pattern indicates that when the eyes are open the EEG signal measured over V1 shows a small amplitude at the frequencies of the  $\alpha$  rhythm, since the neural masses are desynchronized. When the eyes are closed the EEG signal measures a large amplitude at the frequencies of the  $\alpha$  rhythm, since the masses are synchronized

with the thalamic pace. This same association between high information processing and low energy at the frequencies of rhythm  $\alpha$  can also be seen over M1, SMA and PMA during the imagination of motor tasks, being the physiological basis for the phenomenon known as ERD/ERS. In the next section the motor circuit will be analyzed in the same way as the visual circuit to understand how the ERD/ERS pattern occurs during motor mental tasks.

## 2.5 Direct pathway of movement

This section will analyze circuits that are involved in motor activity, linking different areas of the motor cortex. The choice of initiation of voluntary movements engage areas in frontal, prefrontal and parietal cortex, which are connected to the basal nuclei<sup>21</sup>, deep in the brain. The basal nuclei receive most of their input signals from the cerebral cortex and return almost all of their output signals to the cerebral cortex. In each hemisphere the basal nuclei are formed by the caudate nucleus, the putamen<sup>22</sup>, globus pallidus<sup>23</sup>, subthalamic nucleus and the substantia nigra<sup>24</sup>, which are located around the thalamus, occupying a large portion of the inside of both brain hemispheres (Figure 2.12 - Left). The caudate and putamen together are called the striatum, which is the target from the cortical afference to the basal nuclei (Guyton & Hall, 2006).

The basal nuclei project an afference, called VLo, to the ventral lateral nucleus of the thalamus (VL). The VLo afference is a projection of axons from the basal nuclei through the VL to the SMA, which is intimately interconnected with the M1 (Figure 2.12 - Right). Thus, there is a path on which information will cycle from the cortex to the basal nuclei and the thalamus, and it comes back to the cortex as follows (Bear, et al., 2008):

Cortex (frontal, prefrontal and parietal) → Striate → globus pallidus → VLo → Cortex (SMA)

---

<sup>21</sup> Improperly called basal ganglia, as the term “ganglia” is only used for neural cluster in the PNS (Machado, 2007). See footnote 3.

<sup>22</sup> The term “putamen” is derived from Latin “putare” meaning “to prune, to think, or to consider”.

<sup>23</sup> The term “globus pallidus” is derived from Latin meaning “pale globe”.

<sup>24</sup> The term “substantia nigra” is derived from Latin meaning “black substance” (Bear, et al., 2008).

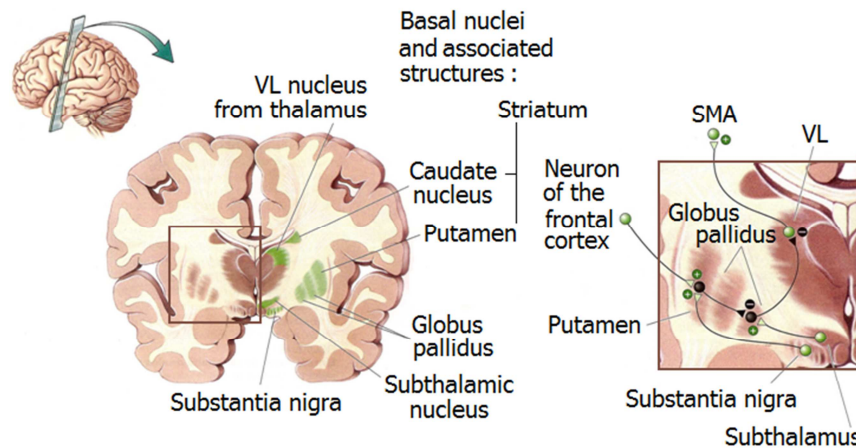


Figure 2.12 - Motor circuit. Green synapses are marked with sign (+) and are excitatory, while black synapses are marked with sign (-) and are inhibitory (adapted from Bear, et al., 2008).

This neuronal loop is known as the direct pathway of movement. The direct pathway originates with an excitatory connection to cortical cells in the putamen. The cells of the putamen establish inhibitory synapses on neurons in the globus pallidus, which in turn makes inhibitory connections with the cells of the VL. The thalamocortical connection from the VL to the SMA is excitatory, facilitating the triggering of cells related to movements in the SMA (Figure 2.12 - Right). The functional consequence of cortical activation of the putamen is the excitement of the SMA by the VL. This is because neurons in globus pallidus at rest are spontaneously active and thus inhibiting the VL.

The cortical activation (frontal, prefrontal or parietal) excites neurons of the putamen, which inhibit neurons of the globus pallidus, which in turn remove the inhibition of the VL, allowing VL neurons to become active. The activity in the VL drives the activity to the SMA. Thus, this part of the circuit acts as a positive feedback loop that can serve to focus the activation of dispersed cortical areas to the SMA. It is speculated that the signal to start the motor activity occurs when activation of the SMA is driven above some threshold for the activity that reaches it through the basal nuclei (Bear, et al., 2008).

There is a direct afference from thalamus to M1, which mainly originates from another part of the VL, which is called the VLc. The VLc retransmits the information from cerebellum. The information that comes from the cerebellum is related to motor learning and ballistic movements. The ballistic movements are movements executed so fast that the feedback can not act to control the movement. For these movements, the cerebellum relies on predictions based on experience, and it compares what was



intended with what happened, thus conducive to the learning process (Bear, et al., 2008).

The cerebellum has one tenth of the total volume of the brain, but it has a high density of neurons in the cortex, in fact more than 50% of the total number of neurons of the CNS. To clarify the importance of the cerebellum, the path that connects the cerebellum to other parts of the brain has 20 times more axons than the pyramidal tract (Bear, et al., 2008). The path that connects the cerebellum to M1 forms another important motor circuit. However, as the movements controlled by the cerebellum are not related to motor imagination, only the direct pathway of movement will be analyzed.

In brief, during the performance of a mental task of motor imagination, the initial cognitive activity that manifests the intention of performing the task originates in the frontal cortex. This activity propagates to the putamen through excitatory connections. The activation of the putamen inhibits the globus pallidus, which is spontaneously active. Then, the inactivation of the globus pallidus stops it from inhibiting the VLo. The VLo stays active and it can retransmit the signals to specific areas of the SMA. The neural masses of the SMA will be working with different aspects of a complex cognitive task. The neurons will be firing quickly, but not simultaneously, which results in a low synchrony. Conversely, when no motor mental task is being performed, there will be no transmission of information from the frontal, prefrontal or parietal cortices to the putamen. When the putamen is inactive it does not inhibit the globus pallidus which inhibits VLo. The inactivity of the VLo allows the SMA to receive signals from the thalamic pacemaker neuronal circuits. The SMA is connected to the M1 through the afferences that extend into layer V of M1. Therefore, the influence of the thalamic pacemaker signal can be observed in pyramidal neurons of layer V of M1, which will present a synchronous behavior (Bear, et al., 2008).

The large number of pyramidal neurons in layer V of the SMA, PMA and M1 working in synchrony induces a high electrical amplitude activity that can be measured by electrodes on the scalp. Then, when no motor mental task is being performed, the EEG signal measured over the SMA, PMA and M1 will show a high amplitude at the frequencies that are in synchrony. This frequency interval, about 8 to 13 Hz, was measured empirically and is known as  $\mu$  rhythm (Pfurtscheller & Lopes, 1999). During the performance of a mental task of motor imagination, the neural masses of the SMA, the PMA and the M1 will be desynchronized and it will induce a low electrical

amplitude activity over this area. Then, the EEG will measure a low amplitude for the  $\mu$  rhythm.

The  $\mu$  rhythm lies almost on the same frequency interval as the aforementioned  $\alpha$  rhythm. The distinction between them is mostly the location at which they are measured. The  $\mu$  rhythm is observed over the sensorimotor cortex and the  $\alpha$  rhythm is observed almost over the entire scalp. Despite the different nomenclatures for this frequency interval, both of them occur due to the projection of the thalamic pace over the cortex.

Finally, this section discussed the physiologic basis behind a clear pattern that occurs during motor mental tasks and can be measured by the EEG. The  $\mu$  rhythm presents a low amplitude relative to the rest period, during the motor mental task. No specific mental task is performed during the rest period.

## Chapter 3 : The EEG signal

The purpose of this chapter is to describe the genesis of the EEG signal, the acquisition process and the EEG main rhythms and artifacts. The end of this chapter deals with the EEG SNR, the movement-related potentials and the ERD/ERS pattern.

### 3.1 Electroencephalographic signal

The electroencephalogram is the recording of the electrical activity of a large population of neurons of the cerebral cortex measured on the surface of the scalp using electrodes. The noninvasive method is the most usual. However, neuronal activity can also be obtained by introducing the electrode within the brain tissue (depth recording) or by placing electrodes on the exposed surface of the brain, which is called electrocorticogram (ECoG) (Geisinger, 2005).

The EEG recording is relatively simple: about two dozen electrodes are fixed in standard positions on the scalp and connected to amplifier channels of record systems. Small voltage fluctuations, usually a few tens of microvolts ( $\mu\text{V}$ ) are measured between selected pairs of electrodes and then amplified, usually, between 5 to 30 thousand times (Davidson, et al., 2000). A typical EEG recording (Figure 3.1) is a set of many irregular simultaneous tracings, indicating changes in voltage between pairs of properly grounded electrodes. Each output signal of the amplifier controls a record pen or is stored in a computer memory (Bear, et al., 2008).

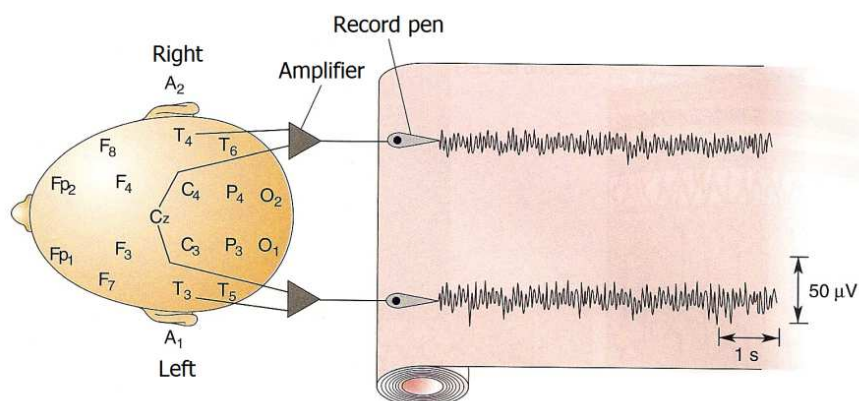


Figure 3.1 - Typical EEG record (adaptaded from Bear, et al., 2008).

The EEG mainly records the extracellular currents that arise as a consequence of synaptic activity in dendrites of neurons in the cerebral cortex. The extracellular electric field is mainly generated by the Post-Synaptic Potential (PSP) that may be excitatory (EPSP) or inhibitory (IPSP). When the action potential (100mV) reaches post-synaptic dendrites, it causes a current flowing, that enters through the synapse to the post-synaptic dendrites of the next neuron. This current is called extracellular activation current, being of around 3 nA and it causes the rising potential within the post-synaptic membrane, that is the EPSP. The current enters the post-synaptic dendrites toward the soma<sup>25</sup>. It goes out into the extracellular fluid by the membrane capacitance of the cell, and then returns to the dendrites making a circular path. This circular current is called excitatory postsynaptic current (Hashemi, 2012) (Figure 3.2).

The neuron has a rest potential, about 65mV, but it does not produce an external electrical field. The cell membrane is formed by a 5 nm phospholipid bilayer closely-approximated by the infinite parallel plate capacitor with capacitance around 0.01 F/m<sup>2</sup> between the intracellular and extracellular fluid. Thus the electric field outside the capacitor is zero and the rest potential has no influence on the EEG signal. In the same way, during the activation for the propagation of an action potential the interior of the cell jumps up by 100 mV, but it does not induce an electrical field outside the cell membrane (Hashemi, 2012).

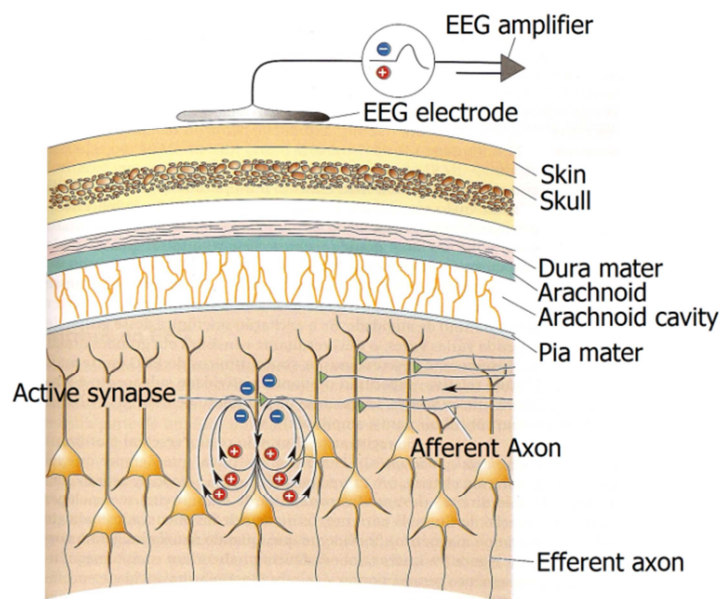


Figure 3.2 – Electric field generated by extracellular currents in pyramidal cells (Bear, et al., 2008).

<sup>25</sup> The word “soma” comes from the Greek meaning “body”. The soma of a neuron is often called the cell body.

As mentioned in section 2.4, the neurons of the cortex are divided into six layers parallel to the surface. These neurons belong to two kinds: pyramidal (layers III, V) and non-pyramidal (layers I, II, IV and VI). Glial cells have spherical symmetry, not having a common direction for the propagation of the electrical signal. As consequence of this symmetry the resulting electromagnetic field is null (Lopes, 2005). The postsynaptic potential of neurons generates extracellular electric fields that have a bipolar distribution, then, neurons can be modeled like a small dipole. The orientation of the dipole depends on the type of PSP that is occurring in the neuron (Luck, 2005).

For example, EPSP occurs in synapses mediated by the neurotransmitter glutamate. Glutamate activates the opening of cation channels, allowing the flow of  $\text{Na}^+$  ions into the postsynaptic dendrite. The flow of  $\text{Na}^+$  makes the soma positive in relation to extracellular fluid (Figure 2.15 - A). IPSP occurs in GABA-mediated synapses allowing the flow of  $\text{Cl}^-$  ions into the postsynaptic dendrites. The flow of  $\text{Cl}^-$  makes the soma negative in relation to extracellular fluid (Bear, et al., 2008). Therefore the orientation of dipoles of excitatory and inhibitory neurons is opposite (Luck, 2005).

The dipole of an individual neuron is impossible to measure by electrodes on the scalp, but under specific conditions, the dipoles of many neurons are added together, generating a resulting field that can be measured on the scalp. The dipoles need to be spatially aligned and the PSP should occur at approximately the same time, so that the dipole activity adds up. If the neurons are randomly oriented the positivity of a dipole would be canceled by the negativity of the adjacent dipole. Furthermore, if a neuron is stimulated by an excitatory neurotransmitter and an adjacent neuron is stimulated by an inhibitory neurotransmitter, the dipoles will have opposite orientations and will cancel each other. However, if many neurons having similar orientations and the same type of neurotransmitter are stimulated at approximately the same moment, then, the dipoles will be added together and their activity may be measured on the scalp (Luck, 2005).

Non-pyramidal cells are mostly inhibitory, mediated by the neurotransmitter GABA, with the exception of interneurons that can be excitatory or inhibitory. These cells have bipolar distribution and in majority use a common neurotransmitter, however, their random orientation cancels the electromagnetic field resulting from the dipoles.

Pyramidal cells are excitatory and use a common neurotransmitter glutamate. They have a resultant electric field with bipolar configuration (Figure 3.3 - A) and are spatially aligned perpendicularly in the cortex (Figure 2.10). Thus, they are the main contributors to the formation of the electrical signals recorded as the EEG. Most

pyramidal cells have their axons directed to the thalamus and basal nuclei, so that the soma which is relatively positive is below the postsynaptic dendrites that are relatively negative and closer to the surface of the cortex. Figure 3.3 - B shows the bipolar configuration of the electric field of pyramidal neurons in an active cortical region, in which the outer surface is negative and the inner region is positive. Figure 3.3 - C shows the equivalent dipole resulting from this region (Luck, 2005).

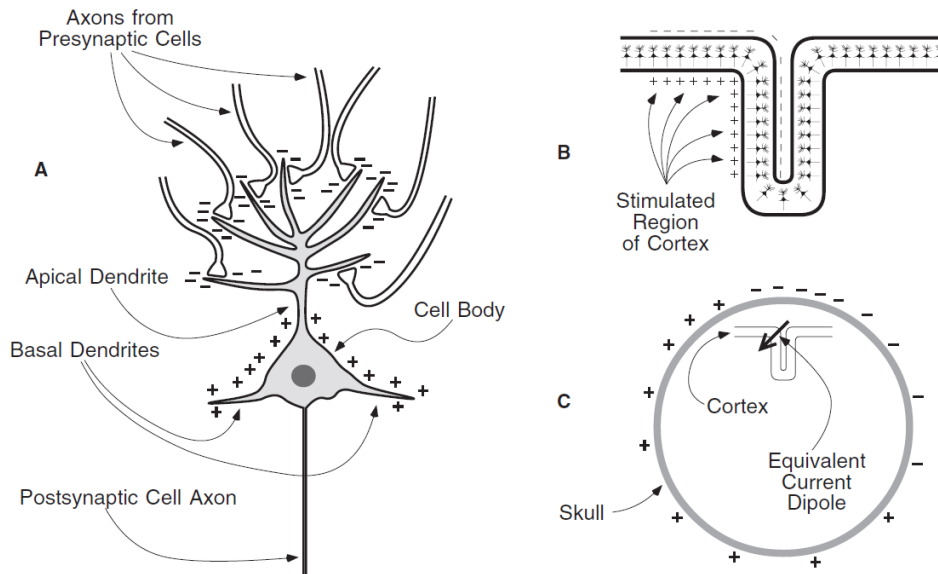


Figure 3.3 – (A) Bipolar configuration of the electric field of a pyramidal neuron during a PSP; (B) Bipolar configuration of the electric field of a pyramidal neurons of an active cortical region; (C) Equivalent current dipole of the active cortical region (Luck, 2005).

Extracellular electric fields generated by neurons are attenuated and scattered when crossing the skull toward the scalp due to the low conductivity of the skull that acts as a low pass spatial filter (Davidson, et al., 2000). The skull thickness can vary from 3.3 to 6 mm depending on its location, which causes a variation of electrical resistance (Tang, et al., 2008). Therefore, the scalp distribution of the electric field is mainly distorted by variations in the conductivity of the skull, but it is also affected by the conductivity of the meninges<sup>26</sup> and the skin (Figure 3.2).

The EEG electrode is made of a very conductive material in order to measure the electrical potential difference induced by the residual electric field of the scalp, relative to a reference point. However, only with the contribution of small voltages of thousands

<sup>26</sup> Meninges is the plural of meninx, from Greek “membrane”. The meninges are the system of membranes that envelope and protect the CNS (spinal cord, brainstem and brain) and it consists of three layers: the dura mater, the arachnoid mater, and the pia mater.

of cells firing together can this signal be sufficiently intense to be detected on the surface of the scalp. This population of neurons is called the neural mass and consists of  $10^4$  to  $10^7$  neurons (Azevedo, 2005). The joint activation of neurons in a neural mass is called synchronism. If the synchronous excitation of this group of cells is repeated several times the EEG will consist of large rhythmic waves (Bear, et al., 2008).

Figure 3.4 shows the generation of large EEG signals by neural synchronous activity. Figure 3.4 - A shows six pyramidal neurons wherein the PSP is measured between a pair of sensors at their extremities (green triangles). In Figure 3.4 - B the neurons are activated in irregular time intervals and the summed PSP activity of all six neurons has small amplitude. In Figure 3.4 - C the neurons are activated synchronously, and the summed PSP activity of all six neurons has higher amplitude (Bear, et al., 2008).

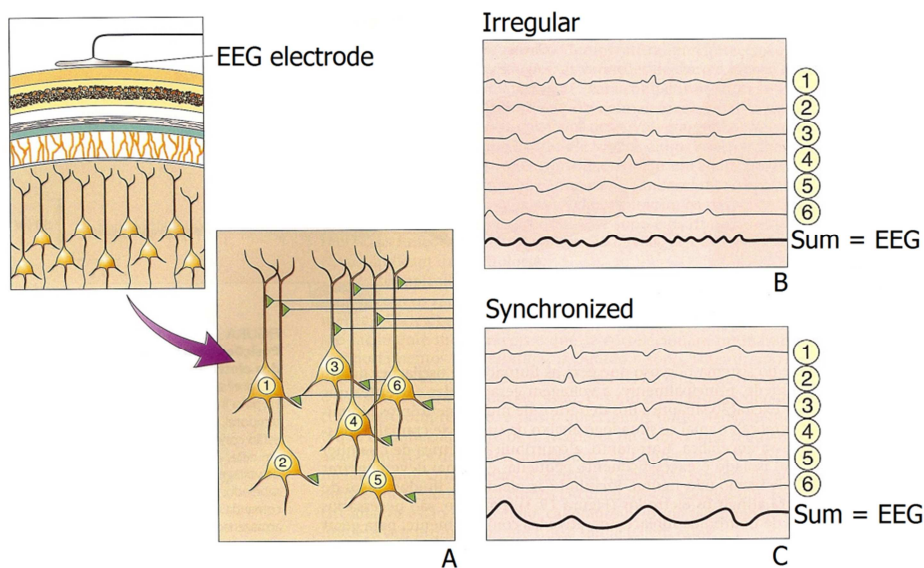


Figure 3.4 – (A) Pyramidal neurons beneath EEG electrode; (B) Unsynchronized neuronal activity; (C) Synchronized neuronal activity (adapted from Bear, et al., 2008).

The silver electrodes wrapped in silver chloride (Ag/AgCl) were used until the 1980s, since silver is the best electricity conductor among the metals, with resistivity ( $\rho$ ) of  $1.59 \times 10^{-8} \Omega\text{m}$ . Recently, electrode caps, e. g., caps from the companies Electro-Cap<sup>®</sup> and MedCap<sup>®</sup>, use tin electrodes ( $\rho = 1,09 \times 10^{-7} \Omega\text{m}$ ), a good conductor and also inert to oxygen, thus, resistant to corrosion (Luck, 2005). For a comparison, the white matter resistivity is about  $6.5 \Omega\text{m}$ , the cortex (gray matter) resistivity is about  $3.0 \Omega\text{m}$ , the cerebro-spinal fluid resistivity is about  $0.64 \Omega\text{m}$  and the skull resistivity is about  $120$

$\Omega\text{m}$  (Hashemi, 2012). Figure 3.5 shows the concentric spherical head model proposed by Rush & Driscoll (1965) in which the brain, including white matter, gray matter and meninges have a resistivity of  $2.22 \Omega\text{m}$ , the skull has a resistivity of  $177 \Omega\text{m}$  and the scalp has a resistivity of  $2.22 \Omega\text{m}$  (Malmivuo & Plonsey, 1995).

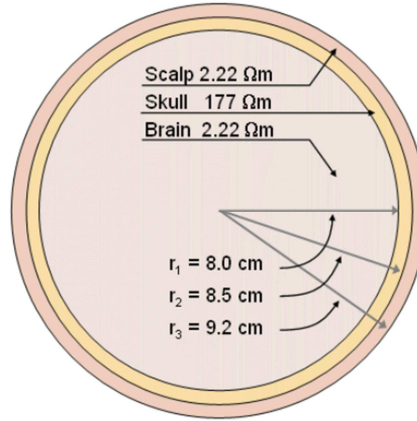


Figure 3.5 – Concentric spherical head model proposed by Rush & Driscoll (Malmivuo & Plonsey, 1995).

The internal impedance comprises the impedance of the white matter, gray matter, cerebro-spinal fluid, meninges and skull while the external impedance comprises the contact impedance and the impedance of electrodes, wires and the amplifier system. The model of the external impedance only considers resistance, because the effect of the brain's electrical permittivity and permeability is negligible at EEG frequencies, therefore, a capacitor and an inductor are not included in the equivalent circuit.

The electrodes are fixed to the scalp using a gel or a conductive electrolytic paste. This paste is intended to reduce the contact impedance between the electrode and the skin. Usually the value of this resistance must be lower than  $5 \text{ k}\Omega$  (Luck, 2005, Ford, et al., 2004). As the amplifiers of the EEG acquisition circuit have very high impedances, typically in the range of  $100 \text{ k}\Omega$ , variations in impedance of the electrodes in the order of a few thousand ohms have negligible effect on the measured voltage (Davidson, et al., 2000).

By adopting the maximum value for the contact resistance lower than  $5 \text{ k}\Omega$ , the contact resistivity of a common disk tin electrode with  $1 \text{ cm}$  of diameter and roughly  $0.5 \text{ cm}$  of length can be calculated by:

$$R = \rho \left( \frac{l}{A} \right) \leftrightarrow 5000\Omega = \rho \left( \frac{0.005 \text{ m}}{\pi(0.005\text{m})^2} \right) \leftrightarrow \rho = 78.5398\Omega\text{m} . \quad (3.1)$$



where  $l$  is the length of the electrode and  $A$  is area of the electrode. Then, the contact resistivity is lower than the skull resistivity given by Kevan Hashemi (120  $\Omega\text{m}$ ) what assures a current flow into the electrode.

### 3.2 EEG acquisition

Regarding the naming and placement of the electrodes on the scalp, in 1958 Herbert Jasper suggested a system which is now used worldwide; it is called “International 10-20 System” (Böcker, et al., 1994). In Figure 3.6 - A electrodes on the edges of the scalp are located at 10% of the distance covered along the curved horizontal line connecting the nasion to the inion through the preauricular point, in which this percentage is related to the length of the line connecting the nasion to the inion through the vertex. All electrodes are positioned with 20% of distance between each other. Then the “10” and “20” numbers of the “International 10-20 System” refers to these percentage values. The electrodes are named by a capital letter corresponding to the initial of the brain lobe where they are placed (F = Frontal, C = Central, P = Parietal, O = Occipital and T = Temporal), followed by an even number for the right hemisphere and an odd number for the left hemisphere. The letter “A” is used for electrodes placed in the ear (from “auricular”). For the electrodes placed in the frontal lobe, near the nasion, the letter “p” is added (Fp = Frontal pole). For the electrodes in the line connecting the nasion to the inion, the letter “z” related to “zero” is used rather than a number, indicating the central division of the brain hemispheres (Figure 3.6 - B) (Luck, 2005). Figure 3.6 – C shows the International 10-10 System and it is worth noting that the T3, T4, T5 and T6 electrodes of the 10-20 system have different names (T7, T8, P7 and P8, respectively) in the 10-10 system.

If the electrical potential of the scalp was measured with only one EEG electrode relative to the ground of the acquisition circuit, the circuit would measure only the static electricity difference between the scalp and the circuit, which is much larger than the neural activity. For comparison, the neural activity generates voltage changes in the order of tens of microvolts while the average static electricity of a human body is around 4 to 35 thousand volts<sup>27</sup>.

---

<sup>27</sup> The average electrical resistance of a human body is between 1.3 to 3 k $\Omega$  and the average capacitance is around a few hundred of picofarads. Further, the capacitance model of the human body, as defined by the Electrostatic Discharge Association (ESDA), is a 100 pF capacitor in series with a resistor of 1.5 k $\Omega$

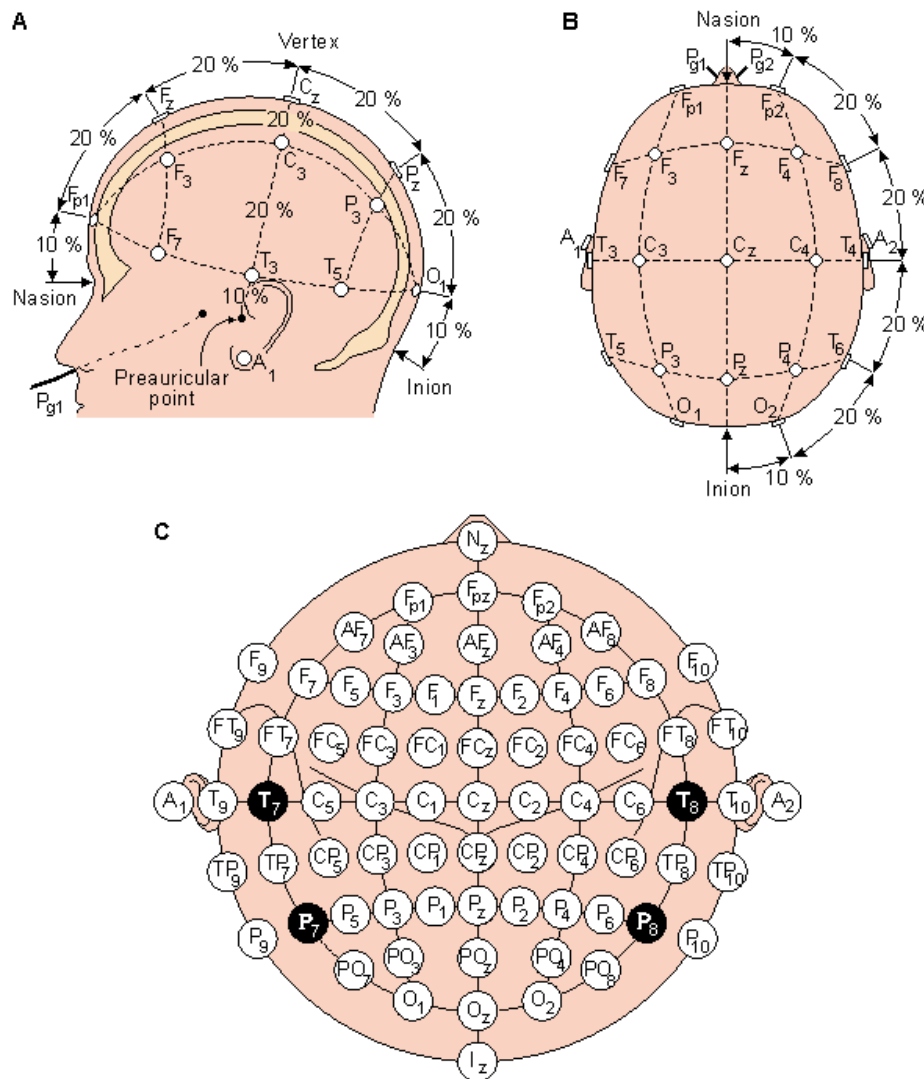


Figure 3.6 – A) and B) International 10-20 System; C) International 10-10 System (Malmivuo & Plonsey, 1995).

However, even using the voltage difference between two electrodes in the scalp to create an EEG channel (C), any noise that affects the ground or the power of the acquisition circuit also would mask the neural activity. To solve this problem the EEG amplifier system uses differential amplifiers with three electrodes in order to create a channel: an electrode called “active<sup>28</sup>” electrode (A), one reference electrode (R), and a

---

charged with voltages from 4 to 35 kV. In this model a capacitor with initial voltage of 35 kV provides an electrical current below 5 mA after 1.3  $\mu$ s. Thus, the high voltage acquired by static electricity from the human body provides currents above the threshold of human perception, which is around 5 mA, during instants of time lower than 1.3  $\mu$ s and no electrical discharge is noticed.

<sup>28</sup> This electrode is called “active” to distinguish itself from the ground and reference electrodes, and it measures passively the scalp potential. It should not be confused with active electrodes that actually perform the signal amplification.

ground electrode (G). The differential amplifier amplifies the voltage difference between  $V_{AG}$  and  $V_{RG}$  ( $C = V_{AG} - V_{RG}$ ), and the common noise that affects the ground of both measures is eliminated (Luck, 2005).

The ground electrode is usually positioned on the frontal bone to minimize the noise of muscular origin. Its potential is canceled during differential amplification. Therefore, its location is not as important as the location of the reference electrode. There is no ideal “neutral” place to position the reference electrode, so it should be kept in mind that the EEG signal from one channel always reflects the contribution of both active and reference electrodes. The reference electrode is usually attached to one ear lobe or to both.

Figure 3.7 shows the ground electrode (G), the reference electrode (R) and the active electrode (A) on the scalp area of interest to measure the EEG. The ground electrode is positioned in the frontal region; the reference electrode is positioned on the left ear; and electrode (A) is positioned over the occipital lobe of the left hemisphere in order to create the channel O1. This figure also shows the resulting dipole of an active area of the cortex and its potential distribution over the scalp. In this example  $V_{AG}$  is lower than  $V_{RG}$  and, therefore, the calculated potential for O1 will be negative.

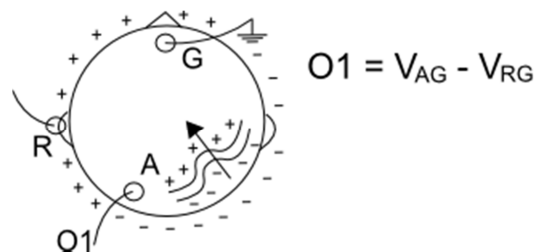


Figure 3.7 –Grounding electrode (G), the reference electrode (R) and the active electrode (A) in order to compose the occipital channel O1.

The EEG signal is represented by a number sequence ordered with respect to its temporal evolution. The potential  $V_{AG}(t)$  and  $V_{RG}(t)$ , and the channel  $O1(t)$ , are shown in the text without reference to its time instant just for simplicity. Thus, in this Thesis, all operations involving variables without the time reference are considered non-recursive, being applied only to the same instant of time.

For the EEG acquisition with multiple locations there are three distinct ways of electrode derivations in order to create the channels: bipolar method, unipolar method (or common electrode/reference) and Common Average Reference method (CAR).

Figure 3.8 - A illustrates the bipolar method in which each channel (T3, C3, C4 and T4) is the difference of potential between two neighboring electrodes (A1, A2, A3, A4 or A5). It may be noted that in this method there is no fixed reference electrode and the number of channels is always smaller than the number of electrodes. It must be remembered that the grounding electrode is present for all three kinds of derivations.

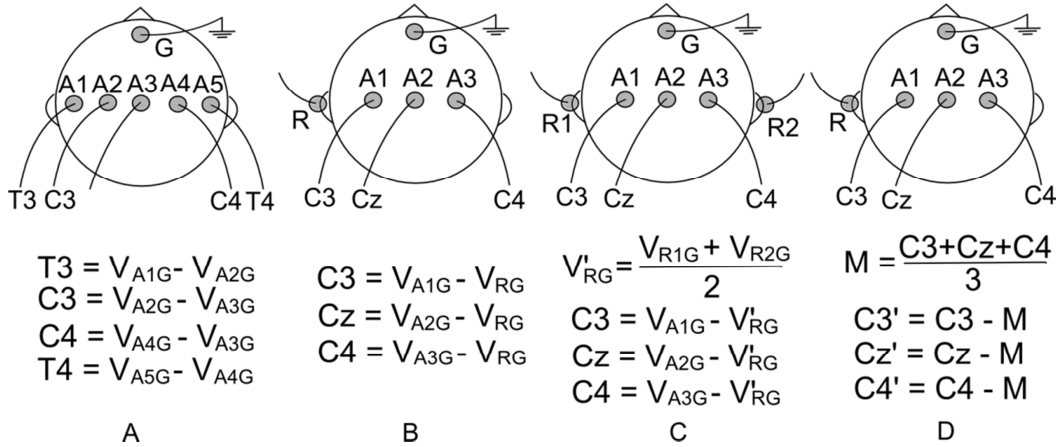


Figure 3.8 – (A) Bipolar method; (B) Unipolar method (uniauricular reference); (C) Unipolar method (biauricular reference); (D) CAR method using the uniauricular reference.

Figure 3.8 - B shows the unipolar method, which has a reference electrode (R) common to all channels. The measured voltage is the difference between any electrode and the reference. Figure 3.8 - C shows the unipolar method with biauricular reference electrodes (R1 and R2), in which the measured voltage is the difference between any electrode and the average values of the reference electrodes.

In the CAR method the signal is originally acquired by the unipolar method (Figure 3.8 - B, channels C3, Cz e C4) and then channels C3', Cz' e C4' are formed by subtracting the average reference potential (M) from the unipolar potentials (Figure 3.8 - D). In general, considering  $n$  channels,

$$C'_i = C_i - \frac{1}{n} \cdot \sum_{i=1}^n C_i . \quad (3.2)$$

where  $C_i$  is the  $i$ -th channel, and  $C'_i$  represents the  $i$ -th channel using the common average reference. As the common average prioritizes signals that are present in a large number of channels, the subtraction leads to the elimination of these signals, working as

a high-pass spatial filter, i.e., it emphasizes components with highly localized distributions while eliminating components that are common to most channels, such as the biological external noise (Estébanez, 2003; Azevedo, 2005).

Thus, a time-varying external noise, which equally affects all electrodes, is theoretically eliminated by the CAR method. Suppose that there is a noise  $X$  that affects the grounding potential of the acquisition system,  $V_{XG}$ , and a biological noise component  $B$  from the human body that equally affects the potential of all electrodes over the scalp,  $V_{BG}$ , then the potential of the electrodes (A) and reference (R) will be,

$$\begin{cases} V_{AG} = \hat{V}_{AG} + V_{BG} + V_{XG} \\ V_{RG} = \hat{V}_{RG} + V_{BG} + V_{XG} \end{cases}, \quad (3.3)$$

where  $\hat{V}$  represents the potential measured by the electrode in the absence of noise. Thus, the channel  $C'$  calculated with the CAR method will be given by,

$$\begin{aligned} C'_i &= C_i - \frac{1}{n} \cdot \sum_{i=1}^n C_i = V_{AG} - V_{RG} - \frac{1}{n} \cdot \sum_{i=1}^n V_{iG} - V_{RG} = V_{AG} - \frac{1}{n} \cdot \sum_{i=1}^n V_{iG} \leftrightarrow \\ C' &= \hat{V}_{AG} + V_{BG} + V_{XG} - \frac{1}{n} \cdot \sum_{i=1}^n \hat{V}_{iG} + V_{BG} + V_{XG} \leftrightarrow \\ C' &= \hat{V}_{AG} - \frac{1}{n} \cdot \sum_{i=1}^n \hat{V}_{iG} \rightarrow C' \approx \hat{V}_{AG}. \end{aligned} \quad (3.4)$$

In equation (3.4) the channel  $C'$  will be free of noise  $X$  affecting the grounding electrode and also the biological noise  $B$  that ideally equally affects all electrodes. Finally, assuming that the activity of the different brain areas is uncorrelated and can be considered random, it then follows that, as the number of electrodes increases, the averaged reference (M) approaches zero. Thus, the sum  $1/n \cdot \sum_{i=1}^n \hat{V}_{iG}$  can be discarded and the potential measured in channel  $C'$  increasingly becomes independent of the fluctuations of the reference.

Figure 3.9 shows the decrease of the average reference (M) amplitude as the number of channels increases. It can be seen that M tends to be a constant different than zero. This is because the ideal assumptions that the activity of the measured brain areas is uncorrelated and fully random and the biological external noise equally affects all

electrodes are not completely valid. This figure was obtained with the EEG of 60 repetitions of the motor mental task of imagination of movement of the right hand. Details of the mental task experiments are mentioned in chapter 5, section 5.1. This figure shows that the reference amplitude decreases from  $26.3 \pm 3.4 \mu\text{V}$  to  $16.5 \pm 2.8 \mu\text{V}$  by using 19 channels. The error bars are the standard deviation calculated from the 60 experiment repetitions.

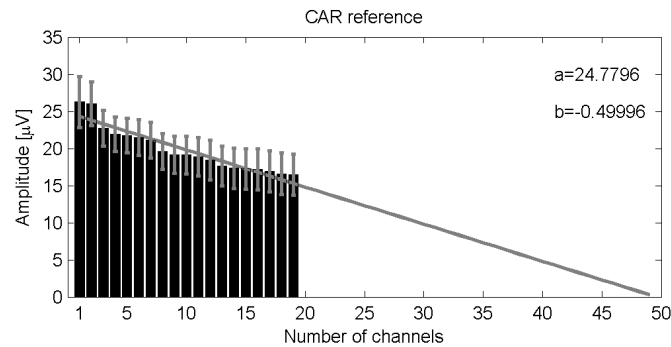


Figure 3.9 – Decrease of the average reference amplitude as the number of channels increases.

A linear regression was performed (Figure 3.9), in which the intercept (a) and the slope (b) are 24.8 and -0.5, respectively. The linear regression gives estimation in which for each added channel the reference amplitude should decrease  $0.5 \mu\text{V}$ . Although those ideal assumptions can not be assured, with 50 roughly independent channels, the reference amplitude potential should be near to zero or at least smaller than the actual potential.

### 3.3 Main EEG rhythms

The EEG signal has specific features in defined frequency bands. It is known that the performance of some activities, such as sleep, relaxation or mental effort is related to specific frequency bands, which can even be induced, blocked or changed during a mental task (Pfurtscheller & Lopes, 1999). The main frequency bands are denoted by Greek letters:  $\alpha$ ,  $\beta$ ,  $\gamma$ ,  $\delta$ ,  $\mu$  and  $\theta$ . Each band is generally observed at a specific location and circumstance, such as:  $\delta$  rhythm is observed in the frontal lobe during deep sleep;  $\alpha$  rhythm is observed in the occipital lobe when the eyes are closed, and  $\mu$  rhythm is observed in the motor cortex during the performance of a motor

activity. The normal oscillatory activity (Figure 3.10) is classified into infra-slow (0.02-0.1 Hz), slow (0.1-15 Hz), fast (20-60 Hz) and ultrafast (100-600 Hz).

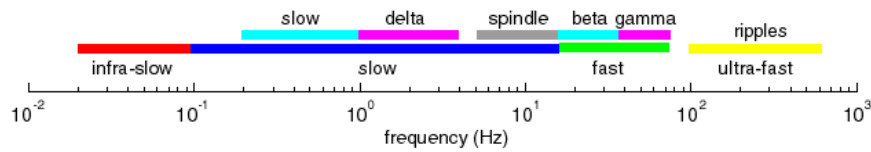


Figure 3.10 – Coverage of the EEG frequency spectrum (Thalamocortical oscillations, 2013).

The most important EEG features are comprehended in frequencies that extend to 30Hz. This frequency range is subdivided into groups or rhythms ( $\delta$ ,  $\theta$ ,  $\alpha$ ,  $\mu$  and  $\beta$ ) related to the location of measurement and the band of frequencies, as shown in Table 3.1.

Table 3.1 - Frequencies occurring in the human brain (Cheeín, 2005).

Banda	Frequency (Hz)	Amplitude ( $\mu\text{V}$ )	Localization
Delta ( $\delta$ )	1 - 4	< 100	Variable
Theta ( $\theta$ )	4 - 8	< 100	Variable
Alpha ( $\alpha$ )	8 - 13	20 - 60	Occipital
Beta ( $\beta$ )	14 - 30	20 - 30	Frontal and Parietal
Mu ( $\mu$ )	8 - 13	< 50	Motor cortex
Gamma( $\gamma$ )	25-100	< 50	Variable

Regarding the ultrafast activity (100-600 Hz), Kevan Hashemi (2012) reported that the highest frequency fluctuation observed in the EEG is up to 120 Hz. He showed that the High-Frequency Oscillations (HFO) and Very High-Frequency Oscillations (VHFO) reported to exist in animal and human EEG by many recent papers (e.g. see Gonzales, et al., 2006) may be artifacts of band-pass filtering or a mismeasurement, i. e., an artifact by electromyographic activity related to other neural functions, such as minute eye movements<sup>29</sup>.

The activation period of a single neuron is about 2 ms, thus, the activation frequency of a neuron can not be greater than 500 Hz. The refractory period of a single neuron is of order 10 ms, which will prevent any neuron from firing much faster than

<sup>29</sup> Minute eye movements, also known as saccade, are fast eye movements of a few minutes of arc, in which there is no conscious control of the speed.

100 Hz. Because EEG is generated by large numbers of neurons acting coherently, it is impossible for EEG to include a fundamental oscillation frequency much higher than 100 Hz. Finally, Kevan Hashemi asserts that he can see no mechanism by which such an oscillation could take place, neither in a group of neurons acting coherently, nor in a single neuron acting alone.

Because of this, the HFO and VHFO of the EEG will be not investigated in this Thesis and for all posterior analysis (described in chapter 3) a sampling rate of 200 Hz will be used, that ensures the observation of the main frequency bands ( $\alpha$ ,  $\beta$ ,  $\gamma$ ,  $\delta$ ,  $\mu$  and  $\theta$ ). In what follows, the mental states associated with some frequency bands are described.

- $\delta$  Rhythm: frequency band between 1 and 4 Hz. It is registered in individuals in deep sleep, and also may appear related with some pathological states.
- $\theta$  Rhythm: frequency band between 4 and 8 Hz. The signal has higher amplitude, in relation to  $\alpha$  and  $\beta$  rhythms. It is found on the frontal region during mental activities such as problem solving and in the temporal and parietal regions during emotions of stress, disappointment and frustration.
- $\alpha$  Rhythm: the International Federation of Electroencephalography and Clinical Neurophysiology defines the  $\alpha$  rhythm as the frequency band between 8 and 13 Hz occurring in awake people over posterior regions of the brain, with typically higher voltage over the occipital areas. The amplitude is variable but it is almost always below 50  $\mu$ V in adults. It is more easily detected with eyes closed and subject conditions of physical relaxation and mental inactivity. It is blocked or attenuated by attention, especially visual, and by mental effort (Guyton & Hall, 2006). Also, the mental imagination of sound generally elicits an increase of  $\alpha$  band activity (Schaefer et al., 2011a).
- $\mu$  Rhythm: frequency band between 8 and 13 Hz. It is a rhythm associated with motor activities and best acquired in the motor cortex. It is blocked or attenuated with movement or the intention to move. As previously mentioned in section 2.5, despite its frequency range and amplitude being similar to the  $\alpha$  rhythm, the  $\mu$  rhythm is topographically and physiologically different from the  $\alpha$  rhythm (Estébanez, 2003; Azevedo, 2005).
- $\beta$  Rhythm: frequency band between 14 and 30 Hz, with lower amplitude, and usually caused by the opening of the eyes, being in a state of wakefulness or



REM sleep (Rapid Eye Movement). It is blocked by motor activity and tactile stimulation (Guyton & Hall, 2006).

- $\gamma$  Rhythm: frequency band between 25 and 100 Hz. The low  $\gamma$  band (25 to 40 Hz) has been shown to be present during the perception of sensory events and the process of recognition. In this Thesis, this rhythm will be especially studied because the information about the mental task of music imagery is not consolidated yet. It is known that the mental task of music imagery only faintly activates the tertiary auditory cortex (A3) and it also could include high-frequency activity.

Figure 3.11 shows the brain rhythms described above and the attenuation of  $\alpha$  rhythm measured on the occipital lobe while the eyes were open. The replacement of the  $\alpha$  rhythm for an asynchronous  $\beta$  rhythm of small amplitude when the eyes are open was exposed in section 2.4 and it shows the EEG desynchronization.

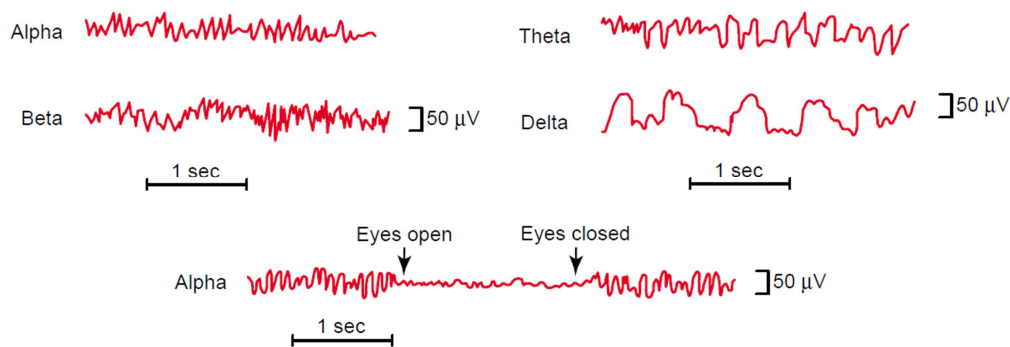


Figure 3.11 – Brain rhythms  $\alpha$ ,  $\beta$ ,  $\theta$  and  $\delta$ . The EEG signal at the bottom shows the occipital desynchronization measured when the eyes are open (adapted from Guyton & Hall, 2006).

In general, the rhythms of low amplitude and high frequency are associated with wakefulness and alertness or the stage of sleep in which dreams occur. Rhythms of high amplitude and low frequency are associated with stages of dreamless sleep and the pathological state of coma. This is logical, because when the cortex is more actively involved in the processing of information, may these be brought by sensory afferents, or generated by internal processes, the level of activity of cortical neurons is relatively high, but also desynchronized. Each neuron or a very small group of neurons is heavily involved in a slightly different aspect of a complex cognitive task, firing rapidly, but not simultaneously in relation of its neighboring neurons. This leads to a low synchrony and thus, the amplitude of the EEG is low and  $\beta$  rhythm prevails (Bear, et al., 2008).

In contrast, during deep sleep, cortical neurons are not busy with the processing of information, and most of them are excited in phase by a slow and rhythmic afference. This rhythmic signal or pacemaker originates in the oscillatory neuronal circuits of thalamus, which imposes itself on the neurons of the cortex. Thus, the synchrony is high, and therefore the amplitude of the EEG is also high (Bear, et al., 2008).

### 3.4 Artifacts

The EEG signal is easily corrupted by other electrical signals, due to its small amplitude. The noises found in biological signals such as the EEG are called artifacts that belong to two categories related to its source: technical artifacts and physiological artifacts (Azevedo, 2005). Technical artifacts occur due to external electrical interference or malfunction of the EEG device (electrodes, wires, amplifiers, filters, power supply).

The main kinds of technical artifacts are grid line artifacts and fluctuations in electrode impedance. The grid line artifacts are caused by magnetic interference from sources of AC voltage. This artifact shows a typical frequency of 50 Hz or 60 Hz depending on the frequency of the grid line (in Brazil it is 60 Hz). It can be removed by the use of properly tuned filters without significant loss in the EEG signal information. Alternatively, short wires can be used between the electrode and the amplifier, or the measurements can be performed in a shielded room. Figure 3.12 shows the frequency spectrum of the EEG channels Fp1 and C3 in which the grid line artifact is present in the 60 Hz component. The phase spectrum shows no useful information. These EEG signals were acquired during the mental task of imagination of movement of the right hand, which occurred between 5 and 15 s. The unipolar method with the reference electrode on the left ear lobe and the ground electrode on the user's forehead was adopted.

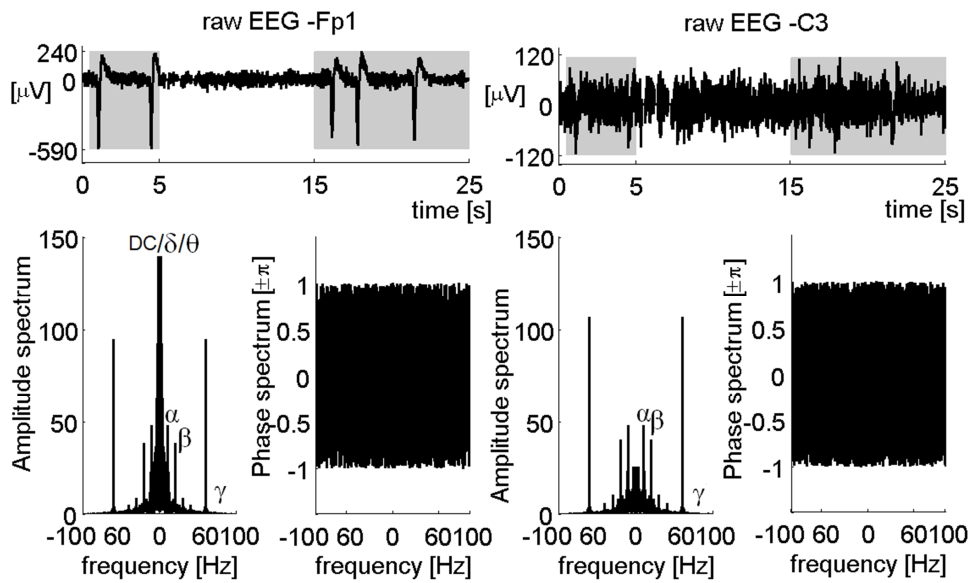


Figure 3.12 – EEG signal with grid line artifact and eye blinks artifacts (the mental tasks experiments are mentioned in chapter 3, section 3.8).

The artifacts due to fluctuations in electrode impedance are usually caused by poor fixation of electrodes and by sweating. The junctions skin-electrolyte and electrolyte-electrode cause a DC level in the electrode. This DC level reaches values from 0.1 to 1.7 V, which is much higher than the EEG signal. Therefore, it is necessary to use high pass filters in the input of the amplifiers (Lopes, 2005). Traditionally the EEG systems configure their high pass input filters by adjusting its time constant ( $\tau$ ) between 0.32 - 0.08 s (0.5 - 2.0 Hz)<sup>30</sup>.

The physiological artifacts originated from interference of the EEG with other biological signals, among which the main artifacts are the artifacts from eye movement, muscle artifacts and the electrocardiogram (ECG).

Artifacts from eye movement are due to eye movements which generate a continuous potential difference between the cornea and the retina that forms the electrical dipole for each eye (Figure 3.13 - A). The Cornea-Retinal Potential (CRP) amplitude is between 10 to 30 mV. This potential is mainly derived from the Retinal Pigment Epithelium (RPE) and it changes in response to background levels of retinal illumination. The eye movement causes a rotation of the dipole; and this signal, known as electrooculogram (EOG), is measured by skin electrodes placed near the inner and outer canthi of the eye (Figure 3.13 - B). The typical EOG amplitude is between 0.25 to

<sup>30</sup> The first-order high-pass filter cutoff frequency ( $f_c$ ) is given by:  $f_c = 1/2\pi\tau$ ,  $\tau = RC$ .

1 mV, which is much higher than the EEG amplitudes, with an essential frequency content of 0 to 30 Hz and higher energy at low frequencies (Marmor, et al., 2011). So, the EOG propagates through the skin to closer electrodes causing an increase or decrease in the EEG baseline, which mainly affects the  $\delta$  and  $\theta$  bands (Figure 3.13 - C) (Croft & Barry, 2000).

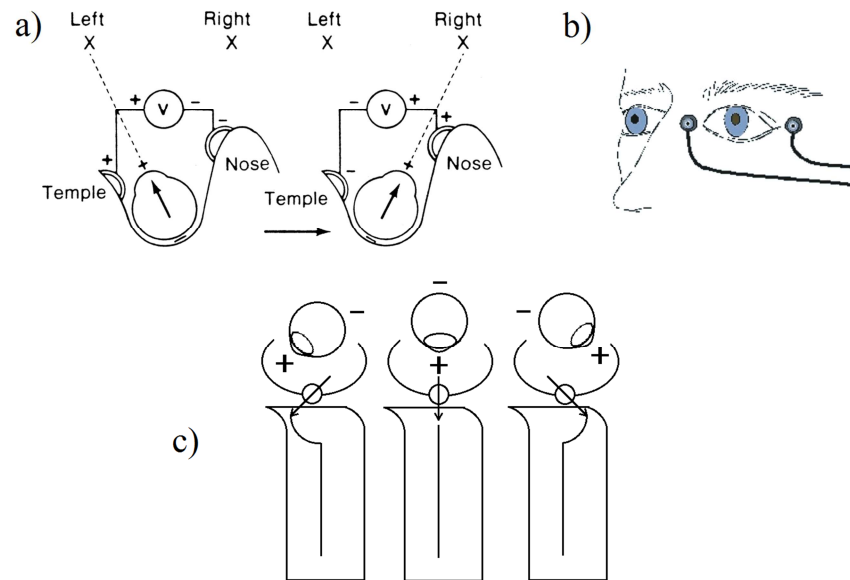


Figure 3.13 – a) EOG schematic; b) EOG electrode placement (Duane, 2006); c) Ocular dipole rotation affecting the EEG baseline.

Muscular artifacts are due to electrical signals related to muscle contraction (electromyography - EMG), particularly due to movements of the head, neck or eye blinks. Usually, the patient is asked to not move their eyes and not blink during the EEG acquisition. It is known that electrodes at temporal (T3, T4, T5 and T6) and lateral-frontal sites (F7 and F8) are particularly affected by facial muscle artifacts, from tension or jaw movements (Davidson et al., 2000). In general, frontal and temporal electrodes are more heavily contaminated by artifacts than central scalp channels (Jung et al., 2000). Eye blink artifacts are represented by a low frequency signal ( $< 4$  Hz) with high amplitude. It is a symmetrical activity mainly located on the frontal electrodes (Fp1 and Fp2) with low propagation. Eye movements are also represented by a low frequency signal ( $< 4$  Hz) but with higher propagation (Garcés & Leber, 2011).

Figure 3.12 - Left shows the raw EEG of channel Fp1, and Figure 3.12 - Right shows the raw EEG of channel C3. Five eye blink artifacts can be seen in the raw EEG of channel Fp1, which are the major peaks observed in the EEG signal. It is important to

mention that the signal from both channels, Fp1 and C3, were collected simultaneously in the same experiment. The channel C3 did not present visible eye blink artifacts, however, the frontal channel Fp1 that was closer to the artifact source was much more affected. From the graphics on the bottom of this figure it can be noted that the eye blink artifacts have low frequency components, usually below 10 Hz. The bilateral amplitude spectrum of channel Fp1 shows that the low frequencies of this channel have higher amplitudes than the low frequencies of channel C3. There are prominent peaks at approximately 10 Hz and 20 Hz in the bilateral amplitude spectrum of channel C3, and those peaks represent the  $\mu$  and  $\beta$  band activity. As the channel C3 did not present visible eye blink artifacts it could be erroneously concluded that the EOG artifact has little or no influence in channels that are distant from the artifact source, which in this case are the eyes.

But, the influence of the eye blink artifacts can be seen in the periodogram of channel C3, where there is low frequency activity occurring in the same instant in which the blink artifacts occurs in the channel Fp1. Figure 3.14 - Left shows the raw EEG of channel Fp1 and its periodogram. The middle part of Figure 3.14 shows the raw EEG of channel C3 and its periodogram and the right part of this figure shows the EEG of channel C3 high pass filtered and its periodogram.

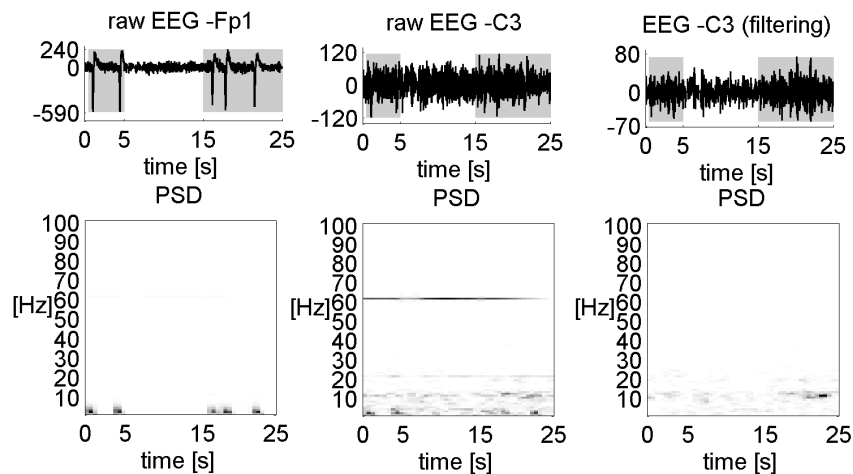


Figure 3.14 – Eye blink artifact on EEG. Left: EEG and periodogram of channel Fp1 heavily contaminated with low frequencies from eye blink artifacts; Middle: EEG and periodogram of channel C3 contaminated with low frequencies from eye blink artifacts and the artifact from the power grid line; Right: EEG and periodogram of channel C3 after applying the CAR method and a high pass filter with cutoff frequency of 5Hz.

The periodogram of the raw EEG of channel Fp1 shows the low frequency activity, below 5 Hz, related to the eye blinks. Even without eye blink peaks in the time course of the raw EEG of channel C3, its periodogram shows some low frequency activity related to the eye blinks. The periodogram of channel C3 also shows the grid line artifact (60 Hz) that proportionally affects this channel more than channel Fp1. Finally the EEG on the right part of Figure 3.14 shows the channel C3 after the application of the Common Average Reference (CAR) and a high pass filter with a cutoff frequency of 5 Hz. The periodogram of the filtered EEG highlights a peak of activity at around 10 Hz, which is a feature of interest for the identification of the mental task. Some methods for avoiding, detecting and discarding or minimizing the EOG and blink artifacts will be discussed in the next section.

ECG artifact due to the cardiac electrical activity can also be recorded on the scalp and affect the EEG. Figure 3.15 - A shows an EEG recording corrupted with ECG and EOG artifacts. Figure 3.15 - B and C show respectively real ECG and EOG signals. The peak of the QRS complex<sup>31</sup> of the ECG can be seen in the EEG signal and the EOG baseline fluctuations do influence the EEG baseline (Garcés & Leber, 2011). Another ECG related artifact is the ballistocardiogram (BCG). The BCG are micro-movements generated due to the heart pulsations that affects the EEG electrodes and wires (Ford, et al., 2004).

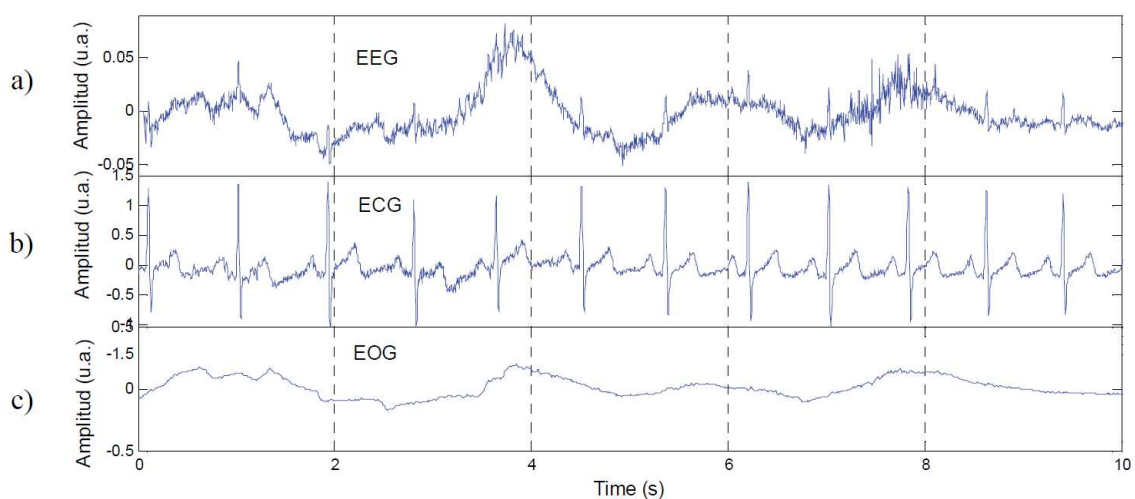


Figure 3.15 – a) EEG signal corrupted with ECG and EOG artifacts; b) ECG signal; c) EOG signal (Garcés & Leber, 2011).

<sup>31</sup> Typically an ECG has five deflections, arbitrarily named P, Q, R, S and T waves. The QRS complex is a name for the combination of three of the graphical deflections seen on a typical ECG. It is usually the central and most visually obvious part of the tracing. The peak of the QRS complex occurs at the R wave.

Beyond the interference from technical or physiological artifacts, the EEG is also affected by the electrical activity of the brain itself. The EEG of an area of interest is a mixture of unrelated signals from neighboring cortical areas that are scattered around and attenuated by the skull and scalp. It is also considered a special type of artifact, for which there are no exact solutions for separating it from the EEG signal. This problem is known as the inverse problem that traditionally has infinite solutions, due to the nature of its variables. A particular inverse solution using the calculation of Local Field Potential (LFP) is called ELECTRA (Grave de Peralta et al., 2005). Another solution uses the distribution of cortical extracellular currents, known as Cortical Current Density (CCD) (Cincotti et al., 2008).

### 3.5 Spatial filtering

Filtering methods are aimed to eliminate the frequency components in which the noise is present. For this purpose, high-pass, low-pass, band-pass or band-reject filters are used. As mentioned in the previous section, the grid line artifact has a well-defined spectral component around 50 or 60 Hz. Thus, a notch filter can be used to eliminate this kind of artifact. The physiological artifacts, such as the ECG, EMG and EOG, have overlapping spectral components with the EEG spectrum. Figure 3.16 shows an analysis of the coherence between the EEG signal of channels F3 and C3, measured by the bipolar method (Figure 3.8), and the EMG signal measured bilaterally in the deltoid while performing extension movements of the fingers (Grimann, et al., 2002). It may be noted that the spectra overlap throughout the range of frequencies (Figure 3.16 - B) and that the higher coherence is obtained between 6 and 16 Hz, completely corrupting the  $\alpha/\mu$  rhythm (Grosse, 2004).

Therefore, the filtering technique is not able to remove all the interference from the ECG, EMG and EOG signals. To minimize the artifact there are two classical approaches: the spatial filtering and some methods based on high order statistical separation (HOS).

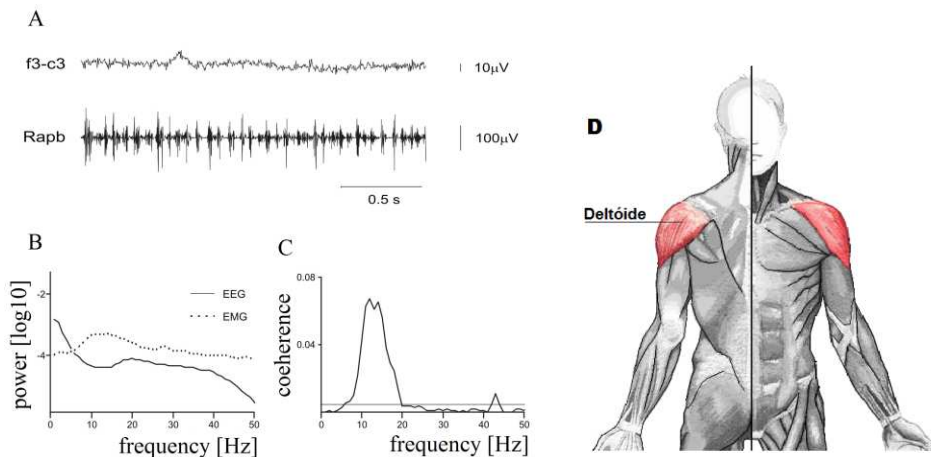


Figure 3.16 – (A) EEG (F3-C3) and EMG; (B) EEG and EMG Amplitude spectra; (C) Coherence between EEG and EMG. The horizontal gray line is the 95% confidence interval (Grosse, 2004); (D) Deltoid muscle.

Spatial filtering is applied to the raw EEG in order to reduce the correlation between channels caused by the spreading of the signal from the cortical source to the scalp and, therefore, improve the reliability of the BCI. Four spatial filters, namely a standard ear reference, a Common Average Reference (CAR), a small Laplacian, and a large Laplacian, will be discussed below. Figure 3.17 shows these four spatial filters in relation to the electrode C3 (highlighted in red). For CAR and Laplacian methods the mean activity of black electrodes is subtracted from the activity recorded in C3.

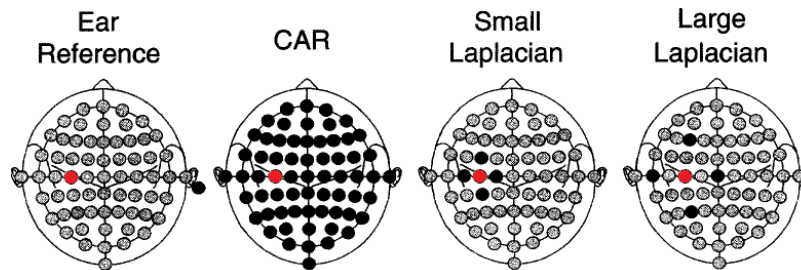


Figure 3.17 – Electrode location for the spatial filters analyzed (McFarland et al., 1997).

As mentioned in section 3.2, the CAR method is based on the assumption that external biological artifacts affect all EEG electrodes in approximately the same way, due to the considerable distance from the noise source to the electrodes on the scalp. Therefore, the CAR method requires the subtraction, sample to sample, of the average signals from the channels obtained from a common reference, such as the ear. As the common average prioritizes signals that are present in a large number of channels, the



subtraction leads to the elimination of these signs, working as a high-pass spatial filter (Estébanez, 2003; Azevedo, 2005).

The small Laplacian method requires the subtraction, sample to sample, of the average signals from the channels in a neighborhood within a radius of 3 cm around the analyzed channel, also obtained from a common reference, such as the ear. It also works as a high-pass spatial filter. The large Laplacian method works in the same way as the small Laplacian, and requires the subtraction, sample to sample, of the average signals from the channels in a neighborhood within a radius of 6 cm around the analyzed channel, also working as a high-pass spatial filter.

The study of spatial filters presented by McFarland et al. (1997) concluded that the CAR and large Laplacian methods would be suitable for BCIs based on the paradigm of motor imagination. The motor cortex has a radius of between 6 to 12 cm, thus, Laplacian filters over the motor cortex with a radius smaller than 6 cm would attenuate the information from the motor cortex itself. In this Thesis motor and non-motor related tasks were used, however, as the exact size of the brain areas that are active during the mental tasks is not known, the CAR method was adopted.

### **3.6 Methods for avoiding, discarding and minimizing artifacts**

As the spatial filters can not eliminate all artifact components, some methods for avoiding, detecting and discarding or minimizing the EOG and blink artifacts will be discussed. The first consideration for avoiding the EOG artifact is to provide a fixation point during the mental tasks that help in avoiding the eye movement artifact. For example, during our experiments subjects were instructed to observe a cross in the center of the screen, such as done by Ford, et al. (2004).

The simplest approach to deal with the remaining artifact is to perform a threshold analysis. For example, whenever EEG signals from selected frontal channels exceed  $\pm 50 \mu\text{V}$ , a 0.5 s time window centered around the EEG peak of these electrodes will be discarded in all EEG channels; such as was done by (Croft and Barry, 2000; Jung et al., 2000). Another simple alternative using the threshold analysis is to replace the identified artifact window by a filtered EEG. For example, during our experiments the identified artifact window was replaced by a filtered window using a FIR equiripple highpass filter set to 5 Hz, with a forward and reverse order filtering algorithm in order to cancel the effect of phase distortion.

Figure 3.18 shows the same trial previously shown in Figures 3.12 and 3.14 that is contaminated by five eye blink artifacts. Figure 3.18 shows the EEG of channels Fp1 and C3 and their periodograms for each signal. The periodogram was calculated by using the Power Spectral Density (PSD) with Hamming windows of 1 s overlapped by 25%. This figure shows the raw EEG, the application of the CAR method, the discarding of artifacts by using the threshold analysis and the filtering method. It can be seen that by only using the CAR method the low frequency artifacts of eye blink are still present in the periodograms of both channels, Fp1 and C3.

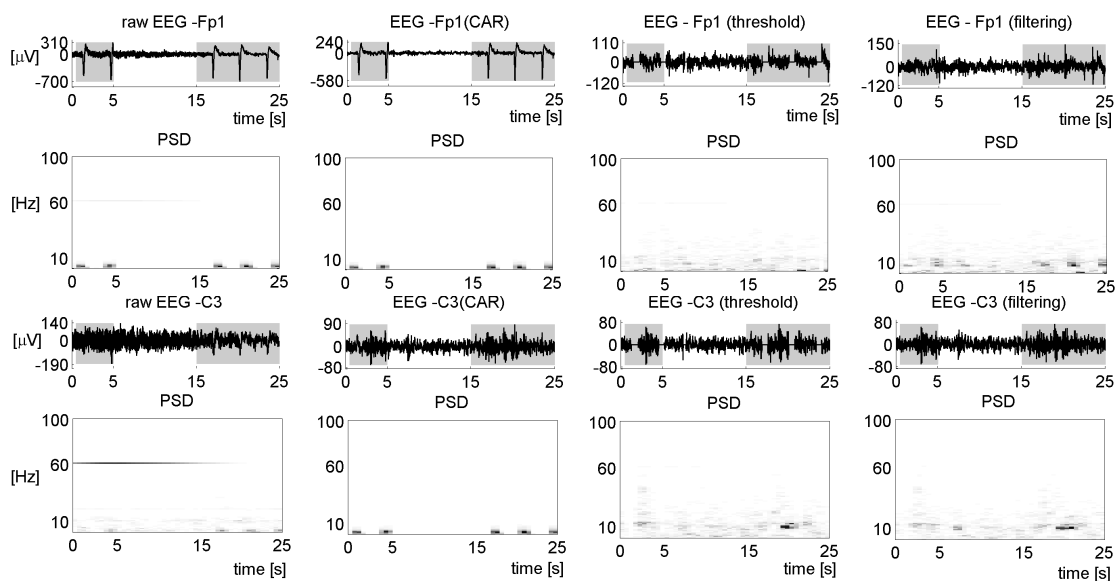


Figure 3.18 – EEG of channels Fp1 and C3 and their periodograms during the application of the following cases: raw EEG; CAR method; threshold analysis and filtering.

It can be seen that using the threshold approach the eye blink artifacts are completely annulled in channel Fp1 and there is no low frequency artifact in the periodogram. It can be noted in channel C3 that using the threshold and the filtering approaches a peak of activity around 10 Hz becomes evident between 15 and 25 s, and that peak of activity lasts longer for the filtering approach because the threshold approach causes a loss of information. As aforementioned, this peak of activity at around 10 Hz represents an ERS occurring at the  $\mu$  band and it is a feature of interest for the identification of the mental task.

Some more complex approaches include performing Blind Source Separation (BSS) using HOS methods as Independent Component Analysis (ICA) (Croft & Barry, 2000, Jung et al., 2000, 2001, Ford et al., 2004). In summary, the BSS problem is to

perform the separation of a set of signals from a set of mixed signals, without the aid of information, or with very little information, about the source signals or the mixing process. BSS relies on the assumption that the source signals are not correlated with each other. Here, the mixed signals correspond to the EEG signal mixed with an unknown noise and the BSS problem is related to performing the separation of a set of source signals, i.e. EEG artifact-free signals, from the set of mixed signals.

ICA is a method for solving the BSS problem recovering  $N$  independent source signals,  $\mathbf{s}$ , from  $N$  linear mixtures,  $\mathbf{x}$ , and it relies on the assumption that the source signals are stationary and mutually statistically independent or decorrelated while their mixtures are not. Statistical independence requires that all second-order and high order correlations are zero, while decorrelation only seeks to minimize second-order statistics, which are the covariance or correlation. The linear mixture of  $N$  sources with  $M$  samples each one, can be written as,

$$\begin{cases} x_1(k) = a_{1,1} \cdot s_1(k) + a_{1,2} \cdot s_2(k) + \dots + a_{1,N} \cdot s_N(k) \\ \vdots \\ x_N(k) = a_{N,1} \cdot s_1(k) + a_{N,2} \cdot s_2(k) + \dots + a_{N,N} \cdot s_N(k) \end{cases}, \quad k = 1, 2, \dots, M. \quad (3.5)$$

or using matrix notation,

$$\begin{bmatrix} x_1(1) & \dots & x_1(M) \\ \vdots & \ddots & \vdots \\ x_N(1) & \dots & x_N(M) \end{bmatrix} = \begin{bmatrix} a_{1,1} & \dots & a_{1,N} \\ \vdots & \ddots & \vdots \\ a_{N,1} & \dots & a_{N,N} \end{bmatrix} \cdot \begin{bmatrix} s_1(1) & \dots & s_1(M) \\ \vdots & \ddots & \vdots \\ s_N(1) & \dots & s_N(M) \end{bmatrix},$$

$$\mathbf{x} = \mathbf{A} \cdot \mathbf{s} \leftrightarrow \mathbf{s} = \mathbf{A}^{-1} \cdot \mathbf{x} \leftrightarrow \mathbf{s} = \mathbf{W} \cdot \mathbf{x}. \quad (3.6)$$

where,  $\mathbf{A}$  is an unknown invertible matrix given by an ICA algorithm. Once  $\mathbf{A}$  is known, the source signals can be found by inverting the mixing process, leading to the “unmixing” or separating matrix  $\mathbf{W}$ . The rows of the input matrix,  $[x_1(k), x_2(k), \dots, x_N(k)]^T$ , are EEG signals recorded at different channels and columns;  $[x_i(1), x_i(2), \dots, x_i(M)]$  are measurements recorded at different time points. The columns of the source matrix,  $\mathbf{s}$ , contain the time course of ICA components. The columns of  $\mathbf{A}$ ,  $[a_{i1}, a_{i2}, \dots, a_{iN}]$ , give the relative projection strengths of the respective ICA components at each EEG site. These scalp weights represent the fixed scalp topography of each ICA component, and provide evidence for the component physiological origin. For example, the EOG and blink artifacts should project mainly to

frontal sites, the ICA components with high weight projected to the frontal sites, should be related to this kind of artifact, which can also be verified in the time course of the component (Vigário et al., 2000; Jung et al., 2000; 2001).

The ICA components related to artifacts can then be set to zero and artifact-free signals can be obtained projecting non-artifactual ICA components back onto the scalp. The artifact-free EEG signals,  $\mathbf{x}_0$ , can be obtained from the artifact-free source matrix,  $\mathbf{s}_0$ , and the mixing matrix  $\mathbf{A}$  by  $\mathbf{x}_0 = \mathbf{A} \cdot \mathbf{s}_0$  (Jung et al., 2000, 2001). Figure 3.19 shows the ICA components and their fixed scalp topography of the same trial analyzed in Figures 3.12, 3.14 and 3.18. This experiment corresponds to the mental task of imagination of movement of the right hand, which occurred between 5 and 15 s, and 19 electrodes positioned according to the international 10-20 system (Figures 3.5 - A and B). Then the input matrix has 19 linear mixtures, and the ICA algorithm results in 19 independent components and 19 respective scalp topographies shown on the right side of each component. In the scalp topography, the relative strength of the ICA component over the 19 scalp sites is shown in shades of gray, in which light shades are related to a high strength value, positive or negative, and dark shades are related to near zero strength values.

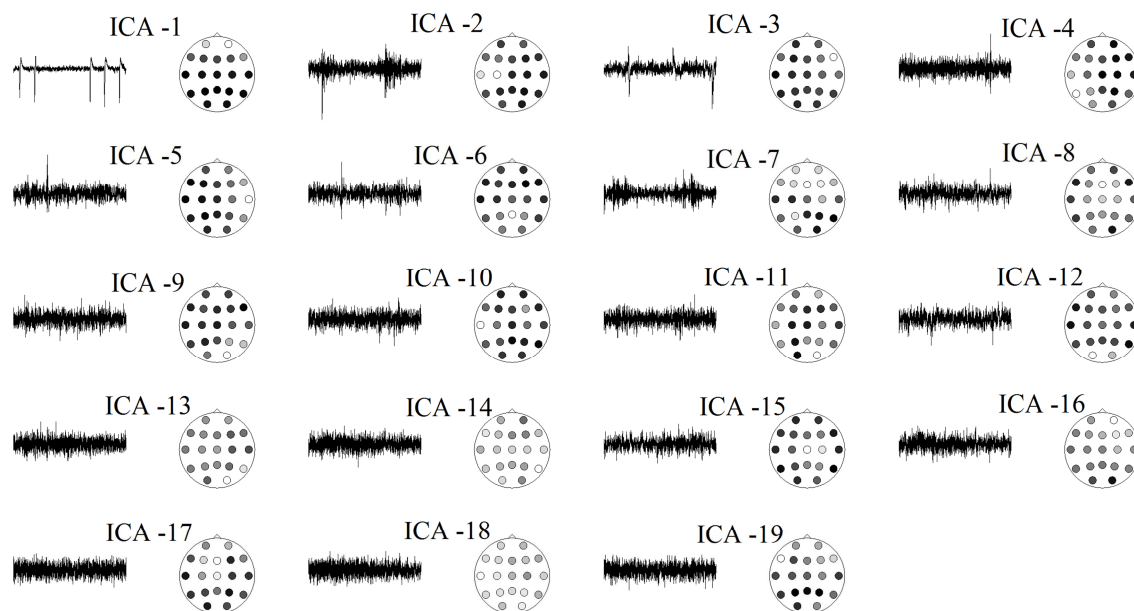


Figure 3.19 – ICA components obtained by “fastICA” algorithm and their fixed scalp topographies.

In Figure 3.19, it can be seen that the first ICA component (ICA-1) is very similar to the time course of the eye blink artifact shown in the EEG of channel Fp2 in

Figures 3.12, 3.14 and 3.18. The scalp topography of this component is shown at its right side, and it can be seen that its strength is higher for frontal sites, in particular at Fp2. This component can then be set to zero in order to obtain a relative artifact-free EEG. Figure 3.20 shows the minimization of eye blink artifacts of the trial of figures 3.12 and 3.18 by using two ICA algorithms, which are the “fastICA” and the “runica”. It can be seen that for both algorithms the eye blink artifacts are completely annulled in channel Fp1 and there is no low frequency artifact in the periodogram. In channel C3 can be noted a peak of activity around 10 Hz, between 15 and 25 s, although the “runica” algorithm clearly distorted the original EEG amplitude.

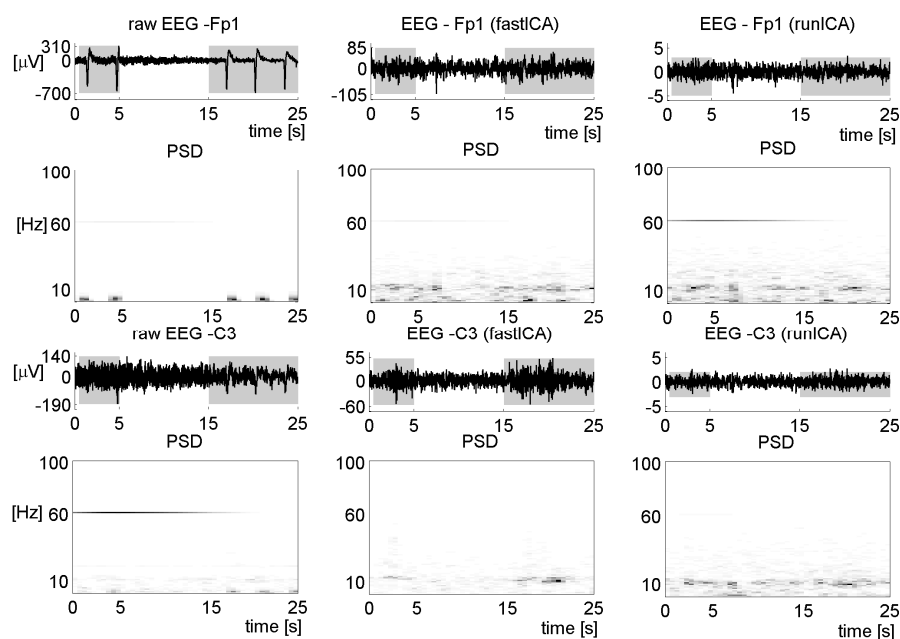


Figure 3.20 – EEG of channels Fp1 and C3 and their periodograms during the application of the following cases: raw EEG; “fastICA” algorithm and “runica” algorithm.

The two mentioned ICA algorithms are based on the two broadest definitions of independence for the ICA that are the maximization of the non-Gaussianity and the minimization of the mutual information (MMI) (Croft & Barry, 2000, Jung et al., 2000, Jung et al., 2001, Ford et al., 2004). The non-Gaussianity family of ICA algorithms, which includes “fastICA” algorithm, is based on measures of non-Gaussianity like kurtosis and negentropy (Hyvärinen, 1999). As the Gaussian distribution has above second order cumulants equal to zero, the functions of its third and fourth cumulants, as

the skewness<sup>32</sup> and kurtosis<sup>33</sup>, are also zero, and thus, they are used as a measure for non-Gaussianity. The negentropy<sup>34</sup>, or differential entropy, can also be approximated by a function of the first and fourth order cumulants, and therefore, it is also used as a measure of non-Gaussianity. The “fastICA” is a fixed point algorithm which, maximizing the absolute value of the kurtosis, leads to the identification of the non-Gaussian sources (Vigário et al., 2000).

The MMI family of ICA algorithms, which includes the “runica” algorithm, uses measures like Kullback-Leibler Divergence<sup>35</sup> ( $D_{KL}$ ) and maximum-entropy. The “runica” performs ICA decomposition of input data using the logistic “infomax” algorithm described by Bell and Sejnowski in 1995. The “infomax” is an optimization principle in which a set of input values (I) are mapped to a set of output values (O) that are chosen, or learned, in order to maximize the average Shannon mutual information between the input and the output,  $H(O;I)$ . The mutual information can also be understood as the expectation of  $D_{KL}$  of the conditional distribution of O given I,  $p(o|i)$ , and the univariate distribution of O,  $p(o)$ . Then,  $H(O;I) = E[D_{KL}(p(o|i)||p(o))]$ , and the greater the difference in the distributions  $p(o|i)$  and  $p(o)$ , the greater the information gain.

For more details, the conditional probability is explained in section 4.6 of chapter 4, when dealing with the classifier. The Kullback-Leibler Divergence is explained in section 4.5 during the feature selection topic. In chapter 5, a comparison between the average processing time of each minimizing artifact method discussed here will be presented regarding its utilization for online BCI operation.

### 3.7 EEG records and SNR

Diverse types of EEG record signals exist and each one functions to show the electrical behavior of the brain during different activities. Spontaneous potentials are basic components of the EEG signal that may be present throughout the range of

---

<sup>32</sup> The measure of skewness of a probability distribution is given by,  $\gamma_1 = k_3/(k_2^{3/2})$ , where  $k_i$  is the  $i^{\text{th}}$  cumulant of the probability distribution.

<sup>33</sup> The kurtosis, from the Greek word *kurtos*, meaning curved, is a measure of flatness of a probability distribution and it is given by,  $\gamma_2 = k_4/k_2^2$ , where  $k_i$  is the  $i^{\text{th}}$  cumulant.

<sup>34</sup> The negentropy,  $J(x)$ , of a random variable  $x$  can be approximated by,  $J(x) \approx (1/12) \cdot [k_1(x^3)]^2 + (1/48) \cdot [\gamma_2(x)]^2$ , where  $k_1$  is the first cumulant, i.e. the expected value of  $x$ ,  $E[x]$ , and  $\gamma_2$  is the kurtosis.

<sup>35</sup> The Kullback–Leibler divergence, or information divergence, is a non-symmetric measure of the difference between two probability distributions P and Q, denoted  $D_{KL}(P||Q)$ . For discrete probability distributions P and Q, the K–L divergence of Q from P is defined as  $D_{KL}(P||Q) = \sum_i \ln(P(i)/Q(i)) \cdot P(i)$ .

frequencies of the EEG signal and are not produced by sensory stimulation. Event-Related Potential (ERP) is the change of the EEG potential in response to a particular event. Typically, the EEG recorded is referenced to the event, i.e., the time is regarded as the time of occurrence of the event. Thus, the recording time before the event is considered negative and the later time is considered positive (Delamonica, 1984).

ERP has a much lower amplitude than spontaneous activity, such that it can not be recognized in the raw EEG signal. Therefore, averaging techniques are commonly employed for detecting the ERP. In the averaging technique the ERP is considered to occur with an approximately constant delay in relation to the event, and the spontaneous activity is modeled as an additive random noise (Figure 3.21 - Left) (Rugg & Coles, 1996). The EEG recordings obtained by repeating the same experiment or trial, under the same conditions, are called epochs, and as the number of epochs,  $N$ , used in the calculation of the average increases, the time-locked activity stresses, their signal-to-noise ratio (SNR) increases, the spontaneous activity decreases and the ERP can be observed (Luck, 2005).

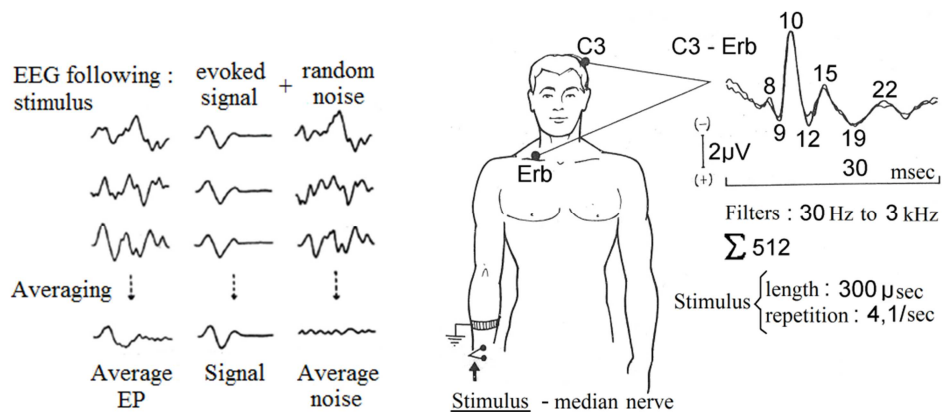


Figure 3.21 – Left: ERP observation by averaging EEG recordings (Rugg & Coles, 1996); Right: Normal somatosensory evoked potential (adapted from Delamonica, 1984).

The signal-to-noise ratio (SNR) is defined as the ratio of the average power in the signal and the average power in the noise (Garcia, 1994). As more epochs are used, the SNR of the time-locked event increases, allowing the observation of the ERP (Luck, 2005). In the ideal case it is assumed that the measured EEG signals  $x(t,k)$  are made up of a sequence of event-locked ERPs  $s(t)$  with invariable latency and shape, and the noise  $n(t,i)$  that can be approximated by a zero-mean Gaussian random process that is

uncorrelated<sup>36</sup> between trials and not time-locked to the event; where  $i$  is the trial number and  $t$  is the time elapsed after the  $i^{\text{th}}$  event. The signal  $s(t)$  does not depend on a specific trial ( $k$ ) while the noise does,  $n(t,k)$ .

The average power of the ERP signal is given by the expected value of its energy,  $E[s^2]$ . When a signal is a stationary<sup>37</sup> stochastic process, its power is defined to be the value of its correlation function,  $\rho_{t,\tau}$ , at the origin. As the noise is supposed to be a stationary zero-mean Gaussian random process, its mean,  $\mu_t$ , and variance,  $\sigma_t^2$ , do not vary with respect to time ( $\mu_0, \dots, \mu_t = 0$  and  $\sigma_0^2, \dots, \sigma_t^2 = \sigma^2$ ). The correlation function at the origin,  $\rho_{t,0}$ , is then equal to its variance,  $\sigma_n^2$ . The SNR between the ERP and the noise of any trial is given by

$$SNR = \frac{E[s^2]}{\sigma_n^2}. \quad (3.7)$$

where  $E[\cdot]$  is the expected value operator. Now the SNR is estimated as the average of EEG trials are taken. First, each EEG recorded can be written as

$$x(t, k) = s(t) + n(t, k). \quad (3.8)$$

the average of  $N$  trials of  $x(t, k)$  is given by,

$$ERP(t) = \bar{x}(t) = \frac{1}{N} \sum_{i=1}^N x(t, i) = \frac{1}{N} \sum_{i=1}^N s(t) + n(t, i) = s(t) + \frac{1}{N} \sum_{k=1}^N n(t, i). \quad (3.9)$$

The expected value of  $\bar{x}(t)$  is the signal  $s(t)$  itself because the noise is approximated by a zero-mean random process, and its expected value in any trial is zero,

---

<sup>36</sup> Two random variables  $X$  and  $Y$  are said to be uncorrelated if their covariance  $\sigma_{X,Y}$  is zero. If  $X$  and  $Y$  are independent, then they are uncorrelated. However, not all uncorrelated variables are independent.

<sup>37</sup> A random process is stationary if the joint distributions of any set of samples does not depend on the placement of the time origins. As the noise is a Gaussian random process, and the Gaussian probability distribution only depends on the two first cumulants that are the mean and the variance, it implies that they are time independent.



$$E[\bar{x}(t)] = E\left[s(t) + \frac{1}{N} \sum_{k=1}^N n(t, i)\right] = E[s(t)] + \frac{1}{N} \sum_{k=1}^N E[n(t, i)] = s(t). \quad (3.10)$$

Now let's calculate the variance of  $\bar{x}(t)$ ,

$$\begin{aligned} \sigma_{\bar{x}(t)}^2 &= E[(\bar{x}(t) - E[\bar{x}(t)])^2] = E\left[\left(\left(s(t) + \frac{1}{N} \sum_{i=1}^N n(t, i)\right) - s(t)\right)^2\right] \leftrightarrow \\ \sigma_{\bar{x}(t)}^2 &= E\left[\left(\frac{1}{N} \sum_{i=1}^N n(t, i)\right)^2\right] = \frac{1}{N^2} E\left[\sum_{i=1}^N n(t, i) + \sum_{i \neq j} n(t, i) \cdot n(t, j)\right] \leftrightarrow \\ \sigma_{\bar{x}(t)}^2 &= \frac{1}{N^2} E\left[\sum_{i=1}^N n(t, i)\right] + \frac{1}{N^2} E\left[\sum_{i \neq j} n(t, i) \cdot n(t, j)\right] \leftrightarrow \\ \sigma_{\bar{x}(t)}^2 &= \frac{1}{N^2} \sum_{i=1}^N E[n(t, i)] + \frac{1}{N^2} \sum_{i \neq j} E[n(t, i) \cdot n(t, j)]. \end{aligned} \quad (3.11)$$

The second sum of eq. 3.11 represents the covariance combinations between two zero mean noise trials. As the noise signal is uncorrelated between trials, then the covariance  $\sigma_{n(t,i),n(t,j)}$  of a sample  $t$  between any two trials ( $i$  and  $j$ ) is null and it can be discarded,

$$\begin{aligned} \sigma_{n(t,i),n(t,j)} &= E[(n(t, i) - E[n(t, i)]) \cdot (n(t, j) - E[n(t, j)])] = 0 \leftrightarrow \\ \sigma_{n(t,i),n(t,j)} &= E[n(t, i) \cdot n(t, j)] = 0. \end{aligned} \quad (3.12)$$

by substituting eq. 3.12 into eq. 3.11, it gives that,

$$\sigma_{\bar{x}(t)}^2 = \frac{1}{N^2} \sum_{i=1}^N E[n(t, i)] + \frac{1}{N^2} \sum_{i \neq j} \sigma_{n(t,i),n(t,j)} = \frac{1}{N^2} \sum_{i=1}^N E[n(t, i)^2]. \quad (3.13)$$

and as the noise is zero-mean, eq. 3.13 can be rewritten to,

$$\sigma_{\bar{x}(t)}^2 = \frac{1}{N^2} \sum_{i=1}^N E[n(t, i)^2] = \frac{1}{N^2} \sum_{i=1}^N E[(n(t, i) - E[n(t, i)])^2] = \frac{1}{N^2} \sum_{i=1}^N \sigma_{n(t, i)}^2. \quad (3.14)$$

then, since the variance of the sum of uncorrelated variables is additive and the variance of the noise averaged during  $N$  trials is given by

$$\sigma_{\bar{n}(t)}^2 = \frac{1}{N} \sum_{i, j=1}^N \sigma_{n(t, i), n(t, j)} = \frac{1}{N} \left( \sum_{i=1}^N \sigma_{n(t, i)}^2 + \sum_{i \neq j} \sigma_{n(t, i), n(t, j)} \right) = \frac{1}{N} \sum_{i=1}^N \sigma_{n(t, i)}^2, \quad (3.15)$$

by substituting eq. 3.15 into eq. 3.14, the variance of  $\bar{x}(t)$  is given by

$$\sigma_{\bar{x}(t)}^2 = \frac{1}{N} \cdot \sigma_{\bar{n}(t)}^2. \quad (3.16)$$

Equation 3.16 shows that the variance of sample  $t$  of the average signal  $\bar{x}(t)$  across the trials decreases proportionally to the total number of trials,  $N$ . For this reason, the noise amplitude of the average of  $N$  trials is  $1/\sqrt{N}$  times that of a single trial (Luck, 2005). And the SNR obtained for each new added trial would be given by

$$SNR = \frac{E[s^2]}{\sigma_{\bar{x}(t)}^2} = \frac{E[s^2]}{\frac{\sigma_{\bar{n}}^2}{N}} = N \frac{E[s^2]}{\sigma_{\bar{n}}^2}. \quad (3.17)$$

Then, equation 3.17 shows that the SNR of the EEG increases proportionally to the number of trials and an excessive number of epochs will not result in significant changes in the ERP curve (Luck, 2005). Based on the relation found in equation 3.17 a study comparing the ERP SNR of the motor mental task of imagination of movement of the right hand and the mental task of music imagery will be detailed in chapter 5, section 5.8.

Event-related potentials (ERPs) were originally called evoked potentials (EPs) because they are electrical potentials that are evoked by stimuli, as opposed to the spontaneous EEG rhythms. Concerning the terminology, Herb Vaughan, wrote in 1969 "Since cerebral processes may be related to voluntary movement and to relatively stimulus-independent psychological processes, the term evoked potentials is no longer

sufficiently general to apply to all EEG phenomena related to sensorymotor processes. Moreover, sufficiently prominent or distinctive psychological events may serve as time references for averaging, in addition to stimuli and motor responses. The term Event-Related Potentials (ERP) is proposed to designate the general class of potentials that display stable time relationships to a definable reference event.” (Luck, 2005).

Then, the ERP may be related to voluntary movement or to relatively stimulus-independent psychological processes, as the mental tasks. Depending on the modality to be studied, it can use a somatosensory, visual or auditory stimuli and it has an important clinical utility for detecting neural degenerative diseases and traumatic pathologies (Delamonica, 1984). EPs can be measured over specific areas of the cortex when certain nuclei of the thalamus are stimulated. These nuclei are called specific thalamic nuclei. Among them, e. g., are the Ventral Posterolateral nucleus (VPL) of the thalamus and the Medial Geniculate Nucleus of the thalamus (MGN) (Figure 2.11), whose stimulation evoke potentials, respectively, in the somatosensory, and auditory areas of the cortex (Machado, 2007).

As previously mentioned, EPs and ERPs are observed by means of hundreds of EEG recordings made with the same type of stimulus in order to eliminate the effect of random noise and enhance the event-locked response. A temporal pattern related to the event then becomes evident in the average EEG. The right part of Figure 3.21 shows a normal somatosensory evoked potential, wherein the first high-voltage negative potential, with latency of 10ms, corresponds to the Action Potential (AP) of the stimulated nerve. The numbers on the peaks of the EP curve indicate the latencies in milliseconds. The number in the summation indicates that the potential of the figure is the result of the average of 512 EEG recordings (Delamonica, 1984).

### 3.8 Movement-related potentials

The Movement-Related Potentials are ERPs measured over the motor cortex that have about 1  $\mu\text{V}$  and are generated in response to an intention, or volition, to move a limb (Azevedo, 2005). One kind of MRP is the Bereitschaftspotential<sup>38</sup> (BP), also called Readiness Potential (RP) (Figure 3.22). The BP can be roughly identified in single-trial measurements and it is widely used in BCI applications, so it will be described in more detail. The BP is related to the pre-motor planning of volitional movement occurring in

---

<sup>38</sup> from German, “readiness potential”.

the motor cortex (M1) and supplementary motor area (SMA). The BP amplitude is ten to hundred times smaller than the  $\alpha$  rhythm amplitude, therefore to observe it in detail it is necessary to perform averaging. BP has two components, the early one (BP1) lasting from about -1.2 to -0.5 s, and the late component (BP2) lasting from -0.5 to shortly before 0 s.

The BP study has precipitated an interesting worldwide discussion about free will that lasts for almost 30 years. Benjamin Libet studied in the 1980s the relationship between conscious experience of volition and the BP, and he found that the BP started about 0.35 s earlier than the subject's reported conscious awareness of the desire to make the movement. Libet's experiments suggest that the true initiator of volitional acts is some unconscious processes in the brain. Therefore, free will plays no part in their initiation. Since the subjective experience of the conscious will to act preceded the action by only 200 ms, this leaves consciousness only 100-150 ms to veto an action (Figure 3.22). This occurs because the final 50 ms prior to an act are occupied by the activation of the spinal motor neurons by the primary motor cortex. Libet concluded that we have no free will in the initiation of our movements, but, since subjects were able to prevent intended movement at the last moment, we do have the ability to veto these actions, sometimes called the “free won't” (Libet, 1985).

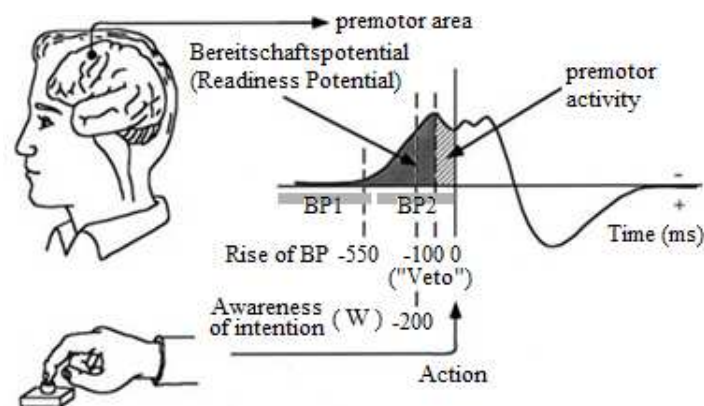


Figure 3.22 – Bereitschaftspotential and the Libet’s experiment. At -550 ms: the rise of BP; at -200 ms: the awareness of intention; at -100 ms: the possibility of veto of the action; at 0 s: the action of pressing a button.

Soon et al., in 2008, performed an experiment with 36 right handed subjects that could freely decide to move their left or right index finger at any time, while in the meantime their brain activity was measured using the fMRI. Most of the intentions (88.6%) were reported to be consciously formed 1 s before the movement and support-

vector machines (SVMs) were trained with fMRI data from several brain areas to predict the specific outcome of a subject's motor decision. The study showed that the activity of the frontopolar and parietal cortices allowed the prediction of the finger laterality (left/right) 8 s before the action and allowed the time prediction (when the action would occur) 6 s before the action. They concluded that the earliest predictive information is encoded in the frontopolar and parietal cortices, and not in the SMA, suggesting that the subjective experience of freedom is no more than an illusion and that our actions are initiated by unconscious mental processes long before we become aware of our intention to act (Soon et al., 2008). Recently, Hans Helmut Kornhuber and Lüder Deecke, who first recorded and reported the BP in 1964, advocate that we have free will for the initiation of our movements and actions, but there is no absolute freedom, which would mean freedom from nature which is impossible. It is a relative freedom that was referred to as freedom in "degrees of freedom".

In contrast with most ERPs and BP, some brain events may not be observed in the EEG signal by using a simple linear technique such as the average over the time. Some events are restricted to certain EEG rhythms and are called phase-locked events. The relative decrement and increment of energy that occurs in specific frequency bands are called Event-Related Desynchronization (ERD) and Event-Related Synchronization (ERS), respectively (Pfurtscheller & Lopes, 1999). During the mental task an ERD can be observed, which is followed by an ERS when the mental task is over. The events related to an ERD/ERS and how they are measured will be the topic of the next section.

### **3.9 ERD/ERS**

As aforementioned, the EEG measures the activity of neural masses working in synchrony. Usually when a population of cortical neurons is inactive, these neurons receive a thalamic rhythmic afference that keeps them synchronized, thus, the sum of these rhythmic signals has a large amplitude. When a neural mass is activated by a stimulus or an intention, cortical neurons receive distinct and specific signals, causing loss of synchrony. The resulting sum of these desynchronized signals has a lower amplitude which causes an ERD (Bear, et al., 2008).

The bottom signal of Figure 3.11 shows the  $\alpha$  rhythm attenuation, observed over V1, when the eyes are opened. The attenuation of  $\alpha$  rhythm amplitude when the eyes are open is an ERD, and the increase in the amplitude of the  $\alpha$  rhythm when the eyes are

closed is an ERS. As discussed in section 2.5, the motor imagination inhibits the synchronization of M1 with the rhythmic activity of the thalamus, causing an ERD similar to the ERD observed over V1. The  $\mu$  rhythm was described by Jasper and Andrews (1938, apud Beisteiner, et al., 1995) as the “precentral  $\alpha$  rhythm”, because it occurs under similar conditions to the  $\alpha$  rhythm, but in the precentral area, over the motor cortex. The electrodes on the precentral area (C3, Cz and C4) can then measure an ERD in the EEG signal during motor mental tasks. Even subjects with limb amputations present an ERD during the imagination of movement of the phantom limb.

The ERD generated during the performance of the motor mental task of imagination of movement of the hand is contralateral and, therefore, the mental task related to the right hand causes an ERD at the  $\mu$  band of M1 in the left brain hemisphere, which can be measured by the electrode C3. The mental task of imagination of movement of the left hand causes an ERD at the  $\mu$  band of M1 in the right brain hemisphere, which can be measured by the electrode C4. While performing the mental task of imagination of movement of the hands, the M1 hand area is activated, as well as the adjacent areas SMA and PMA (Figures 2.3 and 2.12). R. Beisteiner et. al. (1995) showed that the DC potential difference between the electrodes C3 and C4 is higher during the imagination of movement of the right hand than during the imagination of movement of the left hand (Figure 3.23)

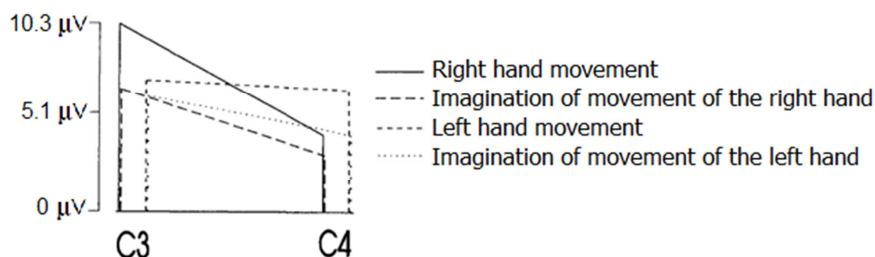


Figure 3.23 – DC potential of electrodes C3 and C4 (adapted from Beisteiner, et al., 1995).

The left hemisphere is involved with visual-spatial imagination that is activated during the planning of both mental tasks, thus it has dominant contribution on the motor imagination. The left hemisphere is then somewhat active for the mental tasks of both hands and by imagining the movement of the right hand this potential is summed with the potential related to the activation of M1 that is also in the left hemisphere. While for the imagination of movement of the left hand there will be a potential regarding the

activation of left hemisphere and the activation of M1 from the right hemisphere, therefor the potential difference between the electrodes C3 and C4 will be lower.

The classical method to measure the ERD/ERS is described by Gert Pfurtscheller and Fernando H. Lopes da Silva (1999), and is similar to the process to obtain an ERP, but it includes filtering and squaring the signal. Given a set with multiple EEG recordings (epochs), the signals are filtered in the desired frequency range, and then the signals are squared obtaining the signal energy. Then, the average energy of all epochs is calculated in order to increase the SNR, making it possible to observe the ERD/ERS pattern. Here, the signal energy is used to prevent the cancelation of positive and negative EEG amplitudes during the average process. The curve obtained so far may be smoothed by using the moving average technique. Finally, as the ERD/ERS are measured as percentages, the average energy of a previous reference period,  $R$ , is calculated. Thus, the relative signal energy,  $A$ , can be measured in relation to a reference period, as given by

$$ERD(\%) = \frac{(A - R)}{R \times 100} . \quad (3.18)$$

Figure 3.24 shows the application of the classic method for measuring the ERD/ERS pattern. Our experiment to observe the ERD/ERS used 60 epochs in which the subject performed the motor task of right hand imagination of movement. In this experiment the subject was instructed to imagine the movement of the right arm and hand in order to reach and grab an object placed in a table in front of him at a distance of 30 cm. The subject was instructed to repeatedly perform this imaginary movement, at his own pace, from 5 to 15 s of the EEG record.

Figure 3.24 - A shows in gray the superimposition of the EEG from channel C3 of the first, fifteenth, and thirtieth epochs, respectively, in black, dark and light gray. The mental task lasted 10 s, occurring between 5 and 15 s of the EEG record, which corresponds to the central area, not hatched of figure. Figure 3.24 - B shows the EEG filtered at the  $\mu$  band. In this study we used a FIR equiripple bandpass filter with a forward and reverse order filtering algorithm to cancel the effect of phase distortion. This figure also shows the superimposition of the filtered EEG of the three aforementioned epochs. The objective of this figure is not to show individual

characteristics of the epochs, but just to emphasize that the steps are performed individually, for each epoch.

In this work, the reference period is the one between 1 s and 3 s of the recording, which is highlighted in Figure 3.24 - E as the interval shaded in dark gray. The horizontal line stresses the null value of the reference period. In Figure 3.24 - E the energy decrease of around 70 % occurring between 5 s and 15 s is the ERD, and the energy increase of around 60 % occurring between 15 s and 20 s is the ERS. Therefore, the ERD/ERS pattern can be observed mainly at electrodes placed over the scalp region of the motor cortex during motor mental tasks.

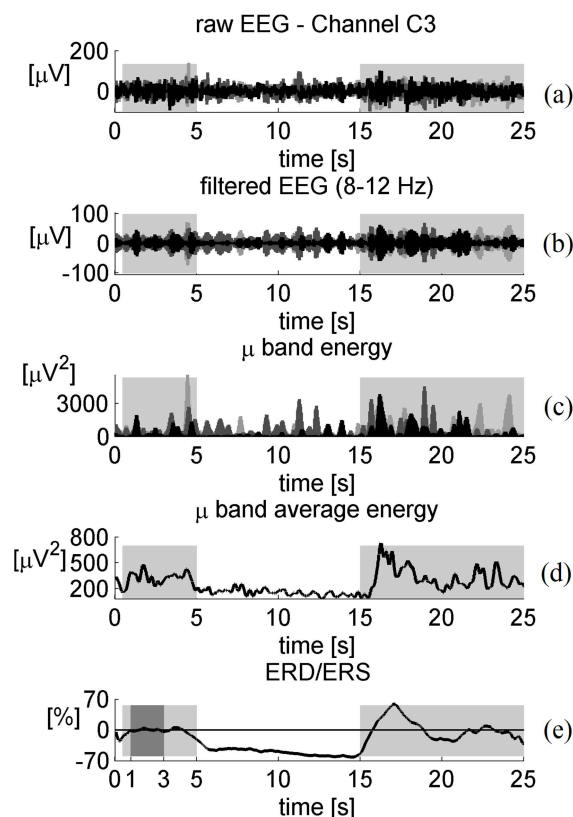


Figure 3.24 – ERD/ERS calculation method. The reference period was taken between 1 and 3 s and the motor mental task occurred between 5 and 15 s. (a) raw EEG from channel C3 during the first, fifteenth, and thirtieth epoch, respectively in black, dark and light gray; (b) EEG from channel C3 filtered at  $\mu$  band; (c) channel C3  $\mu$  band energy (d) channel C3  $\mu$  band average energy of 60 epochs; (e) channel C3  $\mu$  band ERD/ERS.

As previously mentioned, the ERD/ERS patterns of visual cortex can be observed directly by electrodes O1 and O2 through a frequency analysis without the need of averaging. The primary visual cortex (V1) is located on the occipital lobe which is in the posterior region of the brain, and roughly isolated from other lobes. Thus, the signals from V1 do not suffer much interference from signals of other brain areas, and



the ERD/ERS pattern can be observed with a single EEG recording. However, the motor cortex is at the center of the brain surrounded by the frontal, temporal and occipital lobes thus the signals generated by neighboring areas are mixed with signals from M1 and the signal measured by electrodes C3, Cz and C4 contain a mixture of signals from different brain areas. Therefore, the ERD/ERS pattern generated in M1 during a limb imagination of movement can not be observed with a single EEG recording. So, it is necessary to calculate the average over a number of epochs, as described by G. Pfurtscheller and F. H. Lopes da Silva (1999).

The procedure described above can not be used for an online classifier because it is necessary to observe the ERD/ERS in only one epoch. A second method for obtaining the ERD/ERS is described by J. Kalcher and G. Pfurtscheller (1995). Often, evoked potentials spontaneously occurring in the brain in response to external stimuli or noise may mask any event-related desynchronization/synchronization. This occurs when the EP activity is in the same frequency band as the MRP. The ‘‘Intertrial Variance’’ (IV) method was proposed to solve this problem. In the IV method the variance is calculated by

$$IV_{(j)} = \frac{1}{N-1} \cdot \sum_{i=1}^N \left( x_{f(i,j)} - \bar{x}_{f(j)} \right)^2. \quad (3.19)$$

Where  $N$  is the total number of trials,  $x_{f(i,j)}$  is the  $j$ -th sample of the  $i$ -th trial of the EEG filtered in the required frequency band, and  $\bar{x}_{f(j)}$  is the average of the  $j$ -th sample of the signal over all filtered trials. Likewise, the ERD and ERS are defined as the percentage values of increment or decrement in relation to a reference period. In this case, the reference period is formed by the sample variances of a period preceding the event, and the  $R$  parameter in equation 3.18 is the average of the sample variances in the period.

Bianchi et. al. (1998) analyzed the relations of coherence between EEG signals of nine electrodes (F3, Fz, F4, C3, Cz, C4, P3, Pz and P4) filtered at  $\alpha$  and  $\beta$  bands, and also analyzed the description of the time versus signal frequency of the EEG through an autoregressive (AR) bivariate model. In this study they confirmed the activation flow from the frontal area to the parietal area, through the direct pathway of movement, during the preparation of the movement (Figure 3.25). The ERD/ERS was calculated

from the average of 80 repetitions (epochs) of movement of the index finger of the right hand and activation flow was obtained by analyzing the phase of the Power Spectral Density (PSD).

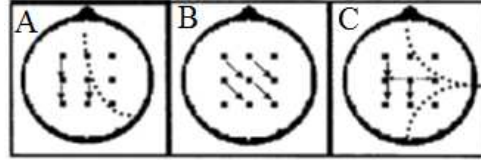


Figure 3.25 – Activation and deactivation flow: (A) programming phase; (B) execution phase; (C) recovery phase (Bianchi, et al., 1995).

It may be noted in Figure 3.25 - A, during the programming phase of the movement, that the activation flow involves only the frontal and parietal lobes of the left brain hemisphere, encompassing electrode F3 to electrode P3. It shows the importance of using electrodes placed not only on the motor cortex, but also on the frontal and parietal lobes.

This Chapter explains the EEG acquisition, the methods for minimizing artifacts, the EEG SNR and the ERD/ERS. The methods for minimizing artifacts are tested and compared in Chapter 5. The EEG SNR and the ERD/ERS scalp maps are also compared during motor mental tasks and music imagery in Chapter 5.

The mental tasks selected to control the BCI should activate different brain areas and the spatial activation pattern measured by the electrodes should be sufficient to distinguish between them. One way to verify the difference between the mental tasks is to calculate the ERD/ERS of all the electrodes and analyze the scalp maps obtained. As the ERD/ERS involves the calculation of averages, the ERD/ERS scalp maps can differ greatly between mental tasks, and even then, be undetectable in real-time by having a low SNR. Therefore the SNR was estimated for all mental tasks and analyzed together with the ERD/ERS scalp maps in order to decide the feasibility of using a specific mental task.

## Chapter 4 : The proposed BCI

As the BCI applications and general processes were mentioned in the introduction, this chapter will focus on the practical features that compose a BCI. The BCIs are platforms that can be understood as the integration of two main processes: the signal acquisition and the signal processing (Figure 1.1). Regarding the signal acquisition, this chapter first presents the techniques for estimating the parameters for online processing and classification, such as the sampling rate and size of the EEG time windows. The feature extraction method and the chosen classifier require that the signal is at least Wide Sense Stationary (WSS), therefore, two statistical hypothesis tests are presented, which completes the first objective mentioned in Chapter 1.

Regarding the signal processing stage, the feature extraction method is described and then, three possible methods for feature selection are presented. The feature selection adapts the classifier training step to a non-supervised approach, which is independent of the chosen mental task paradigm and it is the second objective mentioned in Chapter 1. Then, the classifier is presented and the signal reclassification is discussed. All techniques were initially tested on an EEG database available on the internet (Millán, 2004) and simulated using the platform MATLAB<sup>®</sup>7.11.0 (R2010b) on a computer with an Intel<sup>®</sup> Core<sup>™</sup> i7 processor with a clock speed of 2.10 GHz, Random-Access Memory (RAM) of 8 GB and Hard Disk Drive (HDD) of 1 TB.

### 4.1 EEG Database

The EEG dataset was obtained from the BCI Competition III website. Dataset V was provided by the IDIAP Research Institute (Switzerland) (Millán, 2004). Dataset V contains EEG signals from three normal subjects during three labeled sections (each 4 minutes long) without feedback. In each section, the subject performed three mental tasks (in random order) for about 15-20 seconds, resulting in approximately 16 repetitions of each mental task. The mental tasks consisted of repetitive self-paced left or right hand movement imagery (respectively labeled 2 and 3), and the thought of words beginning with a given random letter (label 7). EEG signals were recorded with a biopotential measurement system (ActiveTwo, Biosemi, the Netherlands) using a cap with 32 integrated electrodes located at standard positions of the International 10-10

system (Fp1, AF3, F7, F3, FC1, FC5, T7, C3, CP1, CP5, P7, P3, Pz, PO3, O1, Oz, O2, PO4, P4, P8, CP6, CP2, C4, T8, FC6, FC2, F4, F8, AF4, Fp2, Fz, Cz). The sampling rate was 512 Hz. Signals were acquired at full DC. No artifact rejection or correction was employed and the EEG records were not subdivided into epochs.

Figure 4.1 shows the EEG of the first session of each subject in the black line, which is related to the left axis. The label (2, 3 or 7) of the continuous recorded mental tasks is shown in the gray superimposed line and it is related to the right axis. The left part of the figure shows the raw EEG, and the right part shows the EEG band pass filtered from 1 to 32 Hz and preprocessed by the CAR method. It can be seen that the raw EEG has a DC component around 6 mV for the first session of subjects 1 and 2 and around 2.5 mV for the first session of subject 3. In the right part of this figure it can be seen that the processed EEG has an amplitude of a few tens of microvolts, as mentioned in section 2.6.

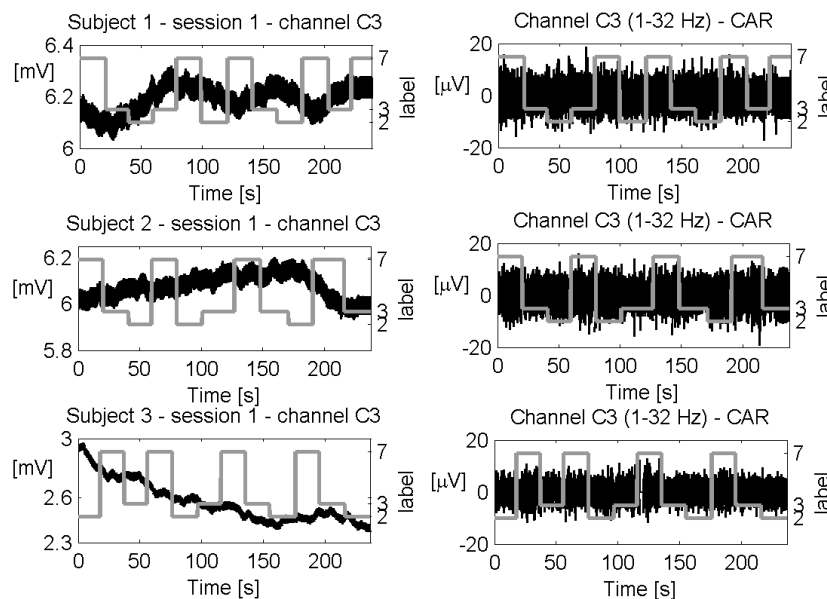


Figure 4.1 – Left: raw EEG of channel C3 from the first section of each subject; Right: EEG band pass filtered from 1 to 32 Hz and preprocessed by the CAR method.

## 4.2 Pseudo-online method

The EEG from the dataset was acquired with monoauricular reference on the right earlobe and the grounding electrode was positioned on the user's forehead. For all tests, the EEG was filtered by using a notch filter combination set to 50, 100, 150, 200 and 250 Hz, in order to reduce the grid line artifact of the European system and its

harmonics. Procedures of spatial filtering were applied to the raw EEG signals to reduce the correlation between channels caused by the spreading of the signal from the cortical source to the scalp. The EEG was spatially filtered by using CAR or large Laplacian methods (see section 3.5).

Small time windows of EEG with a fixed number of samples,  $s$ , were taken to simulate real-time classification, that is the pseudo-online method (Benevides, et al., 2010a-b). The time windows were continuously displaced by a sample (the sliding window technique). Thus, after the first time window was filled, each following window was generated by displacing the current window by one sample, preserving an overlap of  $s-1$  samples. The BCI classification rate is equal to the sampling rate. Regarding the pseudo-online classification, the autocorrelation function (ACF) is performed to determine if the signal is oversampled or subsampled. If the sampling period,  $T_S$ , is too small, the data would be much more highly correlated, which is called the redundancy problem. On the other hand, if  $T_S$  is very large, the data may not have any correlation, which is called the problem of irrelevance. The sampling period,  $T_S$ , can be chosen by the following heuristic rule (Aguirre, 1995),

$$\frac{\tau_m}{20} \leq T_S \leq \frac{\tau_m}{10}. \quad (4.1)$$

In eq. 4.1 above  $\tau_m$  is the time instant of the ACF first minimum. The ACF was performed with time windows of 1 s with a 75% overlap for the EEG signals of all electrodes and sessions of the three subjects. The ACF was averaged and smoothed over all obtained time windows and channels. The left part of Figure 4.2 shows the ACF of each subject obtained by using the CAR method, and the right part of Figure 4.2 shows the ACF obtained by using the large Laplace method. Both curves are very similar and they present the first minimum obtained for channel Cz for a delay of 0,23 s ( $\tau_m = 0,23$ ) (Benevides et al., 2011a).

Then, substituting  $\tau_m$  in eq. 4.1,  $0.011 \text{ s} \leq T_S \leq 0.023 \text{ s}$ , or  $44.524 \text{ Hz} \leq F_S \leq 89.2857 \text{ Hz}$ . As a result, the signal was re-sampled at 64 Hz, which corresponds to a three-step decimation.

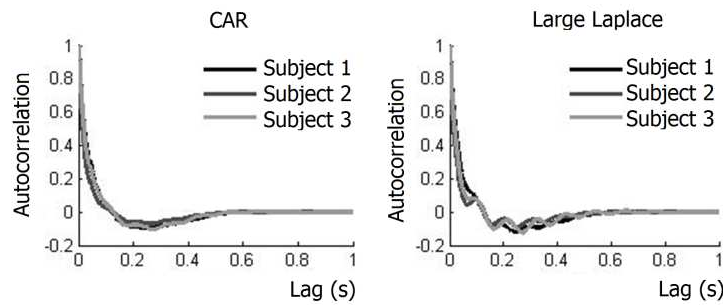


Figure 4.2 – Left: averaged ACF obtained by using CAR method; Right: averaged ACF obtained by using the large Laplace.

### 4.3 Feature extraction

The features used for identification of classes, which in this case are the different mental tasks, are the frequency components of the EEG estimated by the Power Spectral Density (PSD). The PSD choice was motivated by a previous study performed by the author during undergraduate (Benevides, 2007) and graduate (Benevides, 2009) courses. The PSD coefficients, the energy and entropy of the coefficients of the Wavelet Transform and the mean, variance and high order moments of the EEG in the time-domain were tested as possible features. In conclusion the PSD coefficients associated with several classifiers, as simple as decision tree learning and Bayesian Classifiers up to artificial neural networks, obtained results statistically similar. These results will not be replicated in this thesis, but following the findings of this previous work, the PSD coefficients were chosen as the features for the distinction of several mental classes.

The PSD of the filtered EEG signals was calculated without averaging in each 5 s time window of the sliding window technique. The PSD is the Fourier transform of the ACF of a signal if it can be considered wide-sense stationary. It describes how the signal power (defined as the squared value of the signal) is distributed in terms of frequency. Since the EEG signal was resampled to 64 Hz, the signal maximum frequency is 32 Hz. The PSD calculations were performed with rectangular windows and designed to return one coefficient for each integer value of frequency, resulting in 32 coefficients, excluding the DC component. Then, 32 channels and 32 frequency components were used, resulting in 1024 features that are concatenated into a vector (Benevides, et al., 2011c).

To analyze the PSD in the feature space, data was clustered in each class, to get a low-dimensional representation. The k-means algorithm was used to cluster the data,

with 10 centroids per class. Then, Sammon mapping was performed for low-dimensional visualization (Sammon, 1969). Thus, the original feature space with 1024 dimensions is represented two-dimensionally in Figure 4.3. This figure shows the feature space of the training data for subject 1 of dataset V, who obtained the best discrimination between classes. Figure 4.3 - A shows the feature space of the filtered EEG signals in the time domain. The features are the EEG amplitudes of each channel concatenated into a vector. Figure 4.3 - B shows the PSD feature space using all PSD components, and Figure 4.3 - C shows the feature space for some selected PSD components ( $\xi = 50\%$ ). In the feature space a better distribution of classes is observed when frequency components are used rather than the temporal series (Benevides et al., 2011b-c).

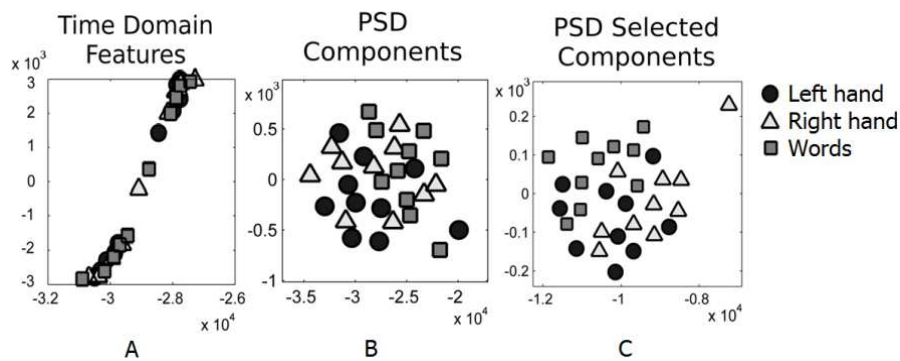


Figure 4.3 – Low-dimensional visualization of the feature space; left: Sammon map of EEG signals in the time domain; center: Sammon map of PSD using all frequency components; right: Sammon map of PSD using selected frequency components ( $\xi = 50\%$ ).

Figure 4.3 - A shows that time domain features mix and overlap in the feature space. It is thus very difficult for the classifier to define regions for each mental task. Figure 4.3 - B shows that PSD components have a small tendency to occupy distinct regions of the feature space, in which the task of thinking of words is mostly at the left region of the figure, considering the center as the center of mass of the features ( $x = -3.2$  and  $y = -0.2 \cdot 10^3$ ). The classifier can thus define rough regions for each mental task. Figure 4.3 - C shows that using some selected components of the PSD, the mental tasks are in mostly distinct regions of the feature space. Using only these components, the classifier can more precisely define the regions for each mental task. These figures show a progressive improvement in class separation, which affects classifier performance and therefore, the BCI reliability.

#### 4.4 EEG stationarity

Some random processes have the property of stationarity which means that the nature of the randomness in the process does not change with time. However, the property of non-stationarity means that characteristics such as the mean,  $\mu$ , the variance,  $\sigma^2$ , or power spectra will change with time (Garcia, 1994). Because of this, the EEG time-windows used to calculate the PSD and also to estimate the mean and variance for the Bayesian classifier have to be at least Wide-Sense Stationary (WSS). If very small time-windows are used, the random nature of EEG will prevail and different values of  $\mu$  and  $\sigma^2$  will be obtained for each new window analyzed. On the other hand, large EEG time-windows are avoided in real-time classification because it may result in large delays during the identification of class transitions. The minimum size of the time-windows in which the EEG can be considered stationary is estimated by using two statistical hypothesis tests. Finally, the size of the time windows used in the sliding window technique will be an interval in which the EEG can be considered stationary.

A time series of  $k$  discrete random variables  $\{x_1, x_2, \dots, x_k\}$  obtained by sampling the random process  $x = x(t, \zeta)$  at the times  $t_1, t_2, \dots, t_k$  is stationary if the joint probability distribution function of any set of samples does not depend on the placement of the time origin. Where  $\zeta$  represents the outcomes from some sample space. Then, for all time shifts  $\tau$ , all  $k$ , and all choices of sample times  $(t_1, t_2, \dots, t_k)$   $f_{x(t)}(x) = f_{x(t+\tau)}(x) = f_x(x)$ . This means that the joint PDF depends only on the time differences  $|t_1 - t_2|$  (Garcia, 1994). Several studies that applied statistical tests of stationarity to EEG reported a variety of results, in which the EEG can be considered stationary from some seconds to several minutes (Blanco et al., 1995).

For an EEG signal strict stationarity is almost impossible to achieve, therefore, a less restrictive requirement called “weak stationarity” or Wide-Sense Stationarity of order  $n$  is used. To obtain a WSS of order  $n$  only the moments up to order  $n$  are constant and independent of time. If the signal has a Gaussian PDF it can be completely defined by the first two cumulants  $K_1$  and  $K_2$ , that are equal to the expected value  $\mu$  and variance  $\sigma^2$  (section 4.6.2). In this case, second order stationarity ( $n = 2$ ) is enough to assure complete stationarity (Garcia, 1994).

Figure 4.4 shows the ongoing average,  $\mu$ , and standard deviation,  $\sigma$ , calculated for every new sample of channel C3, during the first session of subject one. It can be noticed that when ranging from a few samples the values of  $\mu$  and  $\sigma$  tend to vary, i. e.,



for small time-windows, the random nature of the EEG prevails. However, using larger time-windows, the random nature of EEG is approximately canceled and the values of  $\mu$  and  $\sigma$  tend to a constant. The left part of Figure 4.4 shows the ongoing average and standard deviation from time-windows up to 10 seconds and it can be noticed that the values of  $\mu$  and  $\sigma$  tend to stabilize from 5 s onwards. The right part of Figure 4.4 shows the ongoing average and standard deviation from time-windows lasting up to 240 s and it can be noticed that the values of  $\mu$  and  $\sigma$  remain approximately constant until the end of the data. Then, Figure 4.4 shows that small time-windows of an EEG can be non-stationary as  $\mu$  and  $\sigma$  became unstable.

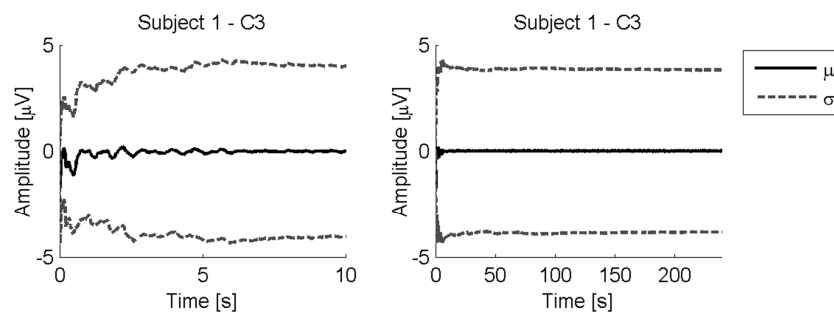


Figure 4.4 – Left: The ongoing average  $\mu$  and standard deviation  $\sigma$  calculated with time-windows up to 10 s; Right: The ongoing average  $\mu$  and standard deviation  $\sigma$  calculated with time-windows lasting up to 240 s.

Large EEG time-windows, such as above 10 s, are avoided in real-time classification because it may result in large delays during the identification of class transitions. On the other hand, small EEG time-windows can be non-stationary, in that case, the minimum size of the time-windows in which the EEG can be considered stationary is estimated here by using two statistical hypothesis tests.

These statistical hypothesis tests are based on the attempt to reject an initial hypothesis, called null hypothesis ( $H_0$ ), which typically proposes a general or default position. The rejection of  $H_0$  states an alternative hypothesis ( $H_A$ ). The Kwiatkowski-Phillips-Schmidt-Shin test (KPSS) is used for testing a null hypothesis that an observable time series is trend stationary while Augmented Dickey-Fuller test (ADF) is used for testing a null hypothesis that the signal is a non-stationary unit root process. Then, these two tests may be used together into a confirmatory analysis (Kwiatkowski et al., 1992).

The statistical hypothesis test uses a test statistic  $\tau$  to make decisions about whether to reject the null hypothesis or not. The test statistic is a function of the sample that is considered as a numerical summary of a data-set that reduces the data to one value that can be used for comparative purposes. Then, the distribution of the test statistic under the null hypothesis is derived and the significance level ( $\alpha$ ) is selected. The significance level is a probability threshold below which the null hypothesis is rejected. The observed value of the test statistic  $\tau_{obs}$  is calculated from the data to be analyzed. The p-value of  $\tau_{obs}$  is calculated and the rule is to reject the null hypothesis if and only if the p-value is less than or equal to the significance level.

The left p-value is the quantile of the value of the test statistic, that is the probability of occurrence of values less or equal the observed test statistic,  $P[\tau \leq \tau_{obs}]$ . Figure 4.5 - A shows an example of a test statistic distribution of a unilateral left sided test. Then, the null hypothesis is rejected only if the p-value of  $\tau_{obs}$ , that is the probability of obtaining values less than or equal to  $\tau_{obs}$ , is less than  $\alpha$ . The right-tailed p-value is one minus the quantile, that is the probability of occurrence of values equal to or greater than the observed test statistic,  $1 - P[\tau \geq \tau_{obs}]$ . Figure 4.5 - B shows an example of a test statistic distribution of a unilateral right sided test. The null hypothesis is then rejected only if the p-value of  $\tau_{obs}$ , that is the probability of obtaining values at least as extreme as  $\tau_{obs}$ , is less than  $\alpha$ , while the two-tailed p-value is twice whichever of these is smaller. Figure 4.5 - C shows an example of a test statistic distribution of a two-tailed test.

The KPSS test is used for testing the null hypothesis that an observable time series is trend stationary while the ADF test is used for testing a null hypothesis that the signal is a non-stationary unit root process. If the KPSS null hypothesis is rejected, what states  $H_A$ , and the ADF null hypothesis is not rejected, it can be concluded that the signal is a non-stationary unit root process. If the KPSS null hypothesis is not rejected and the ADF null hypothesis is rejected, it can be concluded that the signal is trend stationary. If the null hypotheses of both tests are rejected or equally if neither is rejected, then, nothing can be concluded. The possible results are summarized in Table 4.1.

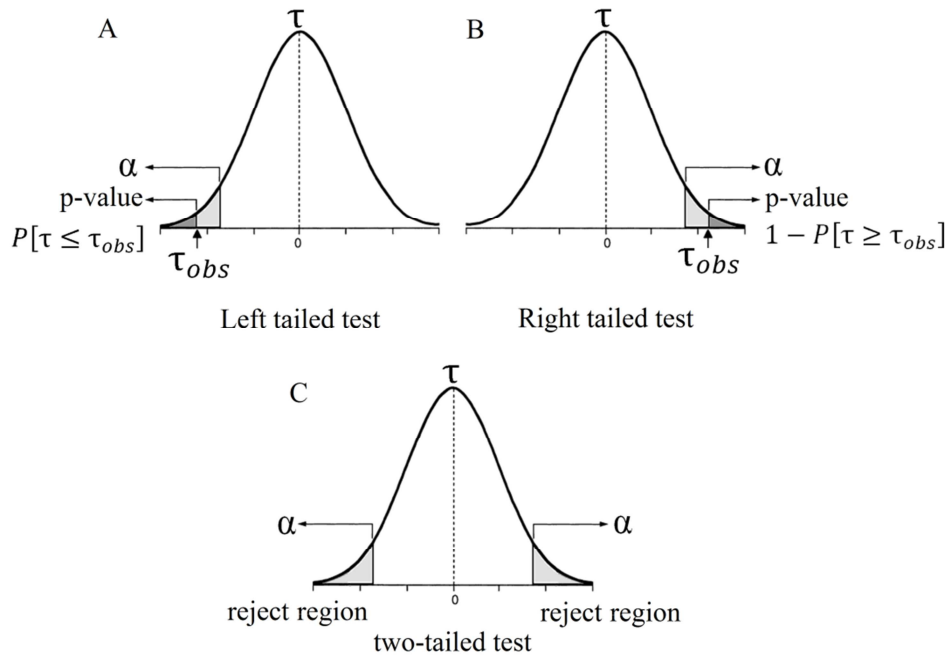


Figure 4.5 – A) left tailed test; B) right tailed test; C) two-tailed test.

Table 4.1 – Confirmatory analysis of KPSS and ADF tests. TSP: Trend Stationary Process; NSURP: Non Stationary Unit-Root Process.

		KPSS	
		$H_0$	$H_A$
ADF	$H_0$	?	NSURP
	$H_A$	TSP	?

The KPSS test is used for testing the null hypothesis that an observable time series is trend stationary<sup>39</sup>. In a trend stationary process the stochastic part of the process is stationary. The KPSS test assumes that the signal is the sum of a deterministic trend, a random walk, and a stationary error,

$$x(t) = \delta(t) + e(t) + \xi(t), \quad t = 1, 2, \dots, T. \quad (4.2)$$

Where  $T$  is the sample size,  $\delta(t)$  corresponds to the deterministic trend,  $e(t)$  is the stationary part of the process and  $\xi(t)$  is a random walk, i. e.,  $\xi(t) = \xi(t-1) + v(t)$ .  $v(t)$  is assumed to be an independent and identically distributed (i.i.d.)<sup>40</sup> zero-

<sup>39</sup> Stationary around a deterministic trend.

<sup>40</sup> A sequence of random variables is i.i.d. if each random variable has the same probability distribution as the others and all are mutually independent. That is, the occurrence of one event does not affect the probability of the other and their covariance is zero.

mean random variable with variance,  $\sigma_v^2$ . If the variance of the random walk is zero,  $\sigma_v^2 = 0$ , then,  $\xi(t) = \xi(0)$  for all  $t$  and  $x(t)$  is stationary. The ordinary least squares (OLS), or linear least squares regression of,  $x(t)$  gives the estimated trend of  $x(t)$ :

$$y(t) = a + b \cdot x(t) + e(t). \quad (4.3)$$

where  $a$  is the constant parameter,  $b$  is the variable coefficient and  $e(t)$  are the residuals from the OLS regression. The residuals obtained from the OLS regression are related to the random walk. The KPSS test is a unilateral right sided test based on,  $H_0: \sigma_v^2 = 0$  against  $H_A: \sigma_v^2 > 0$  (Kwiatkowski et al., 1992). The test statistic of the KPSS is an estimation of the random walk variance that is given by

$$\tau_{KPSS} = \frac{1}{T^2 \cdot \widehat{\Omega}_e} \cdot \sum_{t=1}^T \left( \sum_{s=1}^t e(s) \right)^2. \quad (4.4)$$

where  $\widehat{\Omega}_e$  is the long-run variance of  $e(t)$  calculated by using the Newey-West Heteroscedastic<sup>41</sup> and Autocorrelation Consistent (HAC) estimator (Kwiatkowski et al., 1992). The long-run variance is given by

$$\Omega = \sum_{j=-\infty}^{\infty} \gamma_x(j). \quad (4.5)$$

where  $\gamma_x(j)$  denotes the  $j$ -th lagged autocovariance of  $x$ ,  $\gamma_x(j) = E[(x(t) - E[x(t)]) \cdot (x(t-j) - E[x(t-j)])]$  (Kwiatkowski et al., 1992). The Newey-West HAC estimator for  $\Omega$  is given by,

$$\widehat{\Omega} = \widehat{\gamma}_x(0) + 2 \sum_{j=1}^{l_{max}} w(j, m) \cdot \widehat{\gamma}_x(j),$$

---

<sup>41</sup> Heteroscedasticity is the absence of homoscedasticity. A collection of random variables is heteroscedastic if there are sub-populations that have different variances, covariances, or any other measure of statistical dispersion from others. The possible existence of heteroscedasticity is a major concern in the application of regression analysis.

$$\hat{\gamma}_x(j) = \frac{1}{T} \cdot \sum_{t=j+1}^T (x(t) - \bar{x}_T) \cdot (x(t-j) - \bar{x}_T) \quad \text{and} \quad \bar{x}_T = \frac{1}{T} \cdot \sum_{t=1}^T x(t). \quad (4.6)$$

In the Newey-West formula the lagged autocovariance,  $\hat{\gamma}_x(j)$ , is weighted by the Bartlett Kernel,  $w(j, m) = 1 - [j/(m + 1)]$  for  $j \leq m$  and  $w(j, m) = 0$  otherwise, to ensure a positive semi-definite covariance matrix (Datta & Du, 2012). In this research, the maximum number of lags of  $\hat{\Omega}$ ,  $l_{max}$ , was calculated as recommended by Kwiatkowski et al. (1992) in which  $l_{max}$  is the nearest integer value of the square root of the sample size  $T$ ,  $l_{max} = \text{int}\{\sqrt{T}\}$ . Where the operator  $\text{int}\{\cdot\}$  is the nearest integer value of a real number.

From the sampling distribution of the KPSS test statistic, given by the normal  $N(\mu, \hat{\Omega})^{42}$ , the KPSS p-value can be obtained by  $1 - P[\tau_{KPSS} \geq \tau_{obs}]$ . Then, since KPSS is a right tailed test, the null hypothesis is rejected and the sequence is considered not trend stationary if the p-value is less than  $\alpha$ .

The ADF test is used for testing the null hypothesis that the signal is a non-stationary unit root process<sup>43</sup>. The ADF test assumes that the signal is a stochastic process modeled by an Autoregressive Model (AR). The AR model specifies that the output variable depends linearly on its own previous values. By including lags of the order  $p$  the ADF formulation allows for higher-order autoregressive processes. This means that the lag length  $p$  has to be determined when applying the test. One possible approach is to begin with a maximum lag, such as the one recommended by Schwert (1989), and then test down by assessing the significance of the coefficient of the largest lagged change in  $x(t)$ . The notation  $\text{AR}(p)$  indicates an autoregressive model of order  $p$  and the model is defined as

$$x(t) = c + \sum_{i=1}^p \varphi_i + x(t-i) + \varepsilon(t). \quad (4.7)$$

---

<sup>42</sup> Normal distribution:  $N(\mu, \sigma^2) = (1/\sqrt{2\pi \cdot \sigma}) \cdot e^{-(x-\mu)^2/2 \cdot \sigma}$ .

<sup>43</sup> Characteristic equations are differential algebraic equations used to model the time series of a stochastic process. If the characteristic equation has a unique unit root, then, the stochastic process is non-stationary, integrated of order one,  $I(1)$ , and the first difference of the process will be stationary. If the characteristic equation has  $r$  multiples of unit roots, then, the stochastic process is integrated of order  $r$ ,  $I(r)$ .

Where,  $\varphi_i$  are the parameters of the model,  $c$  is a constant value and  $\varepsilon(t)$  is white noise<sup>44</sup>. In this research, the maximum lag was calculated as recommended by (Schwert, 1989) in which for small sample sizes ( $T < 250$ ) the maximum lag is given by  $l_4$ ,

$$p = l_4 = \text{int}\{4(T/100)^{1/4}\}. \quad (4.8)$$

For large sample sizes ( $T \geq 250$ ) the maximum lag is given by  $l_{12}$ ,

$$p = l_{12} = \text{int}\{12(T/100)^{1/4}\}. \quad (4.9)$$

Some constraints are necessary on the values of the parameters of this model in order that the model remains wide-sense stationary. For example, processes in the AR(1) model,  $x(t) = c + \varphi_1 + x(t - 1) + \varepsilon(t)$ , with  $|\varphi_1| \geq 1$  are not stationary. More generally, for an AR( $p$ ) model to be wide-sense stationary, the roots of the polynomial  $z^p - \sum_{i=1}^p \varphi_i \cdot z^{p-i}$  must lie within the unit circle, i. e., each root  $z_i$  must satisfy  $|z_i| < 1$ . The Dickey-Fuller tests whether a unit root is present in an autoregressive model. Considering the AR(1) model, the unit root hypothesis corresponds to  $H_0: \varphi_1 = 0$  against  $H_A: \varphi_1 < 1$  (Schwert, 1989). Alternatively, the model can be formulated as

$$\nabla x(t) = (\varphi_1 - 1) \cdot x(t - 1) + \varepsilon(t) = \delta \cdot x(t - 1) + \varepsilon(t). \quad (4.10)$$

Where  $\nabla$  is the first difference operator. This model can be estimated and tested for a unit root and it is equivalent to testing  $\delta = 0$  (where  $\delta = \varphi_1 - 1$ ). Then, the unit root hypothesis translates into  $H_0: \delta = 0$  against  $H_A: \delta < 0$ , which is a left tailed test. The statistic of the DF test is given by

$$\tau_{DF} = \frac{(\widehat{\varphi}_1 - 1)}{SE(\widehat{\varphi}_1)} = \frac{\hat{\delta}}{SE(\widehat{\varphi}_1)}. \quad (4.11)$$

Where the  $SE$  denotes the standard errors of the least squares estimators. The statistic  $\tau_{DF}$  has a specific non-Gaussian distribution simply known as the Dickey–

---

<sup>44</sup> White noise is a random signal whose samples are regarded as a sequence of serially uncorrelated random variables with zero mean and finite variance.

Fuller table. Once a value for the test statistic is computed it can be compared with the critical values interpolated from the table for a specific significance level. If the test statistic is less than the larger negative critical value, then the null hypothesis of  $\gamma = 0$  is rejected and no unit root is present. The ADF test is an extended version of the DF test to an  $AR(p)$  model.

Here, a significance level of 5% was used ( $\alpha=0.05$ ) and all tests were applied with time windows from 0.1 to 5 s for all channels and subjects. Figure 4.6 shows the results of the tests taking the average result of all channels and sessions of each subject. For all subjects, the p-value of the KPSS was higher than  $\alpha$  for all lengths of the time windows tested. Therefore, the null hypothesis that the signal is stationary can not be rejected. For subject 1 the p-value of the ADF is lower than  $\alpha$  for time windows larger than 1.1 s indicating that for these time windows the null hypothesis that the signal is a non-stationary unit root process can be rejected. For subject 2 the p-value of the ADF is lower than  $\alpha$  for time windows larger than 0.7 s and, for subject 3, the p-value of the ADF is lower than  $\alpha$  for time windows larger than 1.3 s. By using the confirmatory analysis of the KPSS and ADF tests shown in table 4.1, in the worst case the EEG signal can be considered stationary for windows larger than 1.3 s, which corresponds to approximately 84 samples, as the EEG signal was re-sampled to 64 Hz. The nearest power of two higher than 84 samples corresponds to 128 samples, therefore, time-windows of 2 s were adopted. In Figure 4.6 the non-stationary intervals are highlighted by the shaded area. In conclusion to this analysis, time-windows of 2 s were adopted for further processing with the EEG from the dataset in order to perform the pseudo-online classification.

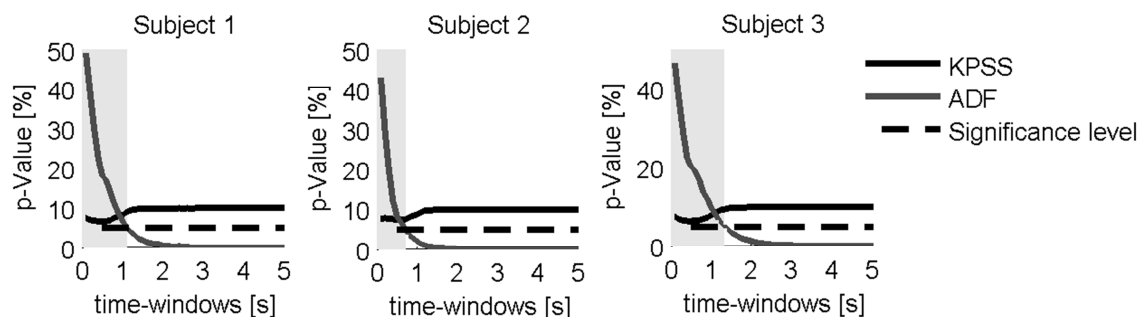


Figure 4.6 – Application of KPSS and ADF tests for each subject.

#### 4.5 Feature Selection

The aim of the feature selection procedure is to maximize the distinction between classes (mental tasks) to increase the classification success rate. The PSD coefficients are the input features of the classifier. The histograms of each frequency of the PSD were calculated for each EEG channel, resulting in  $32 \times 32$  histograms for each class, discarding the DC component. Then, a measure of the discrimination between classes,  $D$ , was used to compare the differences between the histograms of each class for the same frequency and channel. Figure 4.7 shows the channel  $\times$  frequency matrix, where each cell has the value of the discriminant,  $D_{i,j}$ , calculated from the histogram of each class ( $C_1$ ,  $C_2$  and  $C_3$ ) (Benevides et al., 2011d).

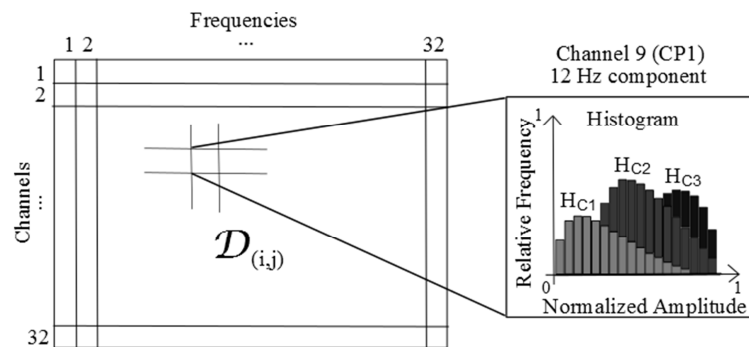


Figure 4.7 – Channel  $\times$  frequency matrix.  $H_{C1}$ ,  $H_{C2}$  and  $H_{C3}$  are the histograms of the respective classes  $C_1$ ,  $C_2$  and  $C_3$ .

Three methods for estimating the differences between the histograms were compared, which were the Discriminative Power (DP), the Mean Squared Error (MSE) between the histograms and the Kullback-Leibler (K-L) symmetric divergence (see footnote 35).

The DP method uses only the extreme values of the histograms and it measures the overlap of histograms without worrying about its shape. Therefore, it is not necessary to calculate the histogram, but only the maximum and minimum values of the measured variables (Gonzalez et al., 2006). Suppose that a variable, e. g. the 12 Hz frequency of channel C3, has been repeatedly observed during two different conditions, which are the mental tasks  $C_1$  and  $C_2$ . Then,  $a$  is the vector containing the set of values corresponding to the condition  $C_1$ , and  $b$  is the vector containing the set of values corresponding to the condition  $C_2$ . In the best case, if the maximum value of  $a$ ,  $max(a)$ , is smaller than the minimum value of  $b$ ,  $min(b)$ , then, there is no overlap between the



histograms and the value of DP is 1 (Figure 4.8 - Left). In the worst case, if the minimum value of  $a$  is greater than the minimum value of  $b$  and the maximum value of  $a$  is smaller than the maximum value of  $b$ , then, the histogram of  $a$  is fully contained in the interval of the histogram of  $b$ , the overlap between the histograms is complete and the value of DP is 0 (Figure 4.8 - Right).

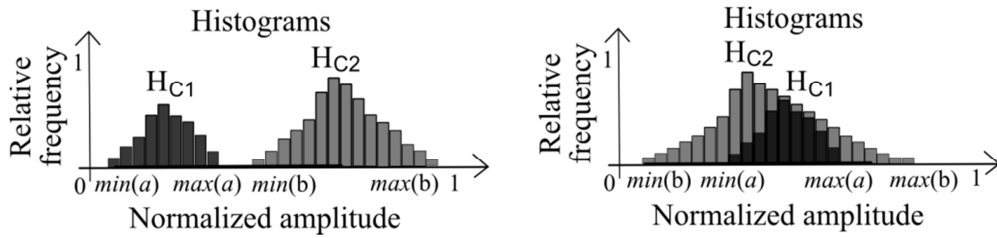


Figure 4.8 – Discriminative Power. Left: Histograms without overlap (DP = 1); Right: Histograms with complete overlap (DP = 0).

The calculation of the DP is given by,

$$DP = \frac{\text{card}\{a < \min(b)\} + \text{card}\{b > \max(a)\}}{\text{card}\{a\} + \text{card}\{b\}}, \quad (4.12)$$

where  $\text{card}\{.\}$ , from cardinality, is the number of elements in a set. The resultant discriminant measure for the three histograms is the sum of the contribution of each possible combination between pairs of histograms, which is given by

$$D_{i,j} = DP_{i,j}(C_1, C_2) + DP_{i,j}(C_1, C_3) + DP_{i,j}(C_2, C_3), \quad (4.13)$$

where the indexes  $i, j$  correspond to the channels  $i$  and frequencies  $j$  of the discriminant matrix. The left part of Figure 4.9 shows the discriminant matrix  $\mathbf{D}$  calculated for subject 1, whose discriminant values are represented in the color scale on the right side of the figure. The highest discrimination values were obtained for tuples (FC1 at 1, 3 and 10 Hz), (C4, P4 and CP2 at 9 Hz), (CP1 at 10 and 19Hz), (CP6 at 10 and 20 Hz), (P3 at 18 Hz) and (O2 at 10 Hz). Excluding channel O2, all other channels highlighted above are positioned approximately over the motor cortex. Most of frequency components associated with these channels belong to  $\mu$  or  $\beta$  bands, which is in accordance with the foreknowledge that motor mental tasks affect  $\mu$  and  $\beta$  bands over the contralateral motor cortex. The right part of Figure 4.9 shows in grayscale the total

contribution of each channel and its relative importance to the discrimination of classes, in which white corresponds to a maximum contribution and black to a negligible contribution. The total contribution of each channel is calculated by summing up the contribution of all the frequencies of the channel.

It can be observed that Fp1, Fc1 and C4 are considered the most important channels and that the occipital area is less important for the discrimination between mental tasks, which is consistent with theory since visual tasks or visual mental tasks are not being performed. However, the contribution of the channel Fp1 is uncertain because its location is greatly affected by blinking and eye movement artifacts.

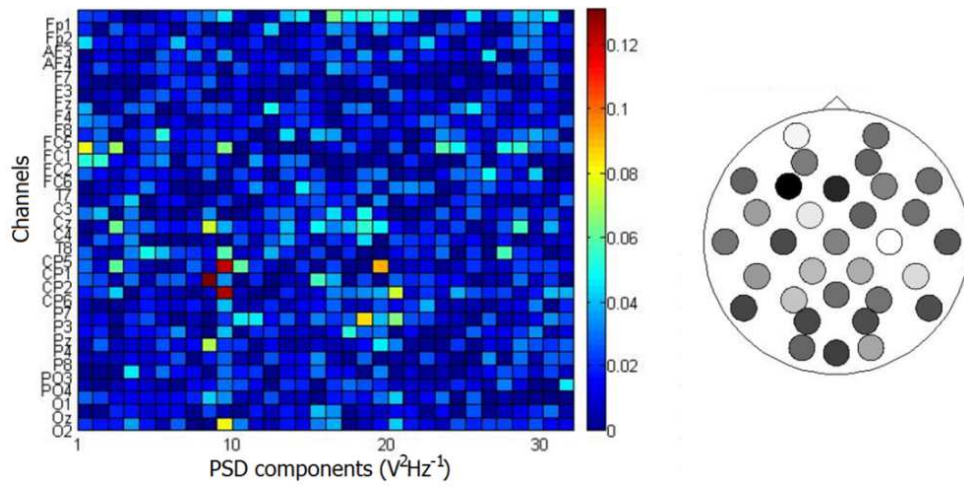


Figure 4.9 – Left: Discriminant Matrix  $\mathbf{D}$  of subject 1 obtained with DP method; Right: Total contribution of each channel in relation to the discrimination between the classes.

The mean squared error is a discriminant measure between the three histograms of each class for the same frequency and channel. The resultant discriminant measure for the three histograms is the sum of the contribution of each possible combination between pairs of histograms, which is given by

$$\mathbf{D}_{i,j} = \mathbf{MSE}_{i,j}(\mathbf{C}_1, \mathbf{C}_2) + \mathbf{MSE}_{i,j}(\mathbf{C}_1, \mathbf{C}_3) + \mathbf{MSE}_{i,j}(\mathbf{C}_2, \mathbf{C}_3) . \quad (4.14)$$

The left part of Figure 4.10 shows the discriminant matrix  $\mathbf{D}$  obtained with MSE method for subject 1. The highest discrimination values were obtained for tuples (F3, Fc1 and C3 at 10 Hz) and (Cp1 at 9 and 10 Hz). All channels highlighted above are positioned approximately over the motor cortex and all frequency components related to these channels belong to  $\mu$  or  $\beta$  bands. The right part of Figure 4.10 shows in grayscale

the total contribution of each channel by summing up the contribution of all frequencies of the channel. It can be noted that the channels with higher contribution are over the frontal, central, central-parietal and temporal cortex.

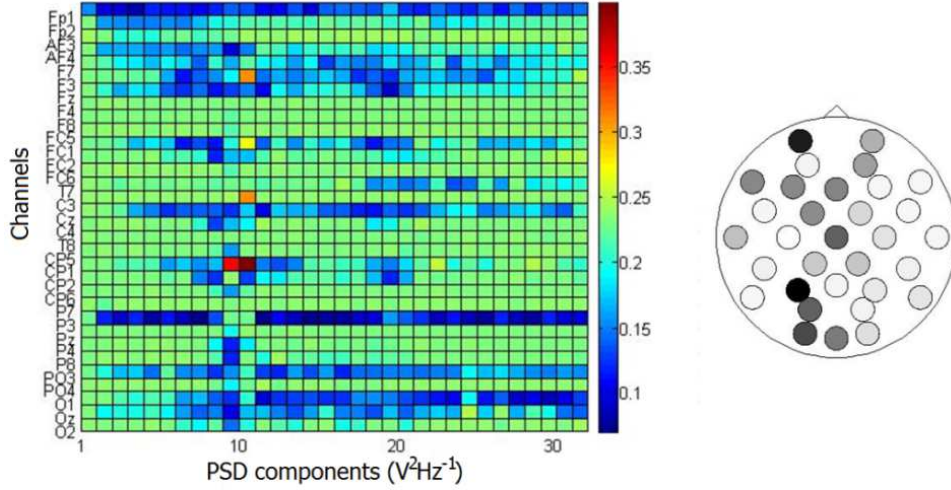


Figure 4.10 – Left: Discriminant Matrix  $D$  of subject 1 obtained with DP method; Right: Total contribution of each channel in relation to the discrimination between the classes.

The K-L symmetric divergence was also used as a discrimination measure between the histograms. The K-L divergence between the classes  $C_1$  and  $C_2$ ,  $D_{KL}(C_1||C_2)$ , is given by

$$D_{KL}(C_1||C_2) = \sum_{i=1}^k H_1(i) \ln \left( \frac{\max(H_1(i), \delta)}{\max(H_2(i), \delta)} \right). \quad (4.15)$$

Where  $H_1$  e  $H_2$  are the histograms of  $C_1$  e  $C_2$ , discretized with  $k$  bins and  $\delta$  is a small constant used to prevent the logarithm, or the division, of zero (Benevides et al., 2011e). Here,  $\delta$  was empirically taken as 0.001. The number of bins  $k$  of the histogram can be assigned by the Sturge's rule,

$$k' = 1 + \log_2 n. \quad (4.16)$$

Where  $n$  is the number of samples, and then  $k$  is given by the nearest integer above  $k'$  (, 1928). Implicit in Sturge's rule is the assumption of a normally distributed data set that is being well approximated by a binomial distribution with probability 0.5,

which gives a symmetric distribution. This is not a problem because, as will be shown in sections 4.6.2, 4.6.3 and 4.7, the EEG signals of this study can be modeled by normal distributions. The symmetric version of K-L divergence,  $SD_{KL}$ , is given by

$$SD_{KL}(\mathbf{C}_1||\mathbf{C}_2) = D_{KL}(\mathbf{C}_1||\mathbf{C}_2) + D_{KL}(\mathbf{C}_2||\mathbf{C}_1). \quad (4.17)$$

In the same way, the resultant discriminant measure for the three histograms is the sum of the contribution of each possible combination between pairs of histograms, which is given by

$$\mathbf{D}_{i,j} = \mathbf{SD}_{KL(i,j)}(\mathbf{C}_1||\mathbf{C}_2) + \mathbf{SD}_{KL(i,j)}(\mathbf{C}_1||\mathbf{C}_3) + \mathbf{SD}_{KL(i,j)}(\mathbf{C}_2||\mathbf{C}_3). \quad (4.18)$$

The left part of Figure 4.11 shows the discriminant matrix  $\mathbf{D}$  obtained with the K-L method for subject 1. Here, all 3 sessions of the sub-sampled EEG of subject 1, each one lasting approximately 4 minutes, are used. The PSD is calculated for 2 s time window with the sliding window technique and 15,232 samples are available for each class. Therefore, the Sturge's rule (eq. 4.16) estimates that  $k' = 14.8948$  and 15 bins are used to calculate the histograms of the K-L method.

The highest discrimination values were obtained for tuples (FP1, AF3, F3, Fz, FC1, FC2, C3, C4, CP2, CP5 and P4 at 9 Hz) and (CP1 at 9 and 10 Hz), clearly highlighting the  $\mu$  rhythm of the motor cortex to the detriment of other frequency components. The right part of Figure 4.11 shows the total contribution of each channel by summing the contribution of all the frequencies of the channel. In contrast to the other two methods tested, it can be seen that the activity highlighted with the K-L method is well focused in frequency components that correspond to the  $\mu$  band. Thus, it having the best adaptation to highlight the expected activity of the  $\mu$  band during the motor mental task was the decisive factor for its choice over the other studied methods.

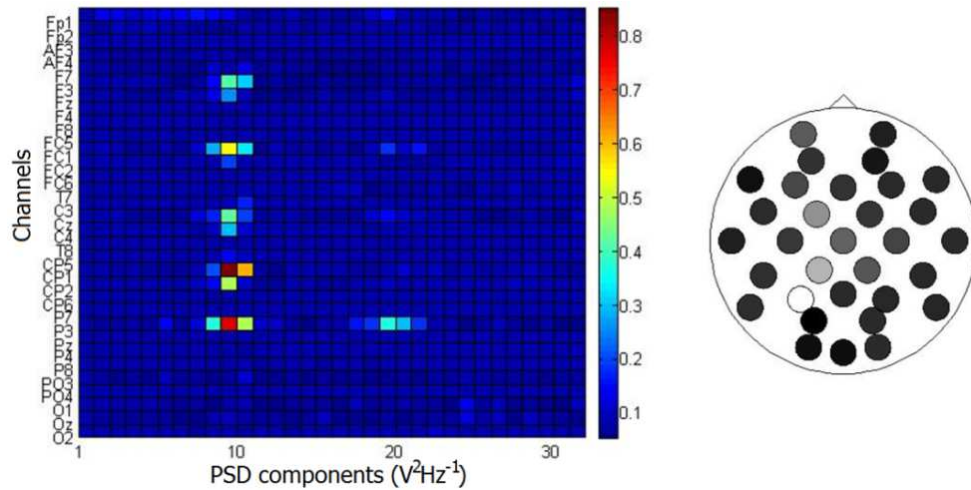


Figure 4.11 – Left: Discriminant Matrix  $\mathbf{D}$  of subject 1 obtained with K-L method; Right: Total contribution of each channel in relation to the discrimination between the classes.

The feature selection can be made by setting a maximum number of features to be used in the classification and selecting those which obtained the highest discriminant values. Another approach of selection would be to use a variable number of features and a threshold analysis, e. g., selecting all the features that obtained discriminant values above 60% of the highest value obtained. The relative percentage of the maximum discriminant value will henceforth be represented by  $\xi$ . Another manner of selection could be by identifying the maximum discriminant value of a channel from an area which we are aware is not related to any of the mental tasks, e. g., the channel Oz. Thus, only features with discriminant values higher than the value found for Oz will be considered important and will be selected. Figure 3.10 shows the selected features by using this last method.

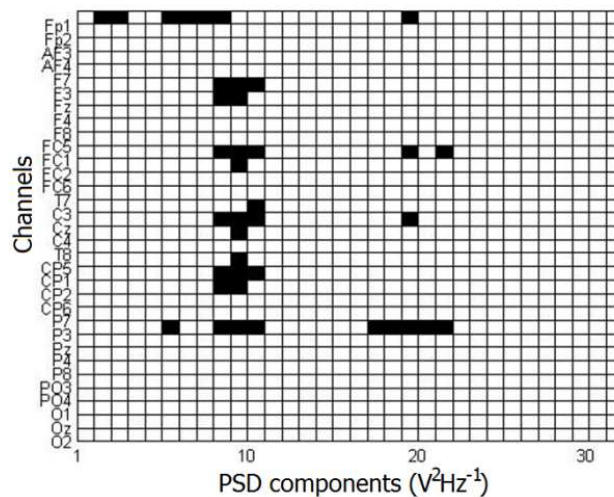


Figure 4.12 – Selection of features with discriminant values higher than Oz maximum discriminant.

## 4.6 Classifier

A Bayesian classifier was used for classification. This choice was motivated by a previous study performed by the author during the undergraduate (Benevides, 2007) and graduate (Benevides, 2009) courses. As previously mentioned, several classifiers were tested together with some feature extraction methods like the PSD, the Wavelet Transform and high order moments of the EEG in the time-domain. The classifiers tested were: the decision tree learning, the Bayesian Classifiers in the case of Linear Discriminant Analysis (LDA), Quadratic Discriminant Analysis (QDA), Regularized Discriminant Analysis (RDA) and a backpropagation artificial neural network (ANN) with the Bayesian regulation backpropagation (trainbr) learning algorithm.

These studies showed that the LDA and the ANN obtained results statistically similar. Then, following these findings, the Bayesian classifier with a linear discriminant function and a normal Probability Density Function (PDF) was chosen for the classification. The LDA was chosen rather than the ANN because its simpler algorithm needs less processing time.

### 4.6.1 Bayesian Classifier

A Bayesian classifier was used for classification. It is a probabilistic approach based on Bayes' rule (eq. 4.19). The Bayes' rule is a conditional probability relating the posteriori probability  $P(\mathbf{C}_k|x)$  of occurrence of the event  $x$  in a class  $\mathbf{C}_k$ , with the priori probability  $P(\mathbf{C}_k)$  of occurrence of a class  $\mathbf{C}_k$  and the probability density function  $P(x|\mathbf{C}_k)$  (Garcia, 1994). In this equation,  $P(x)$  is only a scaling factor, given by the total probability theorem, which ensures that the sum of the posteriori probabilities is equal to 1 (eq. 4.20).

$$P(\mathbf{C}_k|x) = \frac{P(x|\mathbf{C}_k) \cdot P(\mathbf{C}_k)}{P(x)} \quad (4.19)$$

$$P(x) = \sum_{i=1}^L P(x|\mathbf{C}_i) \cdot P(\mathbf{C}_i) \quad (4.20)$$

The sample space  $\mathbf{S}$  is partitioned into  $L$  classes (eq. 4.21), wherein the probability of occurrence of class  $\mathbf{C}_k$  in  $\mathbf{S}$  is its priori probability  $P(\mathbf{C}_k)$ . Let's assume that the sample space has  $N$  samples and each class has  $N_i$  samples. If samples of classes can be considered random, then the priori probability can be estimated by the fraction of each class in  $\mathbf{S}$  (Friedman, 1989). Then, the priori probability of occurrence of a class  $\mathbf{C}_k$  is the fraction of the number of samples  $N_k$  of class  $\mathbf{C}_k$  and the total number of samples in the sample space,  $N$  (eq. 4.22).

$$\mathbf{S} = [\mathbf{C}_1, \mathbf{C}_2, \dots, \mathbf{C}_k, \dots, \mathbf{C}_L] \quad (4.21)$$

$$P(\mathbf{C}_k) = \frac{N_k}{N} \quad (4.22)$$

The feature space can contain more than one feature; being 2-dimensional if it has 2 features, or 3-dimensional if it has 3 features. For the general case, in which  $\mathbf{S}$  has  $d$  features,  $\mathbf{S}$  will be a multidimensional space with  $d$  dimensions, i. e., a hyperspace. Then, each class  $\mathbf{C}_i$  ( $i = 1, 2, \dots, L$ ) has  $d$  features that were observed, or sampled,  $N_i$  times. Then, the classes are represented by matrices in which the rows are the features, or  $\mathbf{S}$  dimensions, and the columns are the observations,  $y$ , of each feature (eq. 4.23).

$$\mathbf{C}_1 = \begin{bmatrix} y_{1,1} & \dots & y_{1,N_1} \\ \vdots & \ddots & \vdots \\ y_{d,1} & \dots & y_{d,N_1} \end{bmatrix}, \mathbf{C}_2 = \begin{bmatrix} y_{1,1} & \dots & y_{1,N_2} \\ \vdots & \ddots & \vdots \\ y_{d,1} & \dots & y_{d,N_2} \end{bmatrix}, \dots, \mathbf{C}_L = \begin{bmatrix} y_{1,1} & \dots & y_{1,N_L} \\ \vdots & \ddots & \vdots \\ y_{d,1} & \dots & y_{d,N_L} \end{bmatrix} \quad (4.23)$$

Let's consider an observed event  $\mathbf{x}$  of unknown class. The event  $\mathbf{x}$  is a vector of random variables, with length  $d$ , corresponding to an observation of the  $d$  features in  $\mathbf{S}$ . The probability of occurrence of the class  $\mathbf{C}_k$  since the event  $\mathbf{x}$  was observed is the posteriori probability  $P(\mathbf{C}_k|\mathbf{x})$ . From the observation matrices of each class the Probability Density Function (PDF) can be estimated. For the general case, in which the feature space has more than one dimension, joint PDF is estimated. In most cases, the PDF is approximated by a multivariate normal, or Gaussian distribution, given the important statement of the central limit theorem. Bayesian classifiers that utilize the multivariate normal distribution are called normal classifiers and they are a particular case of the Bayesian classification.

### 4.6.2 The normal distribution

The central limit theorem states that the mean of a sufficiently large number of samples of i.i.d. random variables, each described by any PDF but with a well-defined mean and well-defined variance, will be approximately normally distributed (Garcia, 1994). Thus, a variable may have a unique distribution very different from the normal, however, if many samples from this distribution are taken, the histogram shape of the sample means will resemble a normal curve. Therefore, the multivariate normal distribution is commonly used and it is completely defined by its first and second order cumulants,  $k_1$  and  $k_2$  (Fukunaga, 1990). The normal distribution of a random variable  $X$  is given by

$$f_X(x|k_1, k_2) = N_X(k_1, k_2) = \frac{1}{\sqrt{2\pi \cdot k_2}} \cdot e^{-(x-k_1)^2/2 \cdot k_2}. \quad (4.24)$$

The cumulant-generating function of  $X$ ,  $K_X$ , is related to the characteristic function  $\Psi_X$  by

$$K_X(t) = \ln(\Psi_X(t)), \quad (4.25)$$

where the characteristic function is given by

$$\Psi_X(t) = E[e^{i \cdot t \cdot x}] = \int_{-\infty}^{+\infty} e^{i \cdot t \cdot x} \cdot f_X(x) dx, \quad t \in \mathbb{R}, \quad i \in \mathbb{C}, \quad (5.26)$$

where  $i$  is the imaginary unit ( $i = \sqrt{-1}$ ). Then, using the McLaurin series expansion of the exponential function ( $e^{i \cdot x} = 1 + i \cdot x + \frac{1}{2!}(i \cdot x)^2 + \frac{1}{3!}(i \cdot x)^3 + \frac{1}{4!}(i \cdot x)^4 \dots$ ) and substituting it into eq. 4.26, we obtain

$$\begin{aligned} \Psi_X(t) &= E[e^{i \cdot t \cdot X}] = E \left[ 1 + i \cdot t \cdot X + \frac{(i \cdot t \cdot X)^2}{2!} + \frac{(i \cdot t \cdot X)^3}{3!} + \dots \right] = \\ \Psi_X(t) &= E[1] + i \cdot t \cdot E[X] + \frac{i^2 \cdot t^2}{2!} E[X^2] + \frac{i^3 \cdot t^3}{3!} E[X^3] + \dots = \end{aligned}$$



$$\Psi_X(t) = 1 + \sum_{n=1}^{\infty} E[X^n] \cdot \frac{(i \cdot t)^n}{n!}. \quad (4.27)$$

As the cumulant-generating function is the natural logarithm of the characteristic function, the power series expansion of the logarithm function,  $\ln(1 + Z) = \frac{Z}{1} - \frac{Z^2}{2} + \frac{Z^3}{3} - \dots = \sum_{m=1}^{\infty} (-1)^{m+1} \frac{Z^m}{m}$ , can be substituted into eq. 4.25 and, by substituting eq. 4.27 into eq. 4.25 the cumulant-generating function takes the following form:

$$K_X(t) = \sum_{m=1}^{\infty} \frac{(-1)^{m+1}}{m} \cdot \left( \sum_{n=1}^{\infty} E[X^n] \cdot \frac{(i \cdot t)^n}{n!} \right)^m =$$

$$K_X(t) = E[X]it - (E[X^2] - E[X]^2) \frac{t^2}{2!} - (E[X^3] - 3E[X^2]E[X] + 2E[X]^3) i \frac{t^3}{3!} + \dots. \quad (4.28)$$

Then, cumulants can be extracted from eq. 4.28 by successive differentiation in  $K_X(t)$  equal to zero. That is, the  $K_n$  cumulants are the McLaurin Series coefficients of  $K_X(t)$ , ignoring the imaginary component. The first four cumulants are given by

$$K_1 = K_X^I(0) = E[X] \text{ (expected value)}$$

$$K_2 = K_X^{II}(0) = E[X^2] - E[X]^2 = \sigma^2 \text{ (variance)}$$

$$K_3 = K_X^{III}(0) = E[X^3] - 3E[X^2]E[X] + 2E[X]^3$$

$$K_4 = K_X^{IV}(0) = E[X^4] - 4E[X^3]E[X] - 3E[X^2]^2 + 12E[X^2]E[X]^2 - 6E[X]^4. \quad (4.29)$$

Curiously, for the normal distribution, the expected value, i. e., the first cumulant, coincides with the arithmetic mean. If there are  $n$  observations of the random variable  $X$ , its arithmetic mean is given by,  $\bar{x} = (1/n) \cdot \sum_{i=1}^n x_i$ . This fact will be demonstrated below. Taking  $n$  i.i.d. samples, the total probability of occurrence of those  $n$  events will be the multiplication of the individual probabilities, and the total probability density function can be represented by,

$$f_X(x_1, \dots, x_n | K_1, K_2) = \prod_{i=1}^n f_X(x_i | K_1, K_2) = \left( \frac{1}{\sqrt{2\pi \cdot k_2}} \right)^n \cdot e^{-\frac{\sum_{i=1}^n (x_i - K_1)^2}{2 \cdot K_2}}. \quad (4.30)$$

Equation 4.30 can be rewritten in a convenient way to explain the term  $\bar{x}$ , i. e., given by

$$f_X(x_1, \dots, x_n | K_1, K_2) = \left( \frac{1}{\sqrt{2\pi \cdot k_2}} \right)^n \cdot e^{-\frac{(\sum_{i=1}^n (x - \bar{x})^2) + n \cdot (\bar{x} - K_1)^2}{2 \cdot K_2}}. \quad (4.31)$$

The total probability  $f_X(x_1, \dots, x_n | K_1, K_2)$  is a constant value, therefore the partial derivative of  $f_X$  regarding any term of the equation will be zero. Similarly, the partial derivative of  $\ln(f_X)$  is also null. The partial derivative of  $\ln(f_X)$  will be taken with respect to  $K_1$ ,  $\frac{\partial \ln(f_X)}{\partial K_1}$ , which requires a lot simpler calculation than  $\frac{\partial f_X}{\partial K_1}$ , for this demonstration:

$$\begin{aligned} \frac{\partial \ln(f_X)}{\partial K_1} = 0 &\Leftrightarrow \frac{\partial}{\partial K_1} \cdot \left[ \ln \left( \left( \frac{1}{\sqrt{2\pi \cdot k_2}} \right)^n \cdot e^{-\frac{(\sum_{i=1}^n (x - \bar{x})^2) + n \cdot (\bar{x} - K_1)^2}{2 \cdot K_2}} \right) \right] = 0 \\ \frac{\partial}{\partial K_1} \cdot \left[ n \cdot \ln \left( \left( \frac{1}{\sqrt{2\pi \cdot k_2}} \right) \right) - \frac{(\sum_{i=1}^n (x - \bar{x})^2) + n \cdot (\bar{x} - K_1)^2}{2 \cdot K_2} \right] &= 0 \\ \frac{\partial \ln(f_X)}{\partial K_1} = -\frac{2 \cdot n \cdot (\bar{x} - K_1)}{2 \cdot K_2} = 0 &\Rightarrow (\bar{x} - K_1) = 0 \Rightarrow K_1 = \bar{x} = \frac{1}{n} \sum_{i=1}^n x_i. \quad (4.32) \end{aligned}$$

So, the first cumulant of the normal distribution is the arithmetic mean. Similarly, the partial derivative of  $\ln(f_X)$  is taken with respect to  $K_2$  to find an estimator of the sample variance  $\hat{\sigma}^2$ :

$$\begin{aligned} \frac{\partial \ln(f_X)}{\partial K_2} = 0 &\Leftrightarrow \frac{\partial}{\partial K_2} \cdot \left[ \ln \left( \left( \frac{1}{\sqrt{2\pi \cdot k_2}} \right)^n \cdot e^{-\frac{\sum_{i=1}^n (x - \bar{x})^2}{2 \cdot K_2}} \right) \right] = 0 \\ \frac{\partial}{\partial K_2} \cdot \left[ n \cdot \ln \left( \left( \frac{1}{\sqrt{2\pi \cdot k_2}} \right) \right) - \frac{\sum_{i=1}^n (x - \bar{x})^2}{2 \cdot K_2} \right] &= 0 \\ \frac{\partial \ln(f_X)}{\partial K_2} = -\frac{n}{K_2} + \frac{\sum_{i=1}^n (x - \bar{x})^2}{K_2^2} = 0 &\Rightarrow K_2 = \frac{1}{n} \cdot \sum_{i=1}^n (x - \bar{x})^2 = \hat{\sigma}^2. \quad (4.33) \end{aligned}$$

The normal distribution of a random variable  $X$  can then be obtained with the arithmetic mean  $\bar{x}$  and the sample variance  $\hat{\sigma}^2$ ,  $f_X(x|\bar{x}, \hat{\sigma}^2)$ . Considering the multivariate case, the normal distribution of a set or a matrix  $\mathbf{X}$  with  $d$  random variables, is determined by the vector  $\bar{\mathbf{x}}$  of the arithmetic mean and the covariance matrix  $\mathbf{\Sigma}_X$ . Then, in the first example (eq. 4.21), the multivariate normal distribution of each class of the set  $\mathbf{S}$  is  $f_{C_1}(x|\bar{\mathbf{x}}_1, \mathbf{\Sigma}_1), f_{C_2}(x|\bar{\mathbf{x}}_2, \mathbf{\Sigma}_2), \dots, f_{C_k}(x|\bar{\mathbf{x}}_k, \mathbf{\Sigma}_k), \dots, f_{C_L}(x|\bar{\mathbf{x}}_L, \mathbf{\Sigma}_L)$ . For example, the multivariate normal distribution of  $\mathbf{C}_k$  is given by

$$f_{C_k}(x|\bar{\mathbf{x}}_k, \mathbf{\Sigma}_k) = N_k(\bar{\mathbf{x}}_k, \mathbf{\Sigma}_k) = \frac{1}{(2\pi)^{\frac{d}{2}} \cdot |\mathbf{\Sigma}_k|^{\frac{1}{2}}} \cdot e^{-\frac{1}{2}(\mathbf{x}-\bar{\mathbf{x}}_k)^T \mathbf{\Sigma}_k^{-1}(\mathbf{x}-\bar{\mathbf{x}}_k)}, \quad (4.34)$$

where, the vector  $\bar{\mathbf{x}}_k$  has the arithmetic mean of each random variable of class  $\mathbf{C}_k$  and the covariance matrix  $\mathbf{\Sigma}_K$  is given by  $\mathbf{\Sigma}_K = E[(\mathbf{x}_k - E[\mathbf{x}_k])(\mathbf{x}_k - E[\mathbf{x}_k])^T]$ , and by the result of eq. 4.32 the covariance matrix can be rewritten to  $\mathbf{\Sigma}_K = E[(\mathbf{x}_k - \bar{\mathbf{x}}_k)(\mathbf{x}_k - \bar{\mathbf{x}}_k)^T]$ . In which  $\mathbf{x}_k$ ,  $\bar{\mathbf{x}}_k$ , and the estimated  $\hat{\mathbf{\Sigma}}_K$  are

$$\mathbf{x}_k = \begin{bmatrix} x_1 \\ \vdots \\ x_d \end{bmatrix}, \bar{\mathbf{x}}_k = \begin{bmatrix} \bar{x}_1 \\ \vdots \\ \bar{x}_d \end{bmatrix}, \hat{\mathbf{\Sigma}}_K = \begin{bmatrix} \hat{\sigma}_1^2 & \dots & \hat{\sigma}_{1d} \\ \vdots & \ddots & \vdots \\ \hat{\sigma}_{d1} & \dots & \hat{\sigma}_d^2 \end{bmatrix}. \quad (4.35)$$

By the result of eq. 4.33 the variance ( $\hat{\sigma}_i^2$ ) and covariance ( $\hat{\sigma}_{ij}$ ) estimators of the sample covariance matrix are given by

$$\hat{\sigma}_{ij} = \frac{1}{n} \cdot \sum_{i=1}^n (x_i - \bar{x}_i)(x_j - \bar{x}_j), \text{ and } \hat{\sigma}_i^2 = \frac{1}{n} \cdot \sum_{i=1}^n (x_i - \bar{x}_i)^2, \quad (4.36)$$

where,  $i$  and  $j$  are random variables of  $\mathbf{x}$ . The resulting covariance matrix is then square and symmetric. The vector of the sample mean and sample covariance matrix are called sampling estimators (Fukunaga, 1990). The samples obtained from a normal distributed population tend to fall into a single set in which the center of the set is determined by the mean vector and the set shape is determined by the covariance matrix. Constant density samples are hyper-ellipsoids where the quadratic form  $(\mathbf{x} - \bar{\mathbf{x}})^T \mathbf{\Sigma}^{-1}(\mathbf{x} - \bar{\mathbf{x}})$  is constant. The main axes of these hyper-ellipsoids are given by the  $\mathbf{\Sigma}$  eigenvectors, and

its eigenvalues determine the size of these axes. The measure  $r^2 = (\mathbf{x} - \bar{\mathbf{x}})^T \boldsymbol{\Sigma}^{-1} (\mathbf{x} - \bar{\mathbf{x}})$  is the Mahalanobis distance from  $\mathbf{x}$  to  $\bar{\mathbf{x}}$ . Thus, the contours of constant density are hyper-ellipsoids with a constant Mahalanobis distance for  $\bar{\mathbf{x}}$  and the volume of such hyper-ellipsoids measures sample dispersion over the mean (Duda, et al., 2000).

Figure 4.13 - Left shows a univariate normal distribution of the random variable  $x$ . In this figure the mean  $\bar{x}$  is represented by  $\mu$ , and the distribution is defined by its mean  $\mu$  and standard deviation  $\sigma$ , where 95% of the distribution is in the interval  $|x - \mu| \leq 2\sigma$ . Figure 4.13 - Right shows the bidimensional feature space of the random variables  $x_1$  and  $x_2$ . The bivariate normal curve would be represented in a three dimensional space as a function of  $x_1, x_2$  and the probability  $P(x)$  and centered about the mean  $\bar{x}$ . In this figure, the ellipses represent section planes at different heights from the normal, which are the Mahalanobis distances that show constant probability density lines (Duda, et al., 2000).

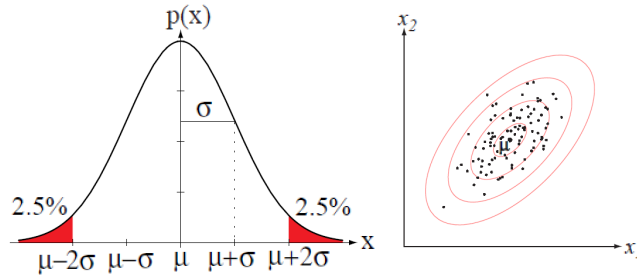


Figure 4.13 – Left: Univariate normal distribution; Right: Mahalanobis distances from a bivariate normal distribution (Duda, et al., 2000).

### 4.6.3 Normal classifier

The normal PDF is calculated for each class, then, the posteriori probability that a vector of observed variables,  $\mathbf{x}$ , is contained in a certain class can be obtained from eq. 3.8. Then, the rule of highest likelihood is used to assign a particular class to  $\mathbf{x}$ . The rule states that the vector of observed variables belonging to the class  $\mathbf{C}_k$  that obtained the highest discriminant function,  $g_k$ , (Anderson, et al., 2007), is given by

$$\mathbf{x} \in \mathbf{C}_k / \mathbf{C}_k = \operatorname{argmax}(g_i), i \in \{1, \dots, L\}, \quad (4.37)$$

where the function  $\operatorname{argmax}(\cdot)$  takes the maximum value of a set. The quadratic discriminant function is given by the natural logarithm of the posteriori probability,

$g_k = \ln(P(\mathbf{C}_k|\mathbf{x}))$  (eq. 4.38). In this equation some simplifications can be made: first the term  $-\ln(P(\mathbf{x}))$  is only a scaling factor and it can be neglected. For the cases where the priori probability  $P(\mathbf{C}_k)$  is equal for all classes the term  $\ln(P(\mathbf{C}_k))$  can also be neglected. Finally, the term  $-(d/2) \cdot \ln(2\pi)$  is constant for all classes and it can also be neglected (Duda, et al., 2000).

$$\begin{aligned}
g_k(\mathbf{x}) &= \ln(P(\mathbf{C}_k|\mathbf{x})) = \ln\left(\frac{P(\mathbf{x}|\mathbf{C}_k) \cdot P(\mathbf{C}_k)}{P(\mathbf{x})}\right) = \ln(P(\mathbf{x}|\mathbf{C}_k)) - \ln(P(\mathbf{x})) + \ln(P(\mathbf{C}_k)) \rightarrow \\
g_k(\mathbf{x}) &= \ln(P(\mathbf{x}|\mathbf{C}_k)) = \ln(N_k(\bar{\mathbf{x}}_k, \mathbf{\Sigma}_k)) = \ln\left(\frac{1}{(2\pi)^{\frac{d}{2}} \cdot |\mathbf{\Sigma}_k|^{\frac{1}{2}}}\right) \cdot e^{-\frac{1}{2}(\mathbf{x}-\bar{\mathbf{x}}_k)^T \mathbf{\Sigma}_k^{-1}(\mathbf{x}-\bar{\mathbf{x}}_k)} \leftrightarrow \\
g_k(\mathbf{x}) &= -\frac{1}{2}(\mathbf{x}-\bar{\mathbf{x}}_k)^T \mathbf{\Sigma}_k^{-1}(\mathbf{x}-\bar{\mathbf{x}}_k) - \frac{d}{2} \ln(2\pi) - \frac{1}{2} \ln(|\mathbf{\Sigma}_k|) \rightarrow \\
g_k(\mathbf{x}) &= -\frac{1}{2}(\mathbf{x}-\bar{\mathbf{x}}_k)^T \mathbf{\Sigma}_k^{-1}(\mathbf{x}-\bar{\mathbf{x}}_k) - \frac{1}{2} \ln(|\mathbf{\Sigma}_k|). \quad (4.38)
\end{aligned}$$

Therefore, the arithmetic mean and the sample covariance matrix are calculated from eq. 4.32 and eq. 4.36 for each class, and the discriminant function of each one can be obtained. When an unknown event  $\mathbf{x}$  occurs, the discriminant functions are applied and the value obtained by a discriminant function is not a probability anymore, but it is related to the posteriori probability. Then, the higher the discriminant value of a class, the higher the posteriori probability that the observed event belongs to this class. Therefore, to use the rule of highest likeness is the same as to attribute to  $\mathbf{x}$  the class with the highest probability of containing it. This solution leads to nonlinear, or quadratic, discriminants and it is also known as Quadratic Discriminant Analysis (QDA). Figure 4.14 - A shows a nonlinear decision region between two univariate normal distributions with same mean and different variances. Figure 4.14 - B shows a nonlinear decision region between two bivariate normal distributions, and Figure 4.14 - C shows nonlinear decision regions between four bivariate normal distributions.

A particular case is obtained by using the linear discriminant function. In this case it is assumed that the covariance matrices of all classes are equal ( $\mathbf{\Sigma}_1 = \mathbf{\Sigma}_2 = \dots = \mathbf{\Sigma}_k = \dots = \mathbf{\Sigma}_L = \mathbf{\Sigma}$ ). Therefore, the term  $-(1/2) \cdot \ln(|\mathbf{\Sigma}_k|)$  from eq. 4.38 is independent from the classes, being a constant that can be neglected. Also, for the cases where the priori probability  $P(\mathbf{C}_k)$  is equal for all classes the term  $\ln(P(\mathbf{C}_k))$  can also be neglected.

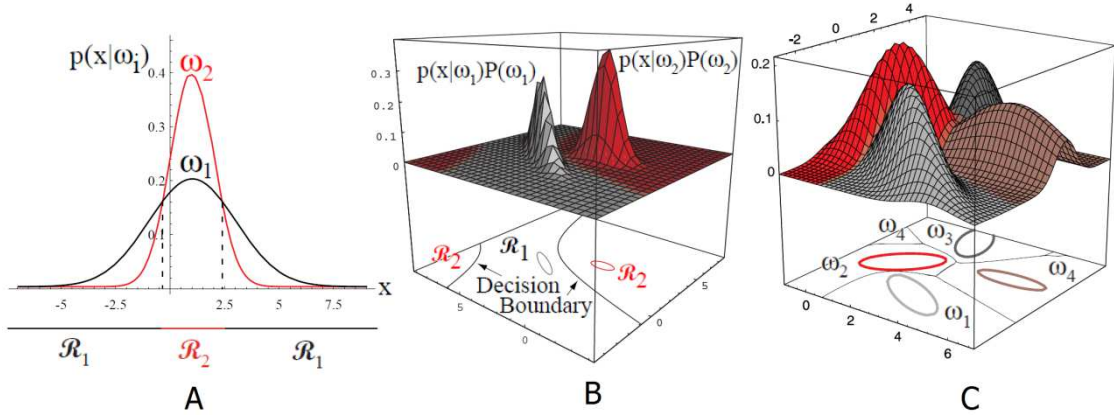


Figure 4.14 – Nonlinear decision regions. (A) Decision boundary between two univariate normal distributions; (B) Decision boundary between two bivariate normal distributions; (C) Decision boundary between two four bivariate normal distributions (Duda, et al., 2001).

$$g_k(\mathbf{x}) = -\frac{1}{2}(\mathbf{x} - \bar{\mathbf{x}}_k)^T \boldsymbol{\Sigma}_k^{-1}(\mathbf{x} - \bar{\mathbf{x}}_k) - \frac{1}{2} \ln(|\boldsymbol{\Sigma}|) + \ln(P(\mathbf{C}_k)) \rightarrow$$

$$g_k(\mathbf{x}) = -\frac{1}{2}(\mathbf{x} - \bar{\mathbf{x}}_k)^T \boldsymbol{\Sigma}^{-1}(\mathbf{x} - \bar{\mathbf{x}}_k). \quad (4.39)$$

Expanding the quadratic term of eq. 4.39,  $(\mathbf{x} - \bar{\mathbf{x}}_k)^T \boldsymbol{\Sigma}^{-1}(\mathbf{x} - \bar{\mathbf{x}}_k)$ , results in,

$$g_k(\mathbf{x}) = -\frac{1}{2} \mathbf{x}^T \boldsymbol{\Sigma}^{-1}(\mathbf{x} - \bar{\mathbf{x}}_k) + \frac{1}{2} \bar{\mathbf{x}}_k^T \boldsymbol{\Sigma}^{-1}(\mathbf{x} - \bar{\mathbf{x}}_k) \leftrightarrow$$

$$g_k(\mathbf{x}) = -\frac{1}{2} \mathbf{x}^T \boldsymbol{\Sigma}^{-1} \mathbf{x} + \frac{1}{2} \mathbf{x}^T \boldsymbol{\Sigma}^{-1} \bar{\mathbf{x}}_k + \frac{1}{2} \bar{\mathbf{x}}_k^T \boldsymbol{\Sigma}^{-1} \mathbf{x} - \frac{1}{2} \bar{\mathbf{x}}_k^T \boldsymbol{\Sigma}^{-1} \bar{\mathbf{x}}_k \rightarrow$$

$$g_k(\mathbf{x}) = \bar{\mathbf{x}}_k^T \boldsymbol{\Sigma}^{-1} \mathbf{x} - \frac{1}{2} \bar{\mathbf{x}}_k^T \boldsymbol{\Sigma}^{-1} \bar{\mathbf{x}}_k. \quad (4.40)$$

In eq. 4.40 the term  $-(1/2) \cdot \mathbf{x}^T \boldsymbol{\Sigma}^{-1} \mathbf{x}$  is independent from the class  $\mathbf{C}_k$ , then, it is a constant that can be neglected. Thus, the discriminant function of eq. 4.40 results in a linear decision region and this approach it is also known as Linear Discriminant Analysis (LDA). Geometrically, this corresponds to the situation in which the samples are sets of hyper-ellipsoids with identical shape and size, and the separation region is defined by a hyperplane (Duda, et al., 2000). Finally, the rule of maximum likeness is applied to assign a class to the unknown observation  $\mathbf{x}$ . Figure 4.15 shows a linear decision region of normal distributions. Figure 4.15 - A shows a decision region between two univariate normal distributions, in which the priori probability of class named  $w_1$  and class  $w_2$  is 0.5. Figure 4.15 - B shows a decision region between two

bivariate normal distributions, in which the priori probability of class  $w_1$  and class  $w_2$  is 0.5. Figure 4.15 - C shows the separation plane for two multivariate normal distributions with priori probabilities of 0.5.

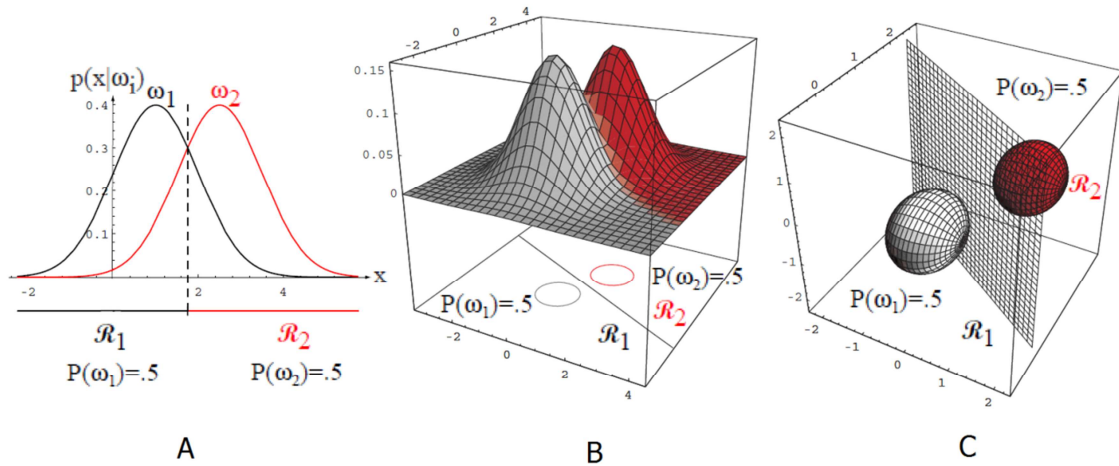


Figure 4.15 – Linear decision region of normal distributions. (A) Univariate normal distributions; (B) Bivariate normal distributions; (C) Multivariate normal distributions (Duda, et al., 2000).

#### 4.7 Simulated results and the reclassification method

As previously mentioned in section 4.3, the EEG features are the PSD frequency components obtained over stationary time windows of 2 s shifted for every new sample (the sliding window technique). The feature selection was made using the K-L symmetric divergence associated with the threshold analysis, as is mentioned in section 4.4. Finally, a normal Bayesian classifier with a linear discriminant function was used for classification of the dataset described in section 4.1. As the normal PDF is estimated for the classification Figure 4.16 shows the EEG histograms of the 19 channels of International 10-20 System and each estimated normal PDF. The histograms were obtained for the interval of  $\pm 20 \mu V$  using 50 equally spaced intervals during the mental task of imagination of movement of the left hand. It can be seen that the normal PDF resembles the histograms general shapes.

In this dataset three normal subjects performed three mental tasks without feedback. The mental tasks were the imagination of movement of left/right hands and the thought of words beginning with a given random letter. The mental tasks were originally labeled as 2, 3 and 7 in the dataset, but they will henceforth be referred as class 1, 2 and 3, respectively. The first two sessions of each subject were used to estimate the mean ( $\bar{x}_1, \bar{x}_2, \bar{x}_3$ ) and the sample covariance matrices ( $\hat{\Sigma}_1, \hat{\Sigma}_2, \hat{\Sigma}_3$ ) of each

class. As a linear discriminant function was used, the average covariance matrix taken over the three covariance matrices was used,  $\bar{\Sigma} = (1/3) \cdot (\sum_{i=1}^3 \hat{\Sigma}_i)$ , in eq. 4.40. The third session of each subject was used for the classifier validation, and all classes were considered equiprobable.

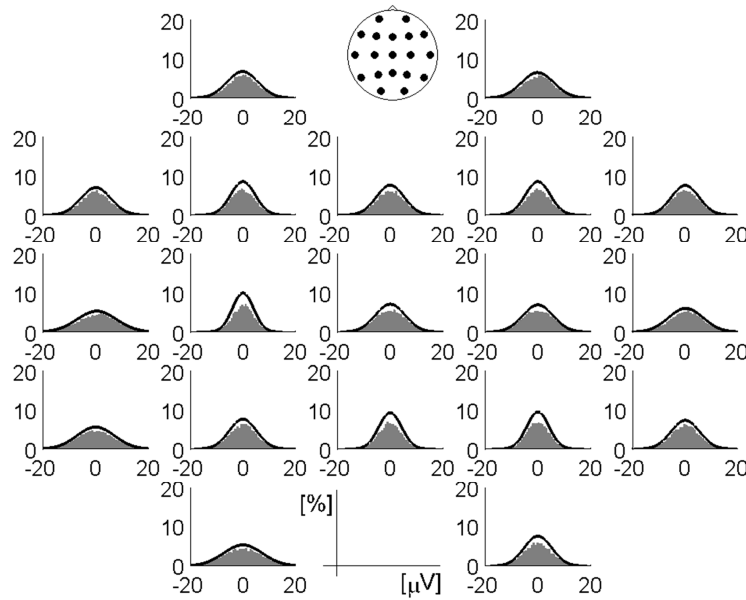


Figure 4.16 – EEG histograms and estimated normal probability functions of subject 1 during the mental task of imagination of movement of the left hand.

As 2 sessions of the sub-sampled EEG of each subject are used, and the PSD is calculated for 2 s time window with the sliding window technique, then 10,112 samples are available for each class. Therefore, the Sturge's rule (eq. 4.16) estimates that  $k' = 14.3038$  and 15 bins are also used to calculate the histograms of the K-L method.

Figure 4.17 shows the classifier output, which represents the current BCI output. The best values of the success rate for subjects 1, 2, and 3 were  $83.77 \pm 1.27\%$  (with discriminant threshold of  $\xi = 50\%$ ),  $65.75 \pm 1.52\%$  ( $\xi = 50\%$ ), and  $55.53 \pm 1.59\%$  ( $\xi = 0\%$ , i.e., using all PSD components), respectively. In this figure, the real class is represented by the dotted line and the predicted class is represented by the continuous line (Benevides et al., 2012a). In Figure 4.17, the predicted class oscillates faster than the user could change tasks, which indicates that the classifier is unstable. Therefore, a method to smooth the classifications was developed. Each output forms a new vector of classification, which stores the previous classifications for a period of time, called the reclassification window. These windows behave as time windows; they are



continuously displaced by one classification, and thus do not change the original classification rate of the system.

The reclassification could use the most frequent class in the reclassification window, but this will lead to a delay during the transitions of mental tasks, since the new class should occur more often than the old class to allow the classifier to identify a class change. To minimize the delay, the output of the classifier is the class with the highest weight in the reclassification window. The weight of each past classification is given in relation to the size of the subgroup of equal classes that it belongs to (Figure 4.18).

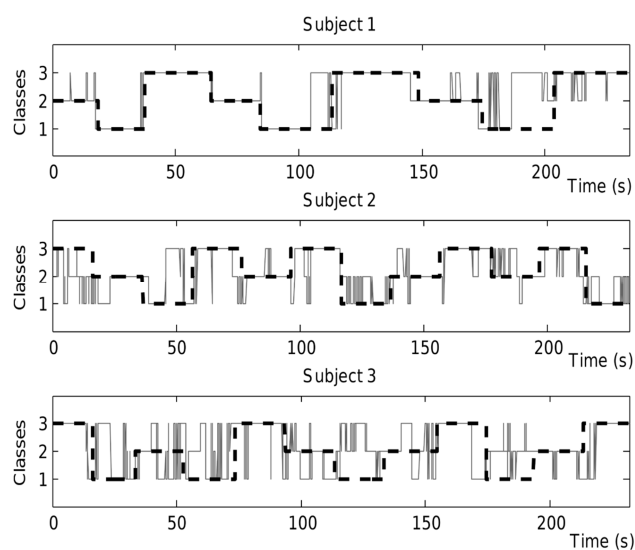


Figure 4.17 – Classifier output.

The weight is the inverse of the probability of a repeated occurrence of a class. Thus, even if two classes have the same number of occurrences within the reclassification window, the class that occurs repeatedly is more likely to be the current class than one class with the same number of occurrences, but which occurred randomly. Then, for three equiprobable classes, a sample in a subgroup with size  $n$  has probability  $P(s) = (1/3)^n$ . Thus, the weight of this sample is given by  $W(s) = (3)^n$ . This penalizes isolated samples or samples in small subgroups among identical classifications, which create noise in the classification. Figure 3.16 shows an example where the reclassification window is composed of nine past classifications. Although the 3 classes occur the same number of times, the class that occurs more times without changing will have the highest weight and be assigned to the system output (Benevides et al., 2011e).

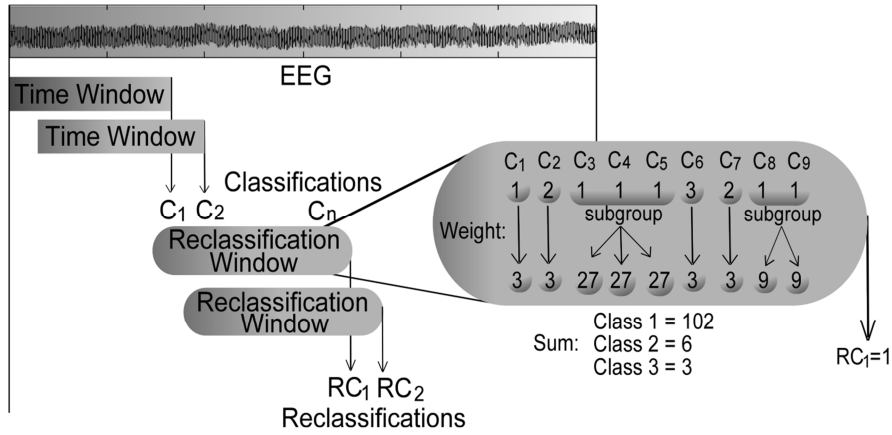


Figure 4.18 – Time windows and reclassification windows.

Two parameters were varied each in turn: the length of the classification windows,  $\lambda$ , which was varied from 1 to 5 s and the discriminant threshold,  $\xi$ . Figure 4.19 shows the curves obtained for each subject, wherein the circle indicates the best values of  $\lambda$  for a constant  $\xi$ .

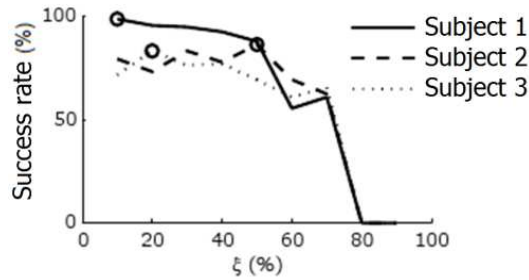


Figure 4.19 – Success rate for different values of  $\xi$ .

Figure 4.20 shows the system output after reclassification using the values of  $\xi$  and the classification windows size  $\lambda$  which produced the best result. In this figure there is a significant improvement in the stability of the system response. Table 4.2 shows the best values of the success rate of each subject and the parameters ( $\xi$ ,  $\lambda$ ) used (Benevides et al., 2012a). In the last column,  $B$  is the information transfer rate, calculated in bits/min as used by Obermaier et al. (2001), and it is given by

$$B = \log_2 L + s \cdot \log_2 s + (1 - s) \cdot \log_2 \left( \frac{1 - s}{L - 1} \right), \quad (4.41)$$

where  $L$  is the number of classes and  $s$  is the success rate.

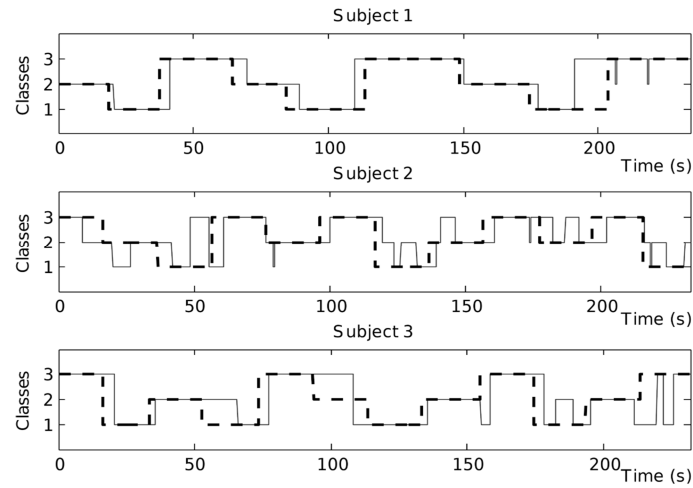


Figure 4.20 –Reclassification.

Table 4.2 – Results from each subject.

	Success rate	$\xi$	$\lambda$	$B$ [bits/min]
Subj. 1	94.93±0.71%	50%	2.5s	29.88
Subj. 2	78.89±1.31%	50%	1.88s	20.12
Subj. 3	81.31±1.25%	0%	5s	8.44

Table 4.3 shows the statistical measures of accuracy, sensitivity and specificity of the best system configuration for each class of each subject.

Table 4.3 – Statistical measures from each subject.

	Accuracy			Sensitivity			Specificity		
	Subj. 1	Subj. 2	Subj. 3	Subj. 1	Subj. 2	Subj. 3	Subj. 1	Subj. 2	Subj. 3
$C_1$	0.85	0.54	0.80	1	0.79	0.79	0.95	0.87	0.90
$C_2$	0.98	0.80	0.80	0.97	0.73	0.79	0.99	0.86	0.91
$C_3$	0.99	0.93	0.83	0.91	0.85	0.86	0.99	0.95	0.91

The differences in the accuracy of the subjects are likely due to the differences in concentration level during a task, reflecting the ease or difficulty of the subject in imagining the mental task. A solution would be to implement a training step with feedback, giving users with lower concentration a longer training phase. The use of feedback also allows the mutual adaptation of the user and the classifier, which could greatly improve the BCI reliability. It could be implemented by means of an online interface showing the subject performance during the mental task. Finally, the results presented here were compared with some results submitted to BCI Competition III, which used the same datasets and mental tasks used here. The results are shown in table 4.4 and were obtained from BCI competition III website (2005) and at Anderson et al. (2007).

Table 4.4 – Comparison with best results of dataset V submitted to BCI Competition III. The row labeled “Authors\*” shows the classifications results obtained using 0.5 s reclassification windows, which is the same length used by the other studies shown here.

	Subject 1	Subject 2	Subject 3	Mean
Authors	94.93	78.89	81.31	85.04
Authors*	84.09	69.34	65.66	73.03
F. Galan	79.60	70.31	56.02	68.65
X. Liao	78.08	71.66	55.73	68.50
Walter	77.85	66.36	53.44	65.90
S. Sun	74.31	62.32	51.99	62.83
C. Anderson	62.30	57.60	47.50	55.80
A. Schlögl	69.00	57.05	32.29	52.71
E. Arbabi	55.41	51.79	43.61	50.25
A. Salehi	26.54	32.84	24.53	27.97

First, some considerations about the results of table 4.4 need to be given. In table 4.4, the classifications were performed using a simple reclassification method. Smoothing was applied to the classification results with 0.5 s windows, which likely leads to a delay during classification. Although the results of the proposed method are on average 16.3% better than those of the best work, reclassification windows of up to 5 seconds were used. The proposed reclassification method leads to shorter delays, which justifies the use of larger reclassification windows. For fair comparison, the second row of Table 4.4, labeled “Authors\*”, shows the classification results obtained with 0.5 s reclassification windows. Our results are on average 4.3% better than those of the best work of Table 4.4. The performance improvement is attributed to the use of symmetric K-L divergence for feature selection (Benevides et al., 2012a).

It should also be noted that each work compared in table 4.4 used different techniques. For example, Shiliang Sun et al. (Tsinghua University, Beijing) previously removed artifacts of seven channels, and the EEG signal was filtered between 8-13 Hz for subject 1 and 2 and between 11 to 15 Hz for subject 3. Common Spatial Patterns (CSP) and Support Vector Machines (SVMs) were used for the classification. Anderson et al. used Short-time PCA for feature extraction and LDA for the classification. Alois Schlögl et al. (Graz University of Technology) sub-sampled the signal to 128 Hz, formed bipolar channels and estimated autoregressive models for each channel. Then, the  $\mu$  and  $\beta$  energy were obtained and the best feature was used for a statistical

classification. Ehsan Arbabi et al. (Sharif University of Technology, Iran) sub-sampled the signal to 128 Hz and filtered it between 0.5 to 45 Hz. Features based on statistical measures and parametric models were extracted using 1 s windows and classification was made by a Bayesian classifier. Ali Salehi used a combination of the Short-time Fourier Transform (STFT) energy and temporal features to perform the classification by means of a Bayesian classifier.

## Chapter 5 : Results

This Chapter will describe our experimental environment and protocol, as well as the application of some tests that were used in the dataset V taken from our own data. The ACF rule was applied in order to estimate the EEG sample rate. The KPSS, ADF and Runs Test are applied in order to verify the EEG stationarity and the time windows length. The histograms of all channels of the International 10-20 System are shown together with the estimated normal PDFs. The ERD/ERS patterns and spectrograms were calculated for all channels and were shown as scalp maps for the frequencies bands  $\alpha/\mu$ ,  $\beta$  and  $\gamma$ . The processing time of the artifact removal techniques presented in section 3.6 was calculated in order to evaluate whether it is possible to adapt the algorithms to an online approach. Finally, an analysis of the EEG SNR was performed during different mental tasks and artifact removal techniques.

### 5.1 Experimental environment

Data were acquired with five right handed male subjects, aged between 26 to 34 years ( $30.4 \pm 3.5$ ). All subjects had normal hearing, normal or corrected-to-normal vision and no history of substance abuse, major medical psychiatric illness, or developmental or neurological disorder. Each subject performed five mental tasks, which were the imagination of the movement of right and left hands, of both feet, of the rotation of a cube and of music imagery.

For EEG acquisition, the device BrainNet36<sup>®</sup> (BNT), from EMSA *Equipamentos Médicos Ltda.* (Figure 5.1 - A), was used with a cap of integrated electrodes from MedCap<sup>®</sup> company (Figure 5.1 - C). We used 19 electrodes positioned according to the international 10-20 system (Fp1, Fp2, F7, F3, Fz, F4, F8, T3, C3, Cz, C4, T4, T5, P3, Pz, P4, T6, O1 and O2). As explained in section 3.2 the grounding electrode was positioned on the user forehead, and monoauricular reference was adopted and all impedances were kept below 5 k $\Omega$  (Ford et al., 2004; Luck, 2005). The EEG was acquired at a sampling rate of 200 Hz. The BNT has 36 channels (Figure 5.1 - B), A/D converters with 16 bit accuracy, conversion time of 10  $\mu$ s and Ethernet communication interface (BNT36 User's manual, 2004). Being a device for clinical purposes, the BNT does not export data online. Therefore, a sniffer was programmed in

ANSI C to export these data in an online way, allowing the online processing, which was performed by MATLAB 7.11.0<sup>®</sup> (R2010b) on a computer with Intel<sup>®</sup> Core<sup>™</sup> i7 processor with a clock speed of 2.10 GHz, 8 GB of RAM and a HDD of 1 TB.

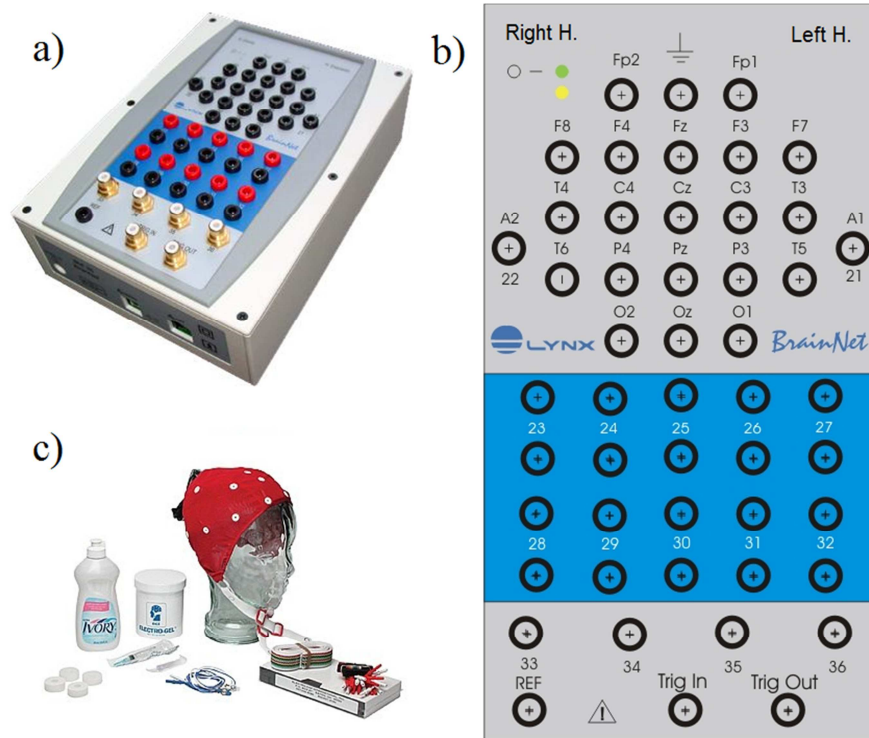


Figure 5.1 – a) BNT device; b) BNT panel (adapted from BrainNet - BNT36 User's manual, 2004); c) MedCap<sup>®</sup> cap of integrated electrodes, conductive electrolytic gel and paste.

The sniffer is a program able to track the data packets sent into a network. The BNT sends UDP packets with coded EEG information, then, the sniffer is configured in the promiscuous mode to observe and decode the data, writing them into a text file, without blocking the original data flow. The sniffer works together with routines implemented in the MATLAB. As the data is sent by BNT, the sniffer writes the text file that is read and deleted by the MATLAB routine. When the text file is deleted the sniffer creates another text file with the next BNT packets. The sniffer was released as free and open source software in accordance with the General Public License version 3.0 (GPLv3) and published in the web-based source code repository SourceForge (Benevides, A. B. [Alessander] and Benevides, A. B. [Alessandro], 2013). More information about the sniffer and the data transfer protocol of the BrainNet36<sup>®</sup> can be found in appendix A.

Regarding the experimental protocol, for each mental task sixty epochs were taken, each epoch corresponding to 25 s. For each epoch subjects were instructed to sit with their hands resting on their legs and to observe a cross in the center of the screen. The cross is a fixation point to avoid excessive artifact from eye movement. After 5 s an arrow replaces the cross indicating the start of the mental task. The mental task lasts 10 s, and then the cross reappears in place of the arrow indicating that the mental task is over. The subject must remain still until the cross is replaced by a circle at time 25 s, indicating the end of the record.

For the left/right hand task the subject was instructed to imagine the movement of the right arm and hand in order to reach and grab an object placed in a table in front of him at a distance of 30 cm. The subject was instructed to repeatedly perform this imaginary movement, at his own pace, from the 5 to the 15 s mark of the EEG record. For the foot task the subject was instructed to imagine the movement of extending both legs, and thus raising both feet. In the same way, the subject was instructed to repeatedly perform this imaginary movement, at his own pace, from the 5 to the 15 s mark of the EEG record.

For the rotation of a cube task the subject was instructed to imagine that he was manipulating a Rubik's cube<sup>45</sup> with both hands. In order to facilitate the imagination, a real Rubik's cube was placed in a table in front of him at a distance of 30 cm. In the same way, the subject was instructed to repeatedly perform this imaginary movement, at his own pace, from the 5 to the 15 s mark of the EEG record. Finally, for the music imagery task the subject was instructed to remember just instrumental music, with no lyrics, to avoid the association of brain areas related to language, from the 5 to the 15 s mark of the EEG record.

It is worth commenting that the project was approved by the Ethics Committee of the Universidade Federal do Espírito Santo (Brazil), recognized by the Ethics Committee of the Research Ethics National Commission (CEP-048/08).

## 5.2 EEG pre-processing and histograms

The present study used different motor and non-motor related tasks, and as we do not know the exact size of the brain areas that are active during these mental tasks,

---

<sup>45</sup> Rubik's Cube is a 3-D combination puzzle invented in 1974 by Hungarian sculptor and professor of architecture Ernő Rubik, and was originally called the "Magic Cube".



the CAR method was adopted. As a normal Bayesian classifier with a linear discriminant function was chosen for classification, Figure 5.2 shows the EEG histograms of the 19 channels of International 10-20 System and each estimated normal PDF. The histograms were obtained using all sixty epochs of the mental task of imagination of movement of the right hand of subject 1, for the interval of  $\pm 100 \mu V$ , using 50 equally spaced intervals. It can be seen that the normal PDF resembles the histograms general shapes.

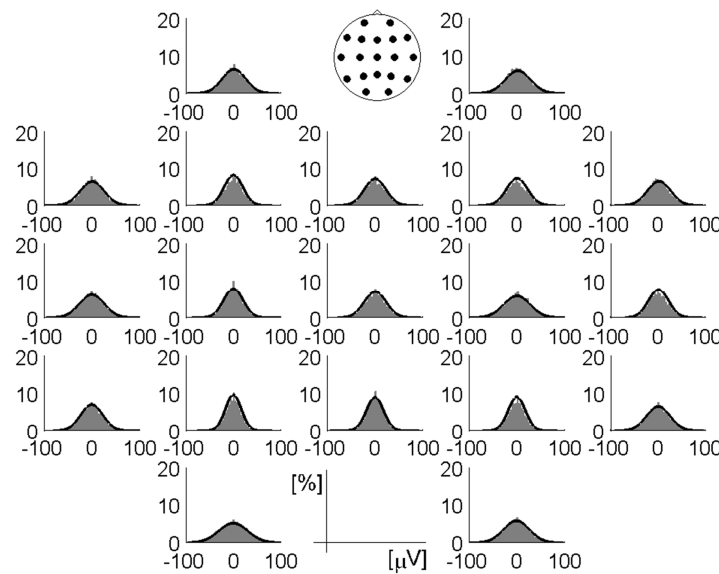


Figure 5.2 – EEG histograms and estimated normal probability functions of subject 1 during the mental task of imagination of movement of the right hand.

### 5.3 ERD/ERS scalp maps

In order to investigate the possibility of extending our BCI to operate with both, motor and music imagery paradigms, five mental tasks were studied. The SNR and the differences between ERD/ERS scalp maps of these five mental tasks were used as a factor in making a decision about choosing new tasks to be used in the aforementioned BCI (Benevides et al., 2012b-c).

The traditional method to obtain the ERD/ERS, described in section 3.9, was implemented for 19 electrodes positioned according to the international 10-20 system. The ERD/ERS calculated for the 19 electrodes was shown as scalp maps for the frequency bands  $\alpha/\mu$  (8-12 Hz),  $\beta$  (14-30 Hz) and  $\gamma$  (30-100 Hz). In Chapter 3, the Figure 3.24 exemplified the application of the classic method for measuring the ERD/ERS pattern for the mental task of imagination of movement of the right hand

from subject 1 from our dataset. Then, regarding the sound imagery task, diverse studies assert that neural activity in the secondary auditory cortex can occur in the absence of sound as a consequence of the experience of imagining music (Zatorre et al., 2005). The sound imagery generally elicits a posterior synchronization (ERS) in the parieto-occipital  $\alpha$  band, which may relate to the inhibition of non-task relevant cortical areas, such as the visual areas. However, the individual variability during sound imagery is highly significant and some early EEG studies reported conflicting findings as decreases, increases or null responses in the  $\alpha$  band when listening to music (Schaefer et al., 2011b). Then, since there was no consolidated information about the occurrence of ERD/ERS during music imagery, the ERD/ERS analysis and the spectrograms presented cover a wide range of frequencies.

The relative energy of the EEG filtered at the  $\alpha/\mu$  (8-12 Hz),  $\beta$  (14-30 Hz) and  $\gamma$  (30-100 Hz) bands was calculated for all the 19 electrodes and all mental tasks. The  $\mu$  frequency band lies on the same frequency interval as the  $\alpha$  band, and the distinction between them is mostly the location at which they are measured. The  $\mu$  band is observed over the sensorimotor cortex, and the  $\alpha$  band is observed over almost the entire scalp. Then, during the analysis of the ERD/ERS scalp maps, the EEG filtered at 8-12 Hz was referred to without distinction as the  $\alpha/\mu$  band, since the electrodes of sensorimotor areas and other areas could be mentioned together.

The ERD/ERS protocol described in the previous section was adopted, 60 epochs were taken for the motor related mental tasks, and 80 epochs were taken for the music imagery mental task, which were shown to be more than enough. Because of space constraints we only show the ERD/ERS scalp maps of subject 1 (29 year old). Figure 5.3 - A shows the arrangement of electrodes on the scalp. Figures 5.2 (B, C, D and E) show the ERD/ERS scalp maps of the EEG filtered at the  $\alpha/\mu$  (black),  $\beta$  (dark gray), and  $\gamma$  (light gray) frequency bands. To avoid overloading the figure, the amplitude and time scales are shown only for channels Fp1 and Fp2, but all channels are related to the same scale.

Figure 5.3 - B shows the ERD/ERS scalp map during the mental task of imagination of movement of the right hand. The ERD/ERS pattern is observed spread over the scalp and the highest ERS occurs at the electrode C3. Electrodes on the parietal area (P3, Pz and P4) exhibit ERD only at the  $\mu$  band. Figure 5.3 - C shows the ERD/ERS scalp map during the mental task of imagination of movement of the left hand. The ERD/ERS pattern is observed spread over the scalp and there is a little

difference between it and the scalp map of Figure 5.3 - B, which is the absence of the ERD at the  $\mu$  band in electrodes Pz and P4.

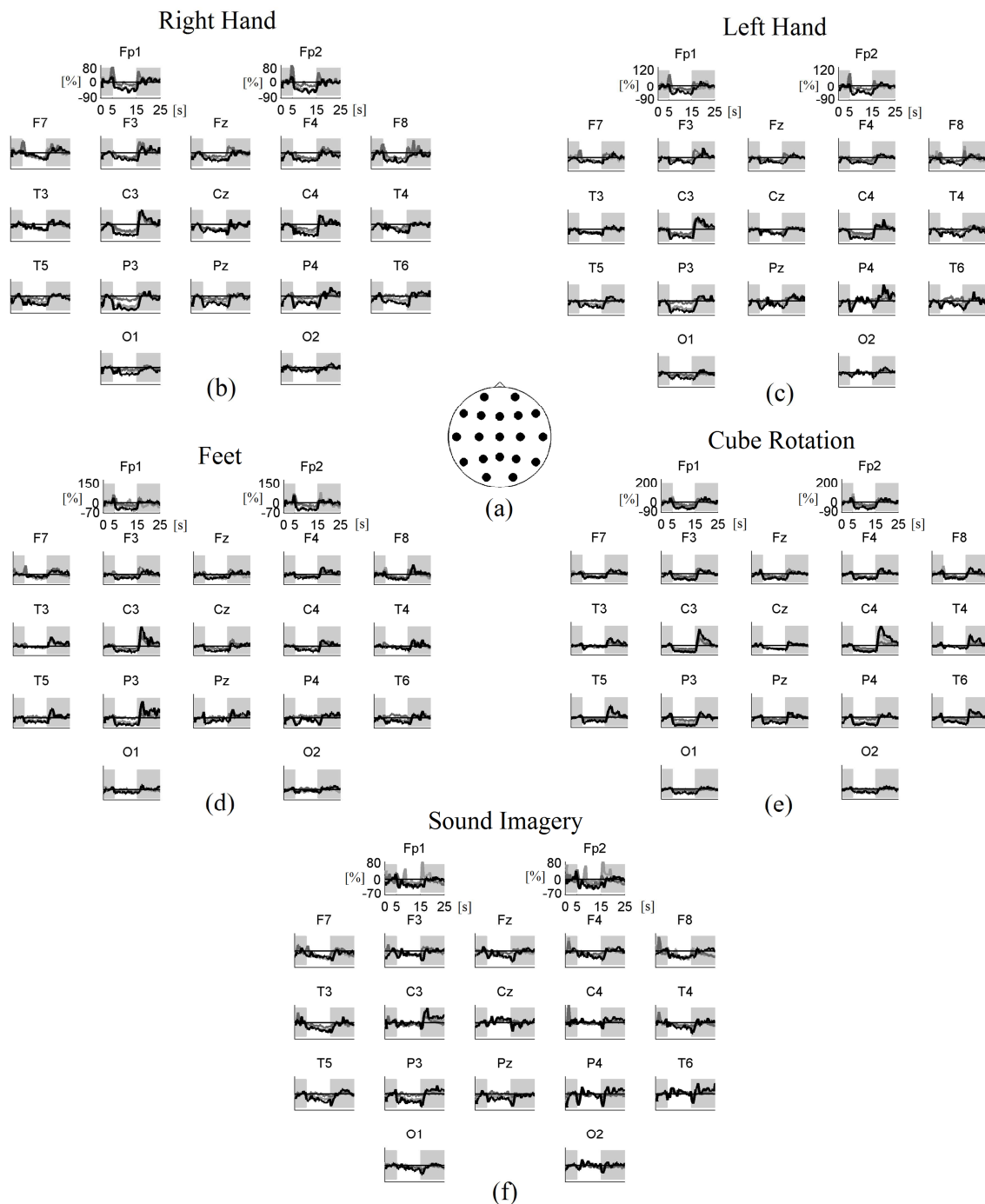


Figure 5.3 – Relative energy of the  $\alpha/\mu$ ,  $\beta$  and  $\gamma$  bands. The reference period was taken between 1 and 3 s and the mental task occurred between 5 and 15 s. (a) arrangement of electrodes; (b) ERD/ERS scalp map during the mental task of imagination of movement of the right hand; (c) ERD/ERS scalp map during the mental task of imagination of movement of the left hand; (d) ERD/ERS scalp map during the mental task of imagination of movement of both feet; (e) ERD/ERS scalp map during the mental task of rotation of a cube; (f) ERD/ERS scalp map during the mental task of music imagery.

Figure 5.3 - D shows the ERD/ERS scalp map during the mental task of imagination of movement of both feet. The ERD/ERS pattern is also observed spread over the scalp, and the main difference between this task and the hand-related mental tasks is the amplitude of the ERS occurring in electrodes C3 and P3. Figure 5.3 - E shows the ERD/ERS scalp map during the mental task of rotation of a cube. The ERD/ERS pattern is observed spread over the scalp, and the main difference between this task and the foot movement imagination of moving both feet is the ERS at the  $\mu$  band occurring in both electrodes C3 and C4.

Figure 5.3 - F shows the ERD/ERS scalp map during the mental task of music imagery. The ERD is observed less spread over the scalp, and for the  $\alpha/\mu$  band it is mainly observed in temporal sites (T3, T4 and T5), lateral-frontal sites (F7 and F8) and the parietal electrode P3. In the  $\beta$  band the ERD is only observed in electrodes T3, T4, F7 and F8. The ERD is observed in the  $\alpha$  and  $\beta$  bands with smaller amplitude in frontal sites (F3, Fz and F4). The main difference between this task and the motor-related mental tasks is the absence of ERD in the  $\mu$  band in the electrodes of the central area (C3, Cz and C4).

#### 5.4 Periodograms

As was previously mentioned, since there is no consolidated information about the occurrence of ERD/ERS and its frequency band during music imagery, and since the research of Klonowski et al. (2009) reports high-frequency peaks related to imagined tones, the periodogram from 1 to 100 Hz was calculated for all electrodes. The periodogram was also calculated for all motor mental tasks, in order to verify if the ERD/ERS pattern would occur at higher frequency bands. The periodogram used the PSD with Hamming windows of 1 s overlapped by 50%, being calculated separately for each mental task epoch (Davidson et al., 2000).

The periodograms of the EEG during all aforementioned mental tasks were calculated in absolute amplitudes and also in percentage values relative to the mean activity of each frequency over the time. The comparison between these two types of spectrograms showed at which frequencies the ERD/ERS could be measured and also its energy. Because, even if the ERD/ERS pattern could be measured at high frequencies by using a large number of epochs, if it presented very small amount of

energy the probability of being measured online for BCI applications would be low. Because of space constraints we only show the spectrograms for subject 1.

Figure 5.4 (A and B) shows the average periodogram during the mental task of rotation of a cube. In this figure the amplitudes are color-coded in gray scale. To avoid overloading the figure, the frequencies and time scales are shown only for channels Fp1 and Fp2, and all channels are related to the same color-coded scale. In Figure 5.4 - A it can be seen that the main activity occurs around 10 Hz, which has the highest energy variation. The energy variation at about 10 Hz is strongly related to the mental task, since the energy is lower between 5 s and 15 s (white central area). Figure 5.4 - B shows the periodogram focused on the activity from 0 to 30 Hz, and it also can be seen that the  $\alpha/\mu$  band has a higher energy variation than the  $\beta$  band.

Figure 5.4 (C and D) also shows the average periodogram during the mental task of rotation of a cube, but in this figure the amplitudes are percentage values relative to the mean activity of each frequency over the time, and are color-coded in gray scale. In Figure 5.4 - C, it can be seen that the ERD/ERS pattern occurs spread over all the analyzed frequency, thus not being an exclusive property of the  $\alpha/\mu$  band. The relative energy variation at 10 Hz was between -64.16 and 82.96 %, and at 100 Hz it was between -45.85 and 76.42 %. Then, the ERD/ERS could be measured even for frequencies near 100 Hz with percentage variations of just 16.89 % less than for 10 Hz. However in absolute amplitudes, the energy variation at 10 Hz was between 5.38 and 130.72  $\mu\text{V}^2$ , and at 100 Hz it was between 3.78 and 151.68  $\text{nV}^2$ , approximately one thousand times lower. The main feature then of the  $\alpha/\mu$  band, compared to the  $\beta$  and the  $\gamma$  bands, is its higher absolute energy variation, instead of the relative energy variation.

The periodograms of all mental tasks, including the music imagery, presented the same general behavior of Figure 5.4 (A and B), in which only the  $\alpha/\mu$  band shows a visible absolute energy variation. Figure 5.4 (E and F) shows the average periodogram during the mental task of music imagery. Figure 5.3 - E shows the periodogram from 1 to 100 Hz, and it can be seen that in general the ERD/ERS has lower amplitude than motor mental tasks. Figure 5.3 - F shows the periodogram from 1 to 30 Hz and it can be seen that the electrodes Cz, C4, Pz and T4 did not present the ERD/ERS pattern.

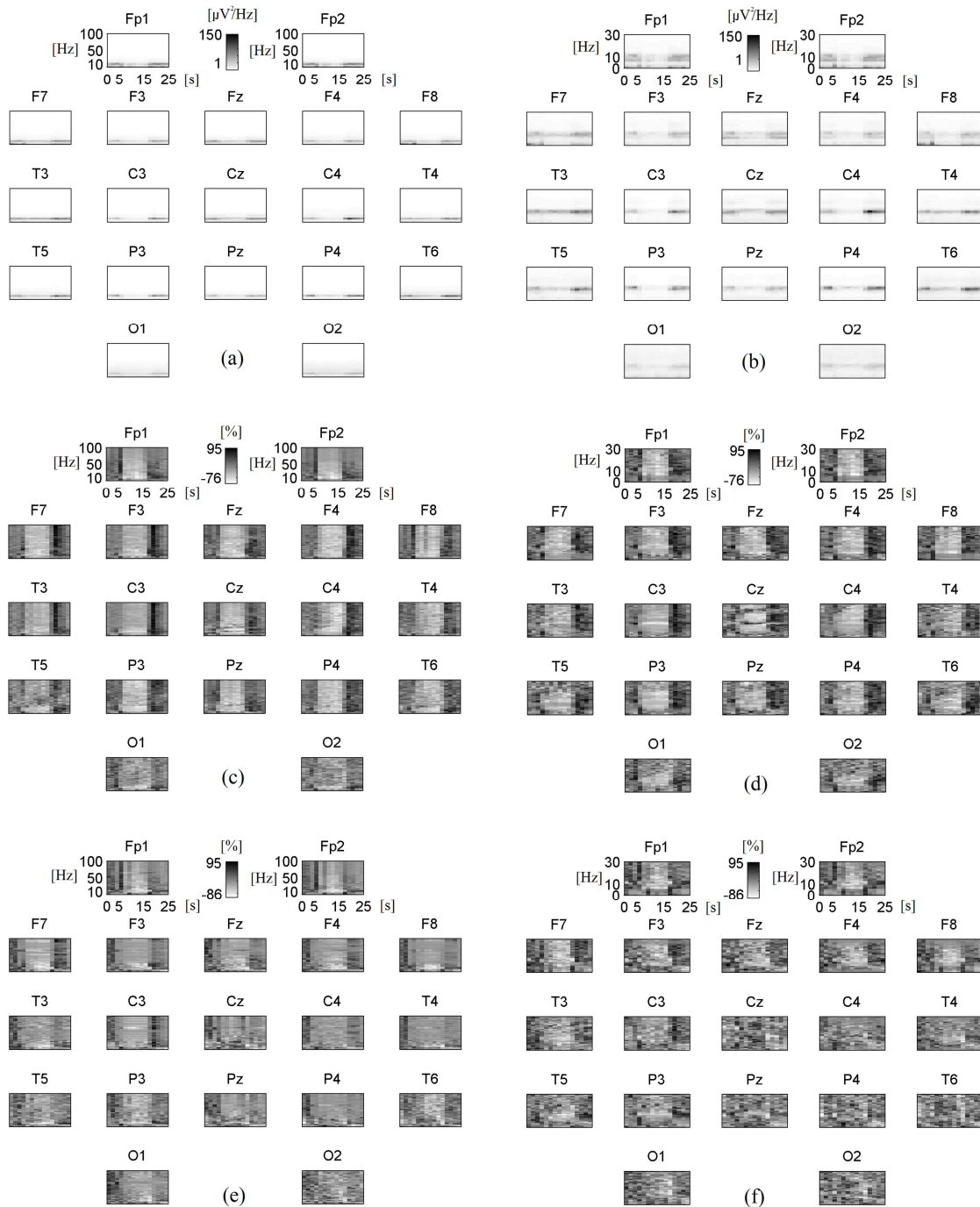


Figure 5.4 – (a) average periodogram during the mental task of rotation of a cube; (b) average periodogram during the mental task of rotation of a cube focused on the activity from 0 to 30 Hz; (c) average periodogram with relative amplitudes for the mental task of rotation of a cube; (d) average periodogram with relative amplitudes for the mental task of rotation of a cube focused on the activity from 0 to 30 Hz; (e) average periodogram with relative amplitudes for the mental task of music imagery; (f) average periodogram with relative amplitudes for the mental task of music imagery focused on the activity from 0 to 30 Hz.

### 5.5 Artifact removal techniques

In Chapter 3, the Figures 3.18, 3.19 and 3.20 exemplified the methods for discarding and minimizing artifacts. As BCI applications need an online usage of the ICA, the separating matrix  $\mathbf{W}$  (eq. 3.6) can be estimated during some training trials and used in later trials, and the processing time will only be due the matrix multiplication. The processing time of the techniques of artifact removal presented in section 3.6 was calculated in order to evaluate whether it is possible to adapt the algorithms to an online approach. The ICA algorithms used two training trials to estimate the separating matrix  $\mathbf{W}$  and the average processing time was calculated for the remaining 58 trials. As the threshold analysis and the filtering approach does not need training trials the average processing time was calculated for all 60 trials. In average, the threshold analysis took  $0.34 \pm 0.47 \mu s$ . The filtering approach spent  $187.6 \pm 7.47 ms$ . The “fastICA” algorithm spent  $1.0 \pm 0.18 ms$ , and the “runica” algorithm took  $3.6 \pm 0.61 ms$ .

Figure 5.5 shows the ERD/ERS of subject 1 obtained for channel C3 using 60 epochs during the mental task of imagination of cube rotation. The black line shows the ERD/ERS obtained without artifact removal, by only using the CAR method. The dark gray line shows the ERD/ERS obtained with “fastICA”, and the light gray line shows the ERD/ERS obtained with “runica”. It can be observed that “fastICA” provided a small improvement in the ERD/ERS amplitude. The ERS peak reached 163%, and by using “fastICA” it reached 186% while the ERD did not change. It can be seen that the “runica” worsened the ERD/ERS curve, and the ERS peak only reached 45%. The average result of applying fastICA during all mental tasks and subjects was an improvement of  $12.6 \pm 9.4\%$ . It means that, on average, the application of “fastICA” enhanced the EEG SNR slightly, so the ERS peak or the ERD depression was more detectably.

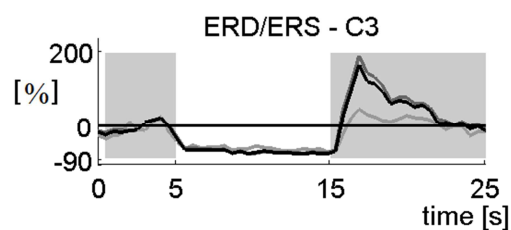


Figure 5.5 – ERD/ERS of channel C3 at  $\mu$  band. In black: ERD/ERS obtained without artifact removal; in dark gray: ERD/ERS obtained with “fastICA”; in light gray: ERD/ERS obtained with “runica”.

## 5.6 Sampling rate analysis

Regarding the sampling rate, the same ACF analysis discussed in section 4.2 was performed with new experiments. In this time, the EEG was acquired at a sampling rate of 400 Hz and subject 1 performed 20 trials of 10 s. In half of the trials the subject should actually move his index finger of the right hand; in the other half the subject should only imagine the movement of the index finger of the right hand. Simultaneously, the sEMG signal from the index finger was captured using a bipolar channel, in which one electrode was placed on top of the hand over the *Extensor indicis* and *Extensor digitorum communis* tendons, and the second electrode was placed on the wrist. The subject was instructed to sit with hands resting on the legs and observe a cross in the center of the screen. After 4 s an arrow replaces the cross indicating the start of the task. The task lasts 2 s, and then the cross reappears in place of the arrow, indicating that the mental task is over. The subject must remain still until the cross is replaced by a circle at the 10 s mark, indicating the end of the record.

During the experiment the hands were resting on the legs and the subject was instructed to slowly perform one extension of the index finger, from the 4 to the 6 s mark of the EEG record. For the imagination task the subject was instructed to slowly perform one imaginary extension of the index finger, from the 4 to the 6 s mark of the EEG record.

At the bottom left of the Figure 5.6 there is a signal representing the beginning and end of the task, and the average EMG from all 10 trials. The sEMG signal is not related to the scale of the figure. A slight delay of about 0.2 s can be noticed, which is due to the subject's reaction time between viewing the arrow and performing the effective finger extension. Another delay is found at the end of the task, where the sEMG activity lasts for approximately 1 second after the notification of the end of the task. The top left part of the figure shows the ERD/ERS calculated at the  $\mu$  and  $\beta$  bands of channel C3, in which the reference period was taken between to be 0 to 2 s. There is a 50% decrease of the  $\beta$  band energy during the finger extension and there is an increase of up to 110% after the task execution that characterizes the ERD/ERS pattern.

At the right of Figure 5.6 the average periodogram of the EEG from channel C3 using Hamming windows of 0.5 s overlapped by 20% is shown. The hatched area highlights the  $\mu$  band activity during the execution of the task, and even in the periodogram a decrease in the  $\mu$  band energy while performing the task can be noticed.



However, the  $\beta$  band does not present a clear ERD/ERS pattern, with the ERD/ERS only being observed in the average of this frequency interval.

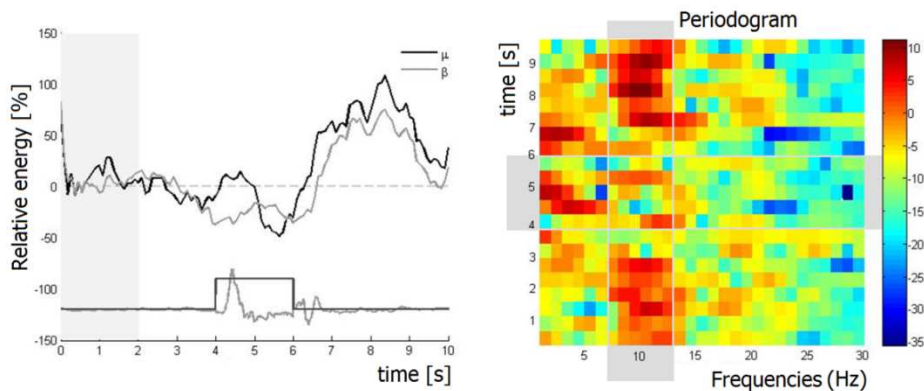


Figure 5.6 – Left: Relative energy of the  $\mu$  and  $\beta$  bands of channel C3. The reference period was taken between 0 and 2 s and the index finger extension occurred between 4 and 6 s; Right: Periodogram of channel C3.

Figure 5.7 was obtained with the task of imagination of movement of the index finger. At the bottom left of the Figure 5.7 there is a signal representing the beginning and end of the task and the average sEMG from all 10 trials. The sEMG signal is not related to the scale of the figure. It may be noticed that sEMG activity is random and does not present any particular feature or vestigial movement during the task interval. The lower horizontal line that almost coincides with the time axis corresponds to the sEMG activity scaled over the sEMG obtained during finger movement. This second sEMG is shown scaled to show that there is almost no myoelectric activity, and it is also shown enlarged so that it appears that the residual activity is seemingly random.

The top left part of the figure shows the ERD/ERS calculated at  $\mu$  and  $\beta$  bands of channel C3. There is a 45% decrease of the  $\beta$  band energy during the finger extension and an increase of up to 90% after the mental task execution that characterizes the ERD/ERS pattern. For the  $\mu$  band there is an increase of up to 180% after the mental task execution.

At the right of the Figure 5.7 the average periodogram of the EEG from channel C3 is shown. The hatched area highlights the  $\mu$  band activity during the execution of the task, and even in the periodogram a decrease in the  $\mu$  band energy while performing the task can be noticed. The energy decrease during the mental task extends to frequencies up to 20 Hz.

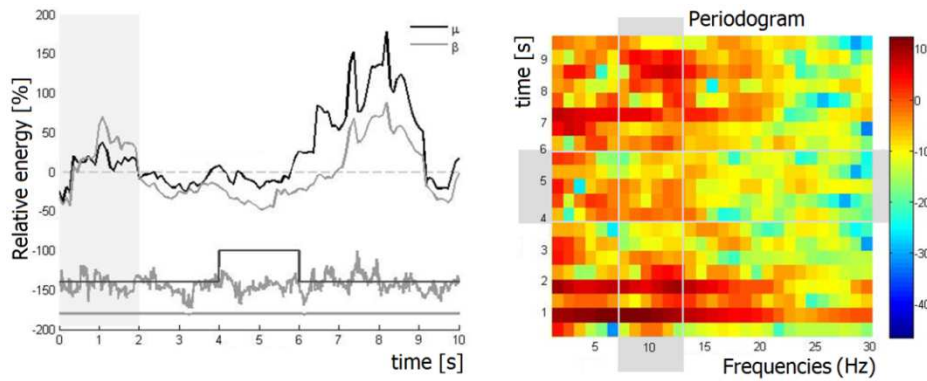


Figure 5.7 – Left: Relative energy of the  $\mu$  and  $\beta$  bands of channel C3. The reference period was taken between 0 and 2 s and the mental task occurred between 4 and 6 s; Right: Periodogram of channel C3.

Figure 5.8 - Left shows the average ACF result during the motor mental task. Figure 5.8 - Right shows the average ACF result during the non-motor mental task and both results are very similar. The first ACF minimum was obtained for 0.06 s ( $\tau_m$ ). Substituting the  $\tau_m$  into eq. 4.1, then,  $0.006 \leq T_s \leq 0.003$  or  $166.6 \text{ Hz} \leq F_s \leq 333.3 \text{ Hz}$ , and the result of the analysis is that the EEG should be sub-sampled to 256 Hz. This analysis corroborates the statement made in section 3.3 that the EEG could not have fundamental oscillation frequencies much higher than 100 Hz and that the sampling rate of 200 Hz should be enough for the observation of the main frequency bands ( $\alpha$ ,  $\beta$ ,  $\gamma$ ,  $\delta$ ,  $\mu$  and  $\theta$ ).

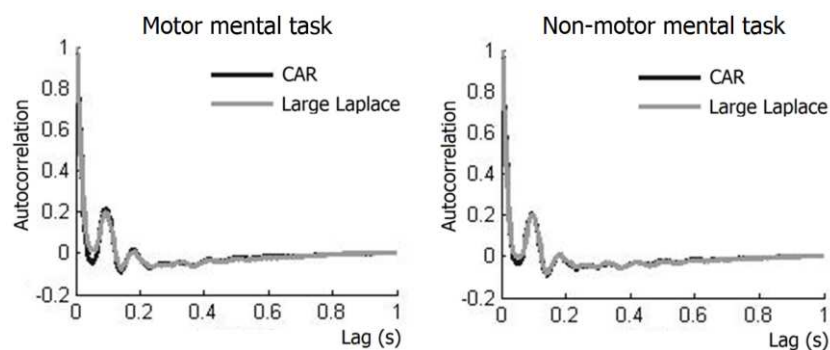


Figure 5.8 – Average ACF obtained during the motor mental task.

## 5.7 Stationarity analysis

Some characteristics of non-stationarity signals such as the mean, variance or power spectra can change with time. Then, the EEG time-windows used to calculate the PSD and also to estimate the mean and variance for the Bayesian classifier have to be at least WSS. If very small time-windows are used the random nature of EEG prevails and

different values of  $\mu$  and  $\sigma$  are obtained for each new window analyzed. On the other hand, large EEG time-windows, are avoided in real-time classification because it may result in large delays during the identification of class transitions. Then, the minimal size of time-windows in which the EEG can be considered stationary is estimated by using the KPSS and ADF tests.

Figure 5.9 shows the ongoing average,  $\mu$ , and standard deviation,  $\sigma$ , calculated for every new EEG sample until the end of the epoch, which is 25 s. But, this figure shows the superimposition of all channels and, it can be seen that when using few samples the values of  $\mu$  and  $\sigma$  tend to vary. While using larger time-windows the values of  $\mu$  and  $\sigma$  tend to be a constant. The left part of Figure 5.9 shows the ongoing average and standard deviation for the right hand imagery and it can be noticed that the values of  $\mu$  and  $\sigma$  of most channels tend to stabilize from 5 s onwards. The right part of Figure 5.9 shows the ongoing average and standard deviation for the sound imagery and it can be noticed that the values of  $\mu$  and  $\sigma$  of most channels also tend to stabilize from 5 s onwards. Then, Figure 5.9 shows that small time-windows of the EEG can be non-stationary as  $\mu$  and  $\sigma$  became unstable.

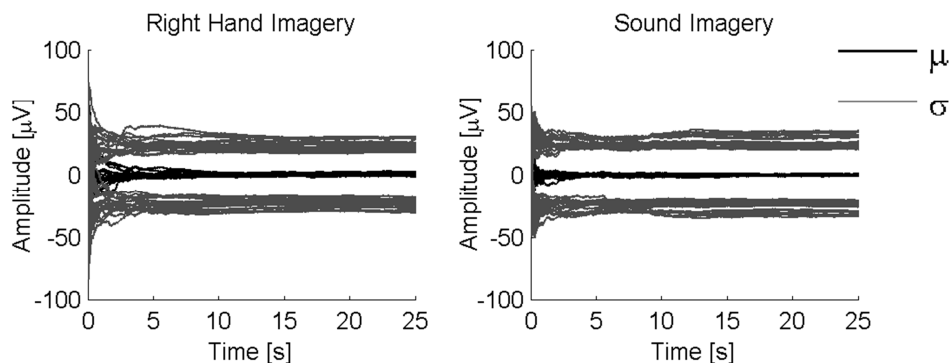


Figure 5.9 – Left: Ongoing average  $\mu$  and standard deviation  $\sigma$  calculated with time-windows up to 25 s during the right hand imagery task; Right: Ongoing average  $\mu$  and standard deviation  $\sigma$  calculated with time-windows up to 25 s during the sound imagery task.

The left of Figure 5.10 shows the average result of KPSS and ADF tests for the motor mental task of right hand imagery, and the right of Figure 5.10 shows these tests for the non-motor mental task of sound imagery. For the motor mental task, the p-value of the KPSS is higher than the significance level ( $\alpha$ ) of 5% for all lengths of time windows tested. Then, the null hypothesis that the signal is stationary can not be rejected. The ADF p-value is smaller than  $\alpha$  for time windows larger than 0.7 s, stating

that the null hypothesis that the signal is a non-stationary unit root process can be rejected for windows with duration larger than 0.7 s. By using the confirmatory analysis of KPSS and ADF tests, shown in table 4.1, the signal can only be considered trend stationary for windows larger than 0.7 s. The non-stationary interval is highlighted by the shaded area.

For the non-motor mental task, the KPSS p-value is higher than  $\alpha$  for all lengths of time windows tested, and the ADF p-value is smaller than  $\alpha$  for time windows larger than 0.7 s. By using the confirmatory analysis of KPSS and ADF tests the signal can only be considered trend stationary for windows larger than 0.7 s, which corresponds to approximately 140 samples, as the EEG signal was sampled at 200 Hz. The nearest power of two higher than 140 samples corresponds to 256 samples, therefore, time-windows with 256 samples are suggested for online processing, that is approximately 1.28 s. Finally, this analysis proposes that the time windows of 1.28 s should be stationary and can be used for the signal processing and feature extraction steps.

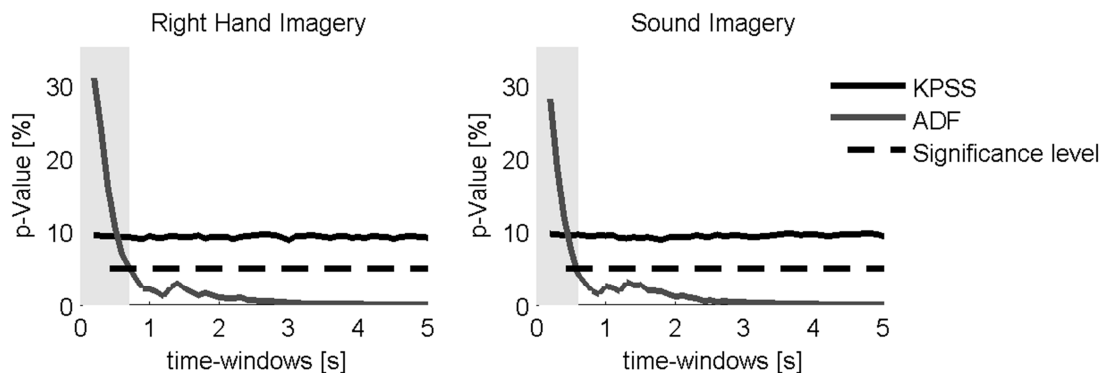


Figure 5.10 – Left: KPSS and ADF tests results for motor mental tasks; Right: KPSS and ADF tests results for non-motor mental tasks.

## 5.8 SNR analysis

As previously mentioned in section 3.7, the noise amplitude of the average of  $N$  trials is  $1/\sqrt{N}$  times that of a single trial, and the SNR of the EEG increases in approximate proportion to the number of trials (Luck, 2005). When dealing with the EEG signal it is very difficult to distinguish the noise component from the clean ERP signal. Therefore, making a realistic estimation of the ERP and the noise amplitudes in order to calculate the SNR improvement for each new added trial by using eq. 3.17 is complicated. Because of this we consider using the signal correlation that is strongly

related to the SNR (Borga, 1999). Let's consider the correlation between a signal  $x$  with this same signal corrupted with a noise  $n$ , where both are zero-mean and uncorrelated. Then, we have that the corrupted signal is given by  $y = x + n$ , and the correlation is

$$\begin{aligned}\rho_{x,y} &= \frac{E[(x - E[x]) \cdot (y - E[y])]}{\sqrt{E[x^2]} \cdot \sqrt{E[y^2]}} = \frac{E[(x) \cdot (x + n - E[x + n])]}{\sqrt{E[x^2]} \cdot \sqrt{E[(x + n)^2]}} \rightarrow \\ \rho_{x,y} &= \frac{E[(x) \cdot (x + n)]}{\sqrt{E[x^2]} \cdot \sqrt{E[x^2 + 2xn + n^2]}} = \frac{E[x^2] + E[xn]}{\sqrt{E[x^2]} \cdot (E[x^2] + E[2xn] + E[n^2])} \rightarrow \\ \rho_{x,y} &= \frac{E[x^2]}{\sqrt{E[x^2]} \cdot (E[x^2] + E[n^2])} = \frac{S}{\sqrt{S \cdot (S + N)}},\end{aligned}\quad (5.1)$$

where  $S$  is signal energy and  $N$  is the noise energy (Borga, 1999). Then, the SNR can be obtained from the correlation, by

$$\begin{aligned}\rho_{x,y}^2 &= \frac{S^2}{S \cdot (S + N)} \leftrightarrow \rho_{x,y}^2 \cdot (S + N) = S \leftrightarrow \rho_{x,y}^2 \cdot S + \rho_{x,y}^2 \cdot N - S = 0 \leftrightarrow \\ S \cdot (\rho_{x,y}^2 - 1) &= -\rho_{x,y}^2 \cdot N \leftrightarrow \frac{S}{N} = \frac{\rho_{x,y}^2}{1 - \rho_{x,y}^2}.\end{aligned}\quad (5.2)$$

An estimation of the EEG SNR was performed, using a comparison with the correlation between the ongoing average and the final ERD/ERS curve, and the correlation between a single trial and the ongoing average as well. This analysis was performed in order to estimate the number of epochs necessary to observe the ERD/ERS pattern during the mental tasks with two kinds of paradigms: the motor and non-motor related mental tasks. By comparing the SNR of the functional mental task of movement of the right hand with the proposed task of music imagery we can have a clue about how difficult it will be to perform the online processing of the feature extraction.

The noise amplitude approximately decreases in approximate proportion to the square root of the number of trials. An excessive number of trials then, will not cause meaningful changes in the observed ERD/ERS (Luck, 2005). In order to verify if the number of trials used to observe the ERD/ERS was enough or was excessive, the correlation between the ongoing average and the final ERD/ERS curve (C-1) was calculated for each new epoch, until reaching the total number of sixty epochs.

Equation 5.2 shows the relation between the SNR and the correlation for the specific case in which both signal and noise are uncorrelated. However, the assumption that the ongoing average is uncorrelated from the ERD/ERS curve is not true, therefore, eq. 3.41 can not be directly applied to find the ERP SNR. As a conservative approach, the rescaled correlation function was compared with the square root of the SNR by using a polynomial regression.

As a single epoch is quite different from the final averaged ERD/ERS curve obtained, the correlation must show small values at the beginning. As the ongoing average uses more epochs, the correlation increases, and, then, it finally converges, indicating that the difference between them is not meaningful. The left side of Figure 5.10 shows, in a black continuous line, the correlation C-1 of channel C3 obtained for the right hand mental task. From 30 epochs forth, the correlation reaches 95% and the ERD/ERS curve obtained at this point is very similar to the ERD/ERS curve obtained by using the total amount of 60 epochs.

Also, the correlation between a single trial and the ongoing average (C-2) was calculated. As a single epoch is very similar to the initial ongoing average, the correlation must show high values at the beginning. As the ongoing average uses more epochs, the correlation decreases, and, then, it converges, indicating that the difference between them is not meaningful. Figure 5.11 - Left shows, in a gray continuous line, the correlation C-2. In this curve, from 30 epochs forth, the correlation reaches 16%, and when using the total amount of epochs it decreases only 2%.

Finally, the gray dashed line in Figure 5.11 shows the square root of the SNR as more epochs are considered and it is related to the right vertical axis. The correlation curve, C-1, was divided into two parts, from the first epoch to an epoch  $n$ , and from  $n$  to the end of C-1. Then, two polynomial regressions were performed for each part of C-1 using functions of the type  $f(n) = c \cdot (n)^a$ , where  $c$  is a scale parameter. The right part of Figure 5.11 shows in the black line the  $a$  value of the first part of C-1, as  $n$  varied. It can be seen that from 7 to 11 epochs the  $a$  value is quite close to the noise amplitude decrease, or the square root of the SNR (that is 0.5).

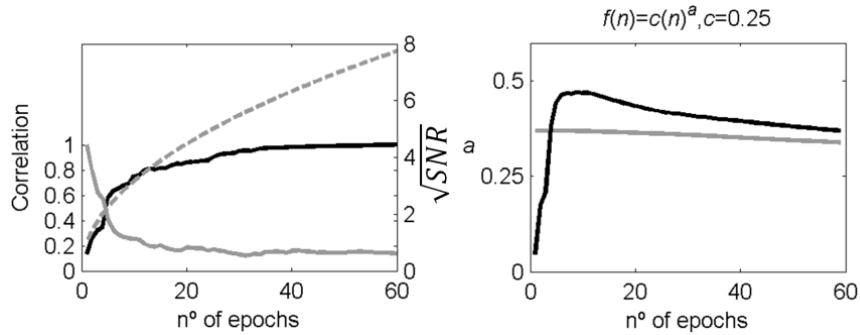


Figure 5.11 –Left: Mental task of right hand. The correlation curve, C-1, of channel C3 is shown by the black continuous line. The correlation curve, C-2, of channel C3 is shown by the gray continuous line. The square root of the SNR curve is shown by the gray dashed line, whose vertical axis is on the right side; Right: The  $a$  value of the first part of C-1 is shown by the black line. The  $a$  value of the second part of C-1 is shown by the gray line.

The right part of Figure 5.12 shows on the gray line the  $a$  value of the second part of C-1, as  $n$  varies. The  $a$  value obtained from 11 to 60 epochs, corresponds to  $a = 0.34$ , which means approximately that  $f(n) = \sqrt[3]{n}$ . This indicates that only for the first 10 epochs, where C-1 reaches 80%, does the information increase similarly to the square root of the SNR curve. Most of the information about the ERD/ERS pattern then is already retained with just 10 epochs.

The correlations C-1 and C-2 were also performed for the mental task of music imagery. Figure 5.12 shows, in the black continuous line, the correlation C-1 of channel T5 that is over the auditory cortex on the temporal lobe of the left brain hemisphere. From 53 epochs forth, the correlation reaches 95%, and the ERD/ERS curve obtained at this point is very similar to the ERD/ERS curve obtained by using the total amount of 80 epochs. The curve seems to converge from 50 epochs forth.

In Figure 5.12 the gray dashed line shows the square root of the SNR curve that was scaled in order to cross C-1 at 50 epochs. The initial part of C-1, from 1 to 50 epochs, is very similar to the square root of the SNR function and, after rescaling, the same aforementioned polynomial fit was performed for this part of C-1, in which  $a$  obtained a value of 0.49, which is very close to the value of the curve. The end part of C-1, from 51 to 80 epochs, obtained  $a = 0.46$ . This small decrease of the exponent  $a$ , in relation to the decrease obtained for the right hand mental task, is due to the small amount of samples representing the convergent portion of C-1.

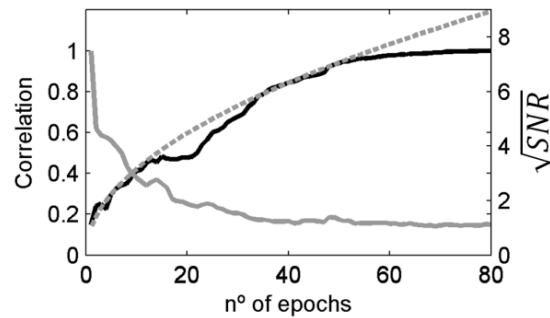


Figure 5.12 – Mental task of music imagery. The correlation curve, C-1, of channel T5 is shown by the black continuous line. The correlation curve, C-2, of channel T5 is shown by the gray continuous line. The square root of the SNR curve is shown by the gray dashed line, whose vertical axis is on the right side.

Even without absolute values for the ERP SNR of motor and non-motor mental tasks, this correlation analysis leads to the conclusion that the mental task of sound imagery should need approximately five times more epochs than the motor related mental task in order to observe the ERD/ERS pattern. We do not intend to make physiological assumptions about the strength of the desynchronization or later synchronization of the neural mass recruited for the mental task of music imagery. However, it is known that electrodes at temporal (T3, T4, T5 and T6) and lateral-frontal sites (F7 and F8) are particularly affected by facial muscle artifacts from tension or jaw movements (Davidson et al., 2000). In general, frontal and temporal electrodes are more heavily contaminated by artifacts than central scalp channels (Jung et al., 2000). Thus, the SNR of these electrodes should be lower than the SNR from electrodes at central sites and more epochs are needed to observe the ERD/ERS pattern.

The convergent portion of C-1 for the right hand mental task had 50 samples while the convergent portion of C-1 for the mental task of sound imagery had 30 samples. Then, 20 new samples were estimated for the convergent portion of C-1 by using general polynomial regression. The new C-1 convergent portion of the mental task of sound imagery, with 50 samples, obtained a  $a = 0.38$ , which is very close to the exponent value obtained for the right hand mental task. Then, after C-1 convergence, the information enhancement gradually decreases for both mental tasks, in a quite similar way.



## Chapter 6 : Conclusion

As described in Chapter 1, BCIs can be understood as the union of two main processes that are the signal acquisition and the signal processing (Figure 6.1). Regarding the signal acquisition the sampling rate analysis shown in section 5.6 concluded that the sampling rate of 200 Hz should be enough for the observation of the main features of the EEG, which lie in the frequency bands  $\alpha$ ,  $\beta$ ,  $\gamma$ ,  $\delta$ ,  $\mu$  and  $\theta$ . This analysis also corroborates the statement made in section 3.3 that the EEG could not have fundamental oscillation frequencies much higher than 100 Hz.

If very small time-windows are used the random nature of EEG prevails as the stationarity analysis shown in section 5.7 concluded that the EEG can only be considered trend stationary for windows larger than 0.7 s. On the other hand, large EEG time-windows, are avoided in real-time classification because it may result in large delays during the identification of class transitions. Therefore, time windows with 1.28 s, or 256 samples are suggested.

Regarding the signal pre-processing, the CAR spatial filter is suggested in association with the “fastICA” algorithm that took  $1.0 \pm 0.18$  ms and resulted in an improvement of  $12.6 \pm 9.4\%$  in the ERD/ERS. At a sampling rate of 200 Hz, there is a new sample every 5 ms, and time windows of 1 s displaced at no less than 10 ms could be used. Then, the system would have a classification rate of 100 Hz with no lag and it could be implemented online in BCI applications running minimally in our aforementioned requirements.

Regarding the feature extraction, the EEG features are the PSD frequency components obtained over stationary time windows of 256 samples shifted for every two samples. As shown in section 4.5, the feature selection suggested is the K-L symmetric divergence associated with the threshold analysis that adapts the Bayesian classifier with linear discriminant function for a non-supervised training step. This approach makes the classifier independent of the chosen mental task paradigm and also would adapt the BCI for individual features of the user.

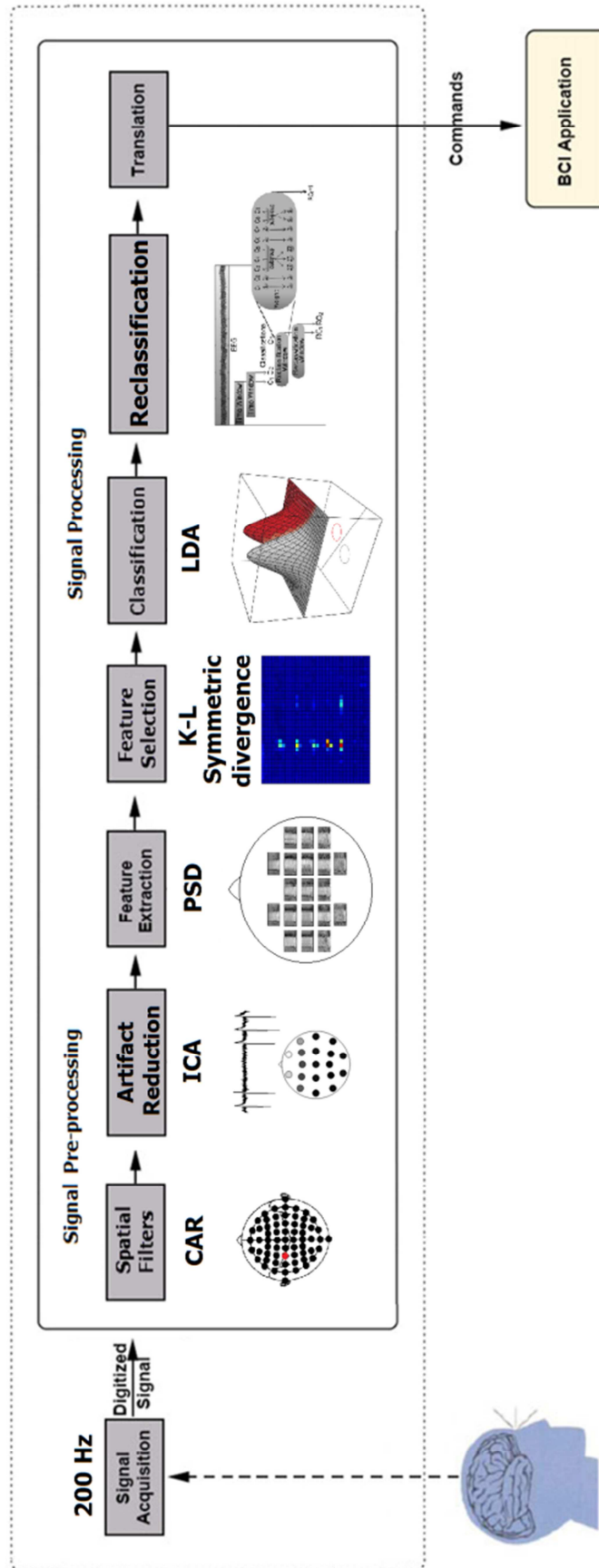


Figure 6.1 – BCI schematic flow chart proposed in this Ph.D. Thesis.

The simulated results shown in table 4.2 are compared in table 4.4 with the results obtained in BCI competition III. The results of the proposed method are on average 16.3% better than those of the best work obtained in BCI competition III. By using fixed reclassification windows of 0.5 s, our results are on average 4.3% better than the best work obtained in BCI competition III. These results support the view that this proposal for the BCI could be implemented successfully, achieving success rates higher than those obtained in BCI competition III. Figure 6.1 shows the overall schematic flow chart of the proposed BCI.

The training process of the classifier and the feature selection method can start after some seconds of EEG acquisition for each mental task, almost without training. However, by using a training time so small it is not expected that the classifier set the correct class. But, after several sessions of training the classifier should start to set the classes with the advantage that the user can observe the improvement of the accuracy rate of the classifier throughout the process of training.

Regarding the possibility of extending our BCI to operate with both, motor and music imagery paradigms, five mental tasks were studied. Before introducing a new mental task into a BCI, it should be analyzed to see if it provides enough and distinct enough information to be classified, at least offline. The main features that allow the identification of a mental task are the physiological effects that culminate in desynchronization and synchronization of the related neuronal masses. As distinct mental tasks activate different brain areas, the ERD/ERS pattern obtained over the scalp should vary related to the mental task.

From the ERD/ERS scalp maps of Figure 5.3 it is very difficult to assign a source for the spread ERD/ERS activity observed in the scalp. In the average technique, the time-locked activity is stressed as the spontaneous activity decreases, however, the cortical electrical activity spreads until it can be measured by electrodes on the scalp. Then, during the average process other scalp areas that do not have time-locked activity to the event may present a remnant of the original spread time-locked activity. Then, a naive approach is to assign the source of the ERD/ERS to the site where the highest activity occurs.

As it can be seen in Figure 5.3 - B, during the mental task of imagination of movement of the right hand the higher ERD/ERS activity occurs in electrodes C3 and P3. Then, it might be supposed that this activity represents the activation of areas related to the right hand in motor cortex, and that activity has spread to the neighboring

electrodes F7, F3, Fz, T3, Cz, T5 and Pz. However, for mental tasks whose activation areas were not fully mapped, this assumption could be wrong, since the activity measured in these electrodes may also be due to some time-locked activity of local small generators yielding a lower amplitude ERD/ERS.

Even though a specific source can not be assigned for the spread observed ERD/ERS pattern obtained for all the motor mental tasks, the ERD/ERS scalp maps obtained for the sound imagery have a less spread pattern over the scalp. The sound imagery ERD/ERS activity was observed in the  $\alpha/\mu$  band over temporal sites (T3, T4 and T5), lateral-frontal sites (F7 and F8) and the parietal electrode P3. The electrodes T3 and T4 are located approximately over the auditory cortex (Brodmann areas 41 and 42) on the temporal lobe. The electrodes T5 and P3 are located approximately over the Wernicke area (Brodmann areas 39 and 40) on the temporal/parietal lobe. And the electrode F7 is located over the Broca's area (Brodmann areas 44 and 45) on frontal lobe (Bear et al., 2008).

The ERD observed in electrodes T3 and T4 indicates that the auditory cortex of both brain hemispheres was activated. Wernicke's area and Broca's area are related to information comprehension, language processing and speech production, and they are present in the dominant cerebral hemisphere, which is the left hemisphere in about 97% of people (Bear et al., 2008). Then, the activity observed in electrodes T5 and P3, over the left hemisphere, is strongly related to the Wernicke's area as no similar activity was observed over electrodes T6 and P4, over the right hemisphere. The activity shown on electrode F7 may be due to the activation of Broca's area.

Also, the activity measured on electrodes F7 and F8 could be merely due to the spreading of an ERD occurring at electrodes T3 and T4, over the auditory cortex. However, this is a very cautious approach, since if the ERD had originated beneath the electrode T4, it would have spread radially, also reaching the electrodes T6 and C4. The same occurred for the electrode T3, in which the near electrode C3 did not present an ERD. It is also important to note that even using a mental task in which the subjects were instructed to remember just instrumental music, with no lyrics, some brain areas related to language and speech were supposedly activated.

The ERD was also observed with smaller amplitude in frontal sites (F3, Fz and F4) that could be due to the spread of the ERD pattern during the average process. Also, it could be due to a local desynchronization on frontal lobe related to the state of attention to the beginning of the mental task. In general, for all analyzed mental tasks,

an ERD with smaller amplitude was always present in electrodes of frontal lobe (Fp1, Fp2, F3, Fz and F4). Then, the above mentioned statement about the frontal ERD being related to the state of attention can be applied to the ERD/ERS scalp maps obtained for all mental tasks.

Also, almost no ERD/ERS activity was observed on electrodes O1 and O2, for all the mental tasks here analyzed. The electrodes O1 and O2 are over the occipital lobe, which is related to visual processing, and so this absence of activity was expected during the mental tasks. Also, considering the spread of the EEG, these electrodes were less affected by the activity of other nearby brain lobes.

The spectrograms of Figure 5.4 (A, B) show that the frequency band with the highest absolute energy variation was the  $\alpha/\mu$  band. The spectrograms of Figure 5.4 (C, D, E and F) show that the ERD/ERS pattern occurs spread over all analyzed frequencies, and any mental task impelled a desynchronization/synchronization of a specifically narrow high frequency band.

Although the ERD/ERS could be measured even for frequencies near 100 Hz, with percentage variations of just 16.89 % lower than for 10 Hz, in absolute amplitudes the energy variation at 100 Hz was approximately one thousand times lower than for 10 Hz. This decrease of energy at high frequencies is caused by the low electrical conductivity of the skull, acting as a low pass filter (Davidson, et al., 2000; Tang, et al., 2008).

In order to estimate the number of epochs necessary to observe the ERD/ERS pattern, we suggest an analysis of the EEG SNR by using a comparison with the correlation between the ongoing average and the final ERD/ERS curve and also the correlation between a single trial and the ongoing average. The comparison was endorsed by using a polynomial regression that showed similarities between the exponents of the curves. Then, we suggest a minimal amount of 10 epochs for observing the ERD/ERS pattern during motor mental tasks and 50 epochs for the sound imagery task. And we concluded that the mental task of sound imagery should need approximately five times more epochs than the motor related mental task in order to observe the ERD/ERS pattern.

Although the correlation curves of the mental tasks analyzed converged at different points, indicating different amounts of epochs to achieve the same quality of information, the decrease of the information enhancement after the convergence is approximately similar for both mental tasks. Then, we can assert that for the motor and

non-motor related mental tasks analyzed, the correlation curve behavior, until it reaches the convergence, is similar to the SNR enhancement function. And after the convergence point the behavior of the correlation curve is similar for both kinds of mental tasks studied.

The ERD/ERS scalp maps of Figure 5.3 show that there is a little difference between the scalp maps from the mental task of right and left hand movement imagery. The main difference between the mental task of imagination of movement of both feet and those hand related mental tasks is the amplitude of the ERS that occur in the electrode C3 and P3. The main difference between the mental task of rotation of a cube and the imagination of movement of both feet is the ERS at the  $\mu$  band, occurring in both electrodes C3 and C4. And the main difference between the sound imagery task and the motor-related mental tasks is the absence of ERD at the  $\mu$  band in electrodes of the central area (C3, Cz and C4). During the sound imagery task we believe that the auditory cortex of both brain hemispheres was activated, followed by the activation of Wernicke's area and Broca's area.

Since it is not known, a priori, which bands of frequencies present useful information during the task of music imagery, the spectrograms of the EEG during all aforementioned mental tasks were calculated in absolute amplitudes and also in percentage values relative to the mean activity of each frequency over the time. The spectrograms of Figure 5.4 show that the ERD/ERS could be measured even for frequencies near 100 Hz, but in absolute amplitudes the energy variation at 100 Hz was approximately one thousand times smaller than for 10 Hz. Even if the ERD/ERS pattern could be measured for high frequencies by using a large number of epochs, if it presents a very small amount of energy the probability of being measured online for BCI applications will be low. Then, most of the useful information for online processing and BCIs corresponds to the  $\alpha/\mu$  band.

Finally, concluding this analysis, although there is a measurable difference in the ERD/ERS scalp map of the sound imagery task and the motor-related mental tasks at the  $\alpha/\mu$  band, the low SNR of the sound imagery task could be a problem during the online processing and pattern recognition for BCI usage.

Further studies are necessary to investigate the Information Transfer Rate (ITR) during the online classification of sound imagery (Obermaier, et al., 2001). As the mental task of sound imagery should need approximately five times more epochs than the motor related mental task in order to observe the same ERD/ERS pattern, it is very

likely that the ITR should be approximately five times lower than for motor-related mental tasks.

It is worth to comment that from the studies conducted during this Ph.D. Thesis, the following publications were realized:

Journal articles:

1. **Benevides, A. B.**, Bastos, T. F., & Sarcinelli, M. S. Pseudo-Online Classification of Mental Tasks Using Kullback-Leibler Symmetric Divergence. In: *Journal of Medical and Biological Engineering*, 2012, 32(6): 411-416. ISSN 1609-0985. doi: 10.5405/jmbe.926.
2. **Benevides, A. B.**, Atencio, A. C., Bastos, T. F., & Sarcinelli, M. S. Study of Motor and non-Motor Related Mental Tasks for Application in Brain-Computer Interfaces (in Portuguese). In: *Medical Journal of Minas Gerais*, 2012, 22(6): 130. ISSN: 0103-880X.
3. Atencio, A. C., Ferreira, A., **Benevides, A. B.**, Bastos, T. F., Menezes, M. L., & Pereira, C. Evaluation of HOC Statistics Features of EEG Signals Applied to the Recognition of Emotional States (in Portuguese). In: *Medical Journal of Minas Gerais*, 2012, 22(6): 131. ISSN: 0103-880X.
4. **Benevides, A. B.**, Bastos, T. F., & Sarcinelli, M. S. Design of a General Brain-Computer Interface. In: *Control & Automation Journal*, 2011, 22(6): 638-646. ISSN 0103-1759.

Full papers in international conferences:

1. Atencio, A. C., **Benevides, A. B.**, Bastos, T. F., Ferreira, A. EEG Evaluation During Emotional State Elicited by Unpleasant Sounds to be Applied in BCI. In: *International Brain-Computer Interface Meeting*, 2013, California, United States, 166:167. doi: 10.3217/978-3-85125-260-6-84
2. Atencio, A. C., Bastos, T. F., Ferreira, A., & **Benevides, A. B.** Evaluation of ERD/ERS Caused by Unpleasant Sounds to be Applied in BCIs. In: *4th IEEE Biosignals and Biorobotics conference (ISSNIP)*, 2013, Rio de Janeiro. *Proceedings of the 4th IEEE Biosignals and Biorobotics conference (ISSNIP)*, 2013. p. 1-5. doi: 10.1109/BRC.2013.6487533
3. Sarmiento, J. F., Romero, D., Bastos, T. F., **Benevides, A. B.**, & Silva, I. V. Identification the Limit of Conscious Perception of Surface EEG Signals with

- Visual Evoked Potentials. In: 3rd IEEE Biosignals and Biorobotics conference (ISSNIP), 2012, Manaus, Brazil. Proceedings of the 3rd IEEE Biosignals and Biorobotics conference, 182-186. doi: 10.1109/BRC.2012.6222161
4. Sarmiento, J. F., Tello, R., **Benevides, A. B.**, Bastos, T. F., & Kumar, D. K. Capture Protocol Forearm sEMG Signals with Four Channels and Healthy and Amputee People. In: 3rd IEEE Biosignals and Biorobotics conference (ISSNIP), 2012, Manaus, Brazil. Proceedings of the 3rd IEEE Biosignals and Biorobotics conference, 178-181. doi: 10.1109/BRC.2012.6222162
  5. Sarmiento, J. F., Bastos, T. F., **Benevides, A. B.**, Elias, A., Frizzera-Neto, A., Moreira, M. H., & Silva, I. V. Characterization and Diagnosis of Fibromyalgia Based on Fatigue Analysis with sEMG Signals. In: 3rd IEEE Biosignals and Biorobotics conference (ISSNIP), 2012, Manaus, Brazil. Proceedings of the 3rd IEEE Biosignals and Biorobotics conference, 192. doi: 10.1109/BRC.2012.6222159
  6. **Benevides, A. B.**, Bastos, T. F., & Sarcinelli, M. S. A Pseudo-Online Brain-Computer Interface with Automatic Choice for EEG Channel and Frequency. In: The IEEE International Symposium on Circuits and Systems, 2011, Rio de Janeiro, Brazil. Proceedings of The IEEE International Symposium on Circuits and Systems, 81-84. doi: 10.1109/ISCAS.2011.5937506
  7. **Benevides, A. B.**, Bastos, T. F., & Sarcinelli, M. S. Proposal of Brain-Computer Interface Architecture to Command a Robotic Wheelchair. In: 20th IEEE International Symposium on Industrial Electronics, 2011, Gdansk, Poland. Proceedings of The 20th IEEE International Symposium on Industrial Electronics. doi: 10.1109/ISIE.2011.5984511
  8. Bastos, T. F., Müller, S. M. T., **Benevides, A. B.**, & Sarcinelli, M. S. Robotic Wheelchair Commanded by SSVEP, Motor Imagery and Word Generation. In: 33rd Annual International Conference of the IEEE Engineering in Medicine, 2011, Boston. Proceedings of the 33rd Annual International Conference of the IEEE Engineering in Medicine & Biology Society, 4753-4756. doi: 10.1109/IEMBS.2011.6091177
  9. **Benevides, A. B.**, Bastos, T. F. & Sarcinelli, M. S. Pseudo-Online Classification of Mental Tasks. In: 2nd IEEE Biosignals and Biorobotics Conference (ISSNIP), 2011, Vitória, Brazil. Proceeding of Biosignals and Biorobotics Conference. doi:10.1109/BRC.2011.5740659



10. Sarmiento, J. F., **Benevides, A. B.**, Moreira, M. H., Elias, A., Bastos, T. F., Silva, I. V., & Pelegrina, C. C. Comparative Muscle Study Fatigue with sEMG Signals During the Isotonic and Isometric Tasks for Diagnostics Purposes. In: 33rd Annual International Conference of the IEEE Engineering in Medicine, 2011, Boston. Proceedings of the 33rd Annual International Conference of the IEEE Engineering in Medicine & Biology Society, 7163-7166. doi: 10.1109/IEMBS.2011.6091810

Full papers in regional conferences and symposia:

1. **Benevides, A. B.**, Bastos, T. F., & Sarcinelli, M. S. Comparison of Artifact Removal Techniques on Single-trial Event-related Potentials for use in Brain-Computer Interfaces. In: XI Brazilian Symposium on Intelligent Automation, 2013, Fortaleza, Brazil.
2. **Benevides, A. B.**, Bastos, T. F., & Sarcinelli, M. S. Study of Motor Mental Tasks for Application in Brain-Computer Interfaces (in Portuguese). In: XIX Brazilian Congress on Automatic, 2012, Campina Grande, Brazil. Proceedings of the XIX Brazilian Congress on Automatic, 519-526.
3. **Benevides, A. B.**, Bastos, T. F., & Sarcinelli, M. S. Classification of Mental Tasks Using the Pseudo-Online Technique (in Spanish). In: VI Iberoamerican Congress on Technology Disability Support (IBERDISCAP), 2011, Palma de Mallorca, Spain. Proceedings of the VI Iberoamerican Congress on Technology Disability Support.
4. **Benevides, A. B.**, Bastos, T. F., & Sarcinelli, M. S. Classificação Pseudo-Online de Tarefas Mentais para uma Interface Cérebro-Computador (in Portuguese). In: X Brazilian Symposium on Intelligent Automation, 2011, São João Del-Rei, Brazil. Proceedings of the X Brazilian Symposium on Intelligent Automation, 199-204.
5. **Benevides, A. B.**, Bastos, T. F., & Sarcinelli, M. S. Parameter Selection for Real Time Classification of Mental Tasks (in Spanish). In: CEA Bioengineering Symposium, 2010, Málaga, Spain. Proceedings of the CEA Bioengineering Symposium, 2010. p. 73-79.
6. **Benevides, A. B.**, Bastos, T. F., Garcia, R. C., & Martín, J. L. Real Time Mental Tasks Classification to Control Robotic Devices (in Portuguese). In: XVIII

Brazilian Congress on Automatic, 2010, Bonito, Brazil. Proceedings of the XVIII Brazilian Congress on Automatic, 2010, 6-6.

## References

- Aguirre, L. A. (1995). "A Nonlinear Correlation Function for Selecting the Delay Time in Dynamical Reconstructions". *Physics Letters A*, 203: 88-94.
- Anderson, C. W; Knight, J. N; Kirby, J. M. and Hundley, D. G (2007). "Classification of Time-Embedded EEG using short-time principal component analysis". In: Dornhege, G; Millán, J. M; Hinterberger, T; McFarland, D. J e Müller, K. R. *Toward Brain-Computer Interfacing*. Cambridge: The MIT Press, 261-278.
- Araújo, D. B; Carneiro A. A. O. and Baffa, O (2004). "Localizando a atividade cerebral via magnetoencefalografia". *Ciência e Cultura*, 56(1): 38-40.
- Azevedo, A. P (2005). "Estudo do Sinal Eléctroencefalográfico (EEG) Aplicado a Interfaces Cérebro Computador com uma Abordagem de Reconhecimento de Padrões". Masters Dissertation. Federal University of Espírito Santo.
- Bear, M. F; Connors, B. W. and Paradiso, M. A (2008). *Neurociências: Desvendando o Sistema Nervoso*. Terceira edição. Editora Artmed® S. A., São Paulo, Brasil.
- Blanco, S; Garcia, H; Quian-Quiroga, R; Romanelli, L. and Rosso, O. A (1995). Stationarity of the EEG Series. *IEEE in Medicine and Biology*, 14:395-399.
- Beisteiner, R; Höllinger, P; Lindinger, G; Lang, W. and Berthoz, A (1995). "Mental Representations of Movements. Brain Potentials Associated with Imagination of Hand Movements", Elsevier, *Electroencephalography and Clinical Neurophysiology*, 96: 183-193.
- Bell, A. J; Sejnowski, T. J (1995). "An information-maximization approach to blind separation and blind deconvolution". *Neural computation*, 7:1129-1159.
- Benevides, A. B (2007). "Classificação de Padrões Mentais via Redes Neurais Artificiais e Transformada Wavelet". Undergraduate Thesis. Federal University of Espírito Santo.
- Benevides, A. B (2009). "Proposta de um Modelo de Fontes Cerebrais para Classificação de Padrões Mentais". Masters Dissertation. Federal University of Espírito Santo.
- Benevides, A. B; Bastos, T. F e Garcia, J. C (2010a). "Classificação de Tarefas Mentais em Tempo Real para Aplicação de Controle de Dispositivos Robóticos". *Anais do XVIII Congresso Brasileiro de Automática*, Bonito, Brazil, 2283-2289.
- Benevides, A. B; Bastos, T. F. e Sarcinelli, M (2010b). "Selección de Parámetros para Clasificación de Tareas Mentales en Tiempo Real". *Libro de Actas del Simposio CEA de Bioingeniería*, 68-74.

- Benevides, A. B; Bastos, T. F. e Sarcinelli, M (2011a). "Pseudo-Online Classification of Mental Tasks". *Proceedings of IEEE Computer Society ISSNIP*.
- Benevides, A. B; Bastos, T. F. e Sarcinelli, M (2011b). "Classificação Pseudo-Online de Tarefas Mentais para uma Interface Cérebro-Computador". *Anais do X Simpósio Brasileiro de Automação Inteligente*, 199-204.
- Benevides, A. B; Bastos, T. F. e Sarcinelli, M (2011c). "Clasificación Pseudo-Online de Tareas Mentales". *Memorias del VI Congreso Iberoamericano de Tecnologías de Apoyo a la Discapacidad*.
- Benevides, A. B; Bastos, T. F. e Sarcinelli, M (2011d). "A Pseudo-Online Brain-Computer Interface with Automatic Choice for EEG Channel and Frequency". *Proceedings of The IEEE International Symposium on Circuits and Systems*, 81-84.
- Benevides, A. B; Bastos, T. F. e Sarcinelli, M (2011e). "Proposal of Brain-Computer Interface Architecture to Command a Robotic Wheelchair". *Proceedings of The 20th IEEE International Symposium on Industrial Electronics*.
- Benevides, A. B; Bastos, T. F. e Sarcinelli, M (2011f). "Design of a General Brain-Computer Interface". *Revista Controle & Automação*, 22(6): 638-646.
- Benevides, A. B; Bastos, T. F. e Sarcinelli, M (2012a). "Pseudo-Online Classification of Mental Tasks Using Kullback-Leibler Symmetric Divergence". *Journal of Medical and Biological Engineering*, 32(6): 411-416.
- Benevides, A. B; Bastos, T. F. e Sarcinelli, M (2012b). "Estudos de tarefas mentais motoras para aplicação em interfaces cérebro-computador". *Anais do XIX Congresso Brasileiro de Automática*, Campina Grande, Brazil, 6-6.
- Benevides, A. B; Cotrina-Atencio, A; Bastos, T. F. e Sarcinelli, M (2012c). "Estudos de tarefas mentais motoras e não-motoras para aplicação em interfaces cérebro-computador". *Revista Médica de Minas Gerais*, 22(6): 130.
- Benevides, A. B. [Alessander] and Benevides, A. B. [Alessandro]. An ethernet sniffer for BrainNet36<sup>®</sup>. Available in: <http://sourceforge.net/projects/brainnet36-ethernet-sniffer/>. Accessed on: October 30, 2013.
- Bianchi, A. M; Leocani, L; Mainardi, L. T; Comi, G. and Cerutti, S. "Time-Frequency Analysis of Event-Related Brain Potentials" (1998). *Proceedings of the 20th Annual International Conference of the IEEE Engineering in Medicine and Biology Society*, 20(3): 1486-1489.
- Böcker, K. B. E; van Avermaete, J. A. G. and van den Berg-lenssen, M. M. C (1994). The International 10-20 System Revised: Cartesian and Spherical Coordinates. *Brain Topography*, 6: 231-235.
- Blanco, S; Garcia, H; Quian, R. Q; Romanelli, L. and Rosso, O. A (1995). "Stationarity of the EEG Series", *IEEE Engineering in Medicine and Biology*, 395-399.

- Blankertz, B; Dornhege G; Lemm S; Krauledat, M; Curio, G. and Müller, K. R (2007). "The Berlin Brain-Computer Interface: Machine Learning Based Detection of User Specific Brain States". In: Dornhege, G; Millán, J. M; Hinterberger, T; McFarland, D. J and Müller, K. R., eds. 2007. *Toward Brain-Computer Interfacing*. Cambridge: The MIT Press, 85-102.
- Borga, M (1999). Relation to SNR. Available in: <http://www.imt.liu.se/~magnus/cca/tutorial/node10.html>. Linköpings University, Department of Medical Technology, Sweden. Accessed on: July 15, 2013.
- BrainNet - BNT36 User's manual (2004). LYNX Tecnologia Eletrônica LTDA.
- Cheeín, F. A. A (2005). "Diseño de una Interfase Cerebro-computadora para la Navegación de Robots Móviles". Masters Dissertation. Universidad Nacional de San Juan, Argentina.
- Cincotti, F; Mattia, D; Aloise, F; Bufalari, S; Astolfi, L; Fallani, F; Tocci, A; Bianchi, L; Marciari, M; Gao, S; Millán, J. and Babiloni, F (2008). "High-resolution EEG techniques for brain-computer interface applications". *Journal of Neuroscience Methods*, 167: 31-42.
- Claffey, M (2013). Notes: Vision. Available in: <http://mikeclaffey.com/psyc170/notes/notes-vision.html>. Accessed on: July 15, 2013.
- Croft, R. J. e Barry, R. J (2000). "Removal of ocular artifact from the EEG: a review". *Clinical Neurophysiology*, 30: 5-19.
- Davidson, R. J; Jackson, D. C. and Larson, C. L (2000). "Human Electroencephalography". In: Cacioppo, J. T; Tassinary, L. G and Berntson, G. G., eds. 2000. *Handbook of Psychophysiology*. Cambridge University Press, 2<sup>nd</sup> ed, 27-52
- Datta, D. D and Du, W (2012). Nonparametric HAC Estimation for Time Series Data with Missing Observations. Board of Governors of the Federal Reserve System, International Finance Discussion Papers, Number 1060. Available in: [www.federalreserve.gov/pubs/ifdp/](http://www.federalreserve.gov/pubs/ifdp/). Accessed on: January 03, 2013.
- Decoder: BCI and Detection of Consciousness. Available in: <http://www.decoderproject.eu>. Accessed on: July 15, 2013.
- Delamonica, E.A (1984). Electroencefalografía. Editorial El Ateneo. Buenos Aires.
- Duane, J. F (2006). Duane's Ophthalmology on CD-ROM 2006 edition. Lippincott Williams & Wilkins Publisher. Available in: <http://www.oculist.net/downat0502/prof/ebook/duanes/index.html>. Accessed on: September 04, 2013.
- Duda, R. O; Hart, P. E. and Stork, D. G (2000). Pattern Classification, 2nd ed. United States: John Wiley & Sons Inc., chapter 10: Unsupervised Learning and Clustering, chapter 4: Nonparametric Techniques and chapter 2: Bayesian Decision Theory.

- Estébanez J. M (2003). "EEG-Based Analysis for the Design of Adaptive Brain Interfaces". Ph.D.Thesis. Centre de Recerca en Enginyeria Biomèdica, Espanha.
- Ferreira, A; Bastos, T. F; Sarcinelli, M; Sanchez, J. L. M; Garcia, J. C. G. and Mazo, M. Q (2009). "Improvements of a Brain-Computer Interface Applied to a Robotic Wheelchair". *Communications in Computer and Information Science*, Vol CCIS52, 64-73.
- Ferrez, P. W. and Millán, J. R (2005). "You Are Wrong! - Automatic Detection of Interaction Errors from Brain Waves". *Proceedings of the 19th International Joint Conference on Artificial Intelligence*.
- Ford, M. R; Sands, S. and Lew, H. L (2004). "Overview of artifact reduction and removal in evoked potential and event-related potential recordings". *Physical Medicine and Rehabilitation Clinics of North America*, 15: 1-17.
- Friedman, J. H (1989). "Regularized discriminant analysis". *Journal of the American Statistical Association*, 84(405): 165–175.
- Fukunaga, K (1990). *Statistical Pattern Recognition*. Segunda edição. Academic Press, San Diego, California, USA.
- Gantner, I. S; Bodart, O; Laureys, S. and Demertzi, A (2013). Our rapidly changing understanding of acute and chronic disorders of consciousness: challenges for neurologists, *Future Neurology*, 8(1):43-54.
- Garcia, A. L (1994). *Probability and Random Process for Electrical Engineering*. Addison-Wesley Publishing Coompany. 2<sup>nd</sup> ed.
- Garcés, M. A. and Leber, E. L (2011). "Noise Removal from EEG Signals in Polisomnographic Records Applying Adaptive Filters in Cascade". In: Garcia, L ed. 2011. *Adaptive Filtering Applications*. InTech Publisher, 173-196.
- Gegenfurtner, K. R. and Kiper, D. C (2004). "The processing of color in extrastriate cortex". In: Chalupa, L. M and Werner, J. S., eds. 2004. *The Visual Neurosciences*. Cambridge: The MIT Press, 1017-1028.
- Geisinger, D (2005). "Electrodos Implantableis En El Cerebro en Aplicaciones de Prótesis Neuralis". Artigo vinculado ao XIV Seminário de Engenharia Biomédica, Universidad de La República Oriental Del Uruguay.
- Gonzalez, S. L; Grave de Peralta, R; Thut, G; Millán, J. R; Morier, P. and Landis, T (2006). "Very high frequency oscillations (VHFO) as a predictor of movement intentions". *NeuroImage*, 32(1): 170-179.
- Graimann, B, Huggins, J. E., Levine, S. P. and Pfurtscheller, G (2002). "Visualization of Significant ERD/ERS Patterns in Multichannel EEG and ECoG data". *Clinical Neurophysiology*, 113: 43-47.

- Grave de Peralta, M; Andino, S. G; Perez, L; Ferrez, P. W. and Millán, J (2005). “Non-invasive Estimation of Local Field Potentials for Neuroprosthesis Control.” *Cognitive Processing*, 6: 59-64.
- Grosse, P (2004). “Diagnostic and experimental applications of cortico-muscular and intermuscular frequency analysis”. Thesis for Specialization in Neurology, Clínica de Neurologia, Universidade de Medicina Charité, Campus Virchow-Klinikum, Berlim.
- Guyton, A. C. and Hall, J. E (2006). Textbook of Medical Physiology. 11<sup>a</sup> Edition. Elsevier Saunders Publisher, Philadelphia, Pennsylvania, USA.
- Hashemi, K (2012). The Source of EEG. Available in: <http://www.opensourceinstruments.com/Electronics/A3019/EEG.html>. Accessed on: July 15, 2013.
- He B; Gao S; Yuan H. and Wolpaw J. R. Brain-Computer Interfaces (2013). In: He B; editor. Neural Engineering. Springer, 2<sup>nd</sup> ed., 87-151.
- Hyvärinen, A (1999). Fast and Robust Fixed-Point Algorithms for Independent Component Analysis, *IEEE Transactions on Neural Networks*, 10(3): 626-634.
- Jung, T. P; Makeig, S; Westerfield, M; Townsend, J; Courchesne, E. and Sejnowski, T. J (2000). Removal of eye activity artifacts from visual event-related potentials in normal and clinical subjects, *Clinical Neurophysiology*, 111: 1745-1758.
- Jung, T. P; Makeig, S; Westerfield, M; Townsend, J; Courchesne, E. and Sejnowski, T. J (2001). Analysis and Visualization of Single-Trial Event-Related Potentials, *Human Brain Mapping*, 14: 166-185.
- Kalcher, J. and Pfurtscheller, G (1995). “Discrimination between phase-locked and non-phase-locked event-related EEG activity”. *Clinical Neurophysiology*, (94): 381-384.
- Klonowski, W; Duch, W. and Perovic, A (2009). Some Computational Aspects of the Brain Computer Interfaces Based on Inner Music, *Computational Intelligence & Neuroscience, Special section*, 1-9.
- Kwiatkowski, D; Phillips, P. C. B; Schmidt, P. and Shin, Y (1992). “Testing the null hypothesis of stationarity against the alternative of a unit root”. *Journal of Econometrics*, 54: 159-178.
- Laureys, S; Owen, A. M. and Schiff, N. D (2004). Brain function in coma, vegetative state, and related disorders. *The Lancet Neurology*, 3: 537–546.
- Laureys, S; Pellas, F; Van Eeckhout, P; Ghorbel, S; Schnakers, C; Perrin, F; Berré, J; Faymonville, M. E; Pantke, K. H; Damas, F; Lamy, M; Moonen, G. and Goldman, S (2005). The locked-in syndrome: what is it like to be conscious but paralyzed and voiceless?, *Progress in Brain Research*, 150: 495-511.

- Laureys, S (2005). Science and Society: Death, Unconsciousness and the Brain, *Nature Reviews Neuroscience*, 6(11): 899-909.
- Laureys, S (2007). Eyes open brain shut, *Scientific American*, 4: 32-37.
- Lebedev, M. A. and Nicolelis, M. A. L (2006). Brain-machine interfaces: past, present and future. *TRENDS in Neurosciences*, 29(9): 536:546.
- Leeb, R; Sagha, H; Chavarriaga, R. and Millán, J (2010). Multimodal Fusion of Muscle and Brain Signals for a Hybrid-BCI. *Proceedings of the 32rd Annual International Conference of the IEEE Engineering in Medicine & Biology Society*, 4343-4346.
- Libet, B. (1985). Unconscious cerebral initiative and the role of conscious will in voluntary action. *Behavioral and Brain Sciences*, 8: 529-566.
- Lopes, C. D (2005). “Análise de Sinais de EEG Utilizando a Transformada Wavelet Discreta e as Redes Neurais Artificiais”. Masters Dissertation, Universidade Federal do Rio Grande do Sul.
- Luck, S. J (2005). An Introduction to the Event-Related Potential Technique. Cambridge, MA, London: The Mit Press.
- Machado, A. B. M (2007). Neuroanatomia Funcional. Segunda edição. Editora Atheneu, Belo Horizonte, Minas Gerais, Brazil.
- Malmivuo, J. and Plonsey, R (1995). Bioelectromagnetism - Principles and Applications of Bioelectric and Biomagnetic Fields. Oxford University Press, New York.
- Marmor, M. F; Brigell, M. G; McCulloch, D. L; Westall, C. A and Bach, M (2011). “ISCEV standard for clinical electro-oculography (2010 update)”. *Documenta Ophthalmologica Proceedings Series*, 122:1-7.
- Mcfarland, D. J; McCane, L. M; David, S. V. and Wolpaw, J. R (1997). “Spatial Filter Selection for EEG-based communication”. *Electroencephalography and Clinical Neurophysiology*, 103(3): 386-394.
- Millán, J.del R (2004). On the Need for On-line Learning in Brain-Computer Interfaces. Proceedings of the International Joint Conference on Neural Networks, Hungary, 2877-2882.
- Millán, J; Renkens, F; Mouriño, J. and Gerstner, W (2004). “Noninvasive Brain-Actuated Control of a Mobile Robot by Human EEG”. *IEEE Transactions on Biomedical Engineering*, 51(6): 1026-1033.
- Monti, M. M; Laureys, S. and Owen, A. M (2010). The vegetative state. *BMJ*, 341:292-296.



- Müller, S. M; Celeste, W. C; Bastos, T. F. and Sarcinelli, M (2010). “Brain-Computer Interface Based on Visual Evoked Potentials to Command Autonomous Robotic Wheelchair”. *Journal of Medical and Biological Engineering*, 30: 407-416.
- Obermaier, B; Neuper, C. and Guger C (2001). “Information Transfer Rate in a Five-Class Brain-Computer Interface”. *IEEE Transactions on Neural Systems and Rehabilitation Engineering*, 9(3): 283-288.
- Owen, A. M; Coleman, M. R; Boly, M; Davis, M. H; Laureys, S. and Pickard, J. D (2006). Detecting Awareness in the Vegetative State, *Science*, 313:1402.
- Pfurtscheller, G. and Lopes da Silva, F. H (1999). “Event-Related EEG/MEG Synchronization and Desynchronization: Basic Principles”. Elsevier, *Clinical Neurophysiology*, 110: 1842-1857.
- Pfurtscheller, G; Solis-Escalante, T; Ortner, R; Linortner, P. and Müller-Putz, G. R (2010). “Self-Paced Operation of an SSVEP-Based Orthosis With and Without an Imagery-Based “Brain Switch:” A Feasibility Study Towards a Hybrid BCI”. *IEEE transactions on neural systems and rehabilitation engineering*, 18(4): 409-414.
- Roland, P. E; Larsen, B; Lassen, N. A. and Skinhøj, E (1980). “Supplementary motor area and other cortical areas in organization of voluntary movements in man”. *Journal of Neurophysiology*, 43(1): 118-136.
- Rugg, M. D. and Coles, M. G. H (1996). “Electrophysiology of Mind Event-Related Brain Potentials and Cognition”. *Oxford Psychology Series*.
- Russell, R (2013). Human Brain: Sections, Directions and Divisions. Available in: [http://homepage.smc.edu/russell\\_richard/Psych2/Graphics/human\\_brain\\_directions.htm](http://homepage.smc.edu/russell_richard/Psych2/Graphics/human_brain_directions.htm). Accessed on: July 15, 2013.
- Rush, S. and Driscoll, D. A (1969). “EEG - electrode sensitivity – An application of reciprocity”. *IEEE Transactions on Biomedical Engineering*, 16(1): 15-22.
- Sammon, J. W (1969). “A Nonlinear Mapping for Data Structure Analysis”. *IEEE Transactions on Computers*, 18(5): 401-409.
- Schaefer, R. S; Vlek, R. J. and Desain, P (2011a). Music perception and imagery in EEG: Alpha band effects of task and stimulus, *International Journal of Psychophysiology*, 82: 254-259.
- Schaefer, R. S; Vlek, R. J. and Desain, P (2011b). Decomposing rhythm processing: electroencephalography of perceived and self-imposed rhythmic patterns, *Psychological Research*, 75: 95-106.
- Schaefer, R. S; Farquhar, J; Blokland, Y; Sadakata, M. and Desain, P (2011c). Name that tune: Decoding music from the listening brain, *NeuroImage*, 56: 843-849.

- Shahid, S; Prasad, G. and Sinha, R. K (2011). On fusion of heart and brain signals for hybrid BCI. *Proceedings of the 5th International IEEE EMBS Conference on Neural Engineering*, 48-52.
- Soon, C. S; Brass, M; Heinze, H. J. and Haynes, J. D (2008). Unconscious determinants of free decisions in the human brain, *Nature Neuroscience*, 11(5): 543:545.
- Soriano, D; Silva, E. L; Slenes, G. F; Lima, F. O; Uribe, L. F. S; Coelho, G. P; Rohmer E; Venâncio, T. D; Beltramini, G. C; Campos, B. M; Anjos, C. A. S; Suyama R; Li, M. L; Castellano, G. and Attux, R (2013). "Music versus Motor Imagery for BCI Systems". *Proceedings of the 4th IEEE Biosignals and Biorobotics conference*, 1-6.
- Sun, M (1997). "An Efficient Algorithm for Computing Multishell Spherical Volume Conductor Models in EEG Dipole Source Localization". *IEEE Transactions on Biomedical Engineering*, 44(12): 1243-1252.
- Schwert, G. W (1989). "Tests for Unit Roots: A Monte Carlo Investigation". *Journal of Business and Economic Statistics*, 7(2): 147-159.
- Tang, C; Fusheng, Y; Guang, C; Dakuan, G; Feng, F; Guosheng, Y and Xiuzhen, D (2008). "Correlation Between Structure and Resistivity Variations of the Live Human Skull". *IEEE Transactions on Biomedical Engineering*, 55(9): 2286-2292.
- Thalamocortical Oscillations. Scholarpedia. Available in: [http://www.scholarpedia.org/article/Thalamocortical\\_oscillations](http://www.scholarpedia.org/article/Thalamocortical_oscillations). Accessed on: July 16, 2013.
- Vigário, R; Särelä J; Jousmäki, V; Hämmäläinen, M. and Oja, E (2000). Independent Component Approach to the Analysis of EEG and MEG Recordings, *IEEE Transactions on Biomedical Engineering*, 47(5): 589-593.
- What-when-how. The Thalamus and Cerebral Cortex (Integrative Systems) Part 2. Available in: <http://what-when-how.com/neuroscience/the-thalamus-and-cerebral-cortex-integrative-systems-part-2/>. Accessed on: July 15, 2013.
- Wolpaw, J. R (2007). "Brain-computer interfaces as new pathways". *The Journal of Physiology*, 579(3): 613-619.
- Wolpaw, J. R; Birmaumer, N; McFarland, D. J; Pfurtscheller, G. and Vaughan, T.M (2002). "Brain-computer interfaces for communication and control". *Clinical Neurophysiology*, 113(6): 767-791.
- Zatorre, R. J. and Halpern, A. R (2005). Mental Concerts: Musical Imagery and Auditory Cortex, *Neuron*, 47: 9-12.
- Zeki, S. and Marini, L (1998). "Three cortical stages of color processing in the human brain". *Brain*, 121: 1669-1685.

## Appendix A

### An Ethernet sniffer for BrainNet36<sup>®</sup>

This Ethernet sniffer was designed to work together with the medical device for EEG acquisition BrainNet36<sup>®</sup> (BNT36), from EMSA Equipamentos Médicos Ltda (Figure 5.1 - A). BrainNet36<sup>®</sup> has 36 channels (Figure 5.1 - C), A/D converters with 16 bit accuracy, conversion time of 10  $\mu$ s and Ethernet communication interface. The smaller amplitude of the patient physiological signal that this equipment can handle and display reliably is 2  $\mu$ V. Being a device for clinical purposes, BrainNet36<sup>®</sup> does not export data online.

The sniffer is a program able to track the data packets sent into a network. BNT sends UDP packets with coded EEG information, then, the sniffer is configured in promiscuous mode to observe and decode the data, writing them into a text file, without blocking the original data flow. The sniffer was released as free and open source software in accordance with the General Public License version 3.0 (GPLv3) and published in the web-based source code repository SourceForge (Benevides, A. B. [Alessander] and Benevides, A. B. [Alessandro], 2013):

- <http://sourceforge.net/projects/brainnet36-ethernet-sniffer/> (Accessed on: October 30, 2013).

The data is sent by UDP packets with payload of 1470 Bytes (Figure A.1). The samples are 16-bit signed integers and each packet contains 20 samples (2 Bytes) for each channel, in a total of 1440 Bytes. Data is placed moment by moment and the order of the channels in the packets is: channel 1, channel 2, ..., channel 36 = F7, T3, T5, Fp1, F3, C3, P3, O1, F8, T4, T6, Fp2, F4, C4, P4, O2, Fz, Cz, Pz, Oz, 21, 22, ..., 36.

Using more channels or fewer channels does not alter the packet size, so that unused channels are also sent in the packet. The sampling frequency of the device can be varied between 100 to 600 Hz, but it does not change the packet size. Changing the sampling frequency of the device only increases or slows the emission rate of packets. The header of BNT36 packets includes information about the packet itself (one of them is a 32-bit integer with the packet number). The first sample of the first channel starts at position 71 (72 Byte). The destination port is fixed to 11111. Figure A.1 shows the schematic of the UDP packet sent by BNT36.

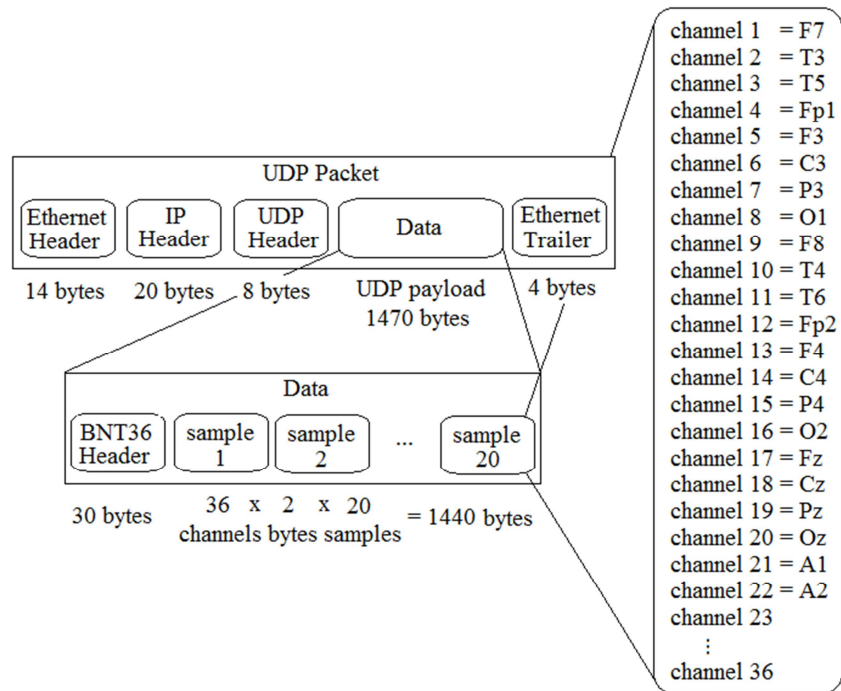


Figure A.1 – UDP packet sent by BNT36.

### User guide on Windows:

1. Install WinPcap for Windows [1] and extract it under C:. The zip file contains a directory named WpdPack, so, after unpacking, you should have C:\WpdPack.
2. Open the terminal, enter the directory where you put BrainNet36Sniffer.c and enter the following command-line: `BrainNet36Sniffer.exe \\Device\Tcpip_{xxxxxxxx-xxxx-xxxx-xxxx-xxxxxxxxxxxx} k1 k2 data`. Where `Tcpip_{x-x-x-x}` is the MAC address of your ethernet board. One can get this MAC address using the function 'getmac' in the terminal (making sure that the Ethernet cable is connected). "k1" is the number of packets to be monitored and "k2" is the number of packets to be recorded in the same text file. Here 'data' is the name of the text file generated with the EEG data. You can replace it. If "k1" is equal to "k2", the sniffer writes one text file named "data0001.txt" with "k2" packets. If "k1" is larger than "k2", the sniffer writes several text files with "k2" packets named: data0001.txt, data0002.txt, etc.
3. Each text file records continuously the concatenated EEG data in the same order that they appear in the UDP packet.

[1] <http://www.winpcap.org/install/default.htm>

For example, if you use the following command-line: `BrainNet36Sniffer.exe \\Device\\Tcpip_{put here your ethernet device MAC address} 200 50 data`. You will sniff 200 packets and write it on 4 text files, each one with 50 packets: `data0001.txt`, `data0002.txt`, `data0003.txt` and `data0004.txt`. As each packet contains 20 samples of each channel (concatenated as shown in figure A.1), the file “`data0001.txt`” will present 50 packets, i. e., 1000 samples concatenated in the same order that they appear in the UDP packet.

### **How to compile on Windows:**

1. Install MinGW [1] in order to get gcc.
2. Install WinPcap for Windows [2].
3. Download WinPcap Developer's Pack [3] and extract it under C:. The zip file contains a directory named `WpdPack`, so, after unpacking, you should have `C:\WpdPack`.
4. Open the terminal, enter the directory where you put `BrainNet36Sniffer.c` and enter the following command-line: `gcc -Wall -I C:\WpdPack\Include -o BrainNet36Sniffer.exe BrainNet36Sniffer.c -L C:\WpdPack\Lib -lwpcap`.

[1] [http://www.mingw.org/wiki/Getting\\_Started](http://www.mingw.org/wiki/Getting_Started)

[2] <http://www.winpcap.org/install/default.htm>

[3] <http://www.winpcap.org/devel.htm>